

# **Chaos Theory and its Application in the Atmosphere**

by  
Xubin Zeng

Department of Atmospheric Science  
Colorado State University  
Fort Collins, Colorado

Roger A. Pielke, P.I.  
NSF Grant #ATM-8915265

**Colorado**  
**State**  
University

**Department of**  
**Atmospheric Science**

Paper No. 504

CHAOS THEORY AND ITS APPLICATION IN THE ATMOSPHERE

Xubin Zeng

Department of Atmospheric Science  
Colorado State University  
Fort Collins, Colorado  
Summer, 1992

Atmospheric Science Paper No. 504



U18400 7029194

## ABSTRACT

### CHAOS THEORY AND ITS APPLICATION IN THE ATMOSPHERE

Chaos theory is thoroughly reviewed, which includes the bifurcation and routes to turbulence, and the characterization of chaos such as dimension, Lyapunov exponent, and Kolmogorov-Sinai entropy. A new method is developed to compute Lyapunov exponents from limited experimental data. Our method is tested on a variety of known model systems, and it is found that our algorithm can be used to obtain a reasonable Lyapunov-exponent spectrum from only 5000 data points with a precision of  $10^{-1}$  or  $10^{-2}$  in 3- or 4-dimensional phase space, or 10,000 data points in 5-dimensional phase space. On the basis of both the objective analyses of different methods for computing the Lyapunov exponents and our own experience, which is subjective, this is recommended as a good practical method for estimating the Lyapunov-exponent spectrum from short time series of low precision.

The application of chaos is divided into three categories: observational data analysis, new ideas or physical insights inspired by chaos, and numerical model output analysis. Corresponding with these categories, three subjects are studied. First, the fractal dimension, Lyapunov-exponent spectrum, Kolmogorov entropy, and predictability are evaluated from the observed time series of daily surface temperature and pressure over several regions of the United States and the North Atlantic Ocean with different climatic signal-to-noise ratios. Although our time series are longer than those used in the previous studies, it is found that no saturated value of the correlation dimension can be obtained. However, it can be shown that the correlation dimension is greater than 8. It is also pointed out that most, if not all, of the previous estimates of low fractal dimensions in the atmosphere are

spurious. By means of computing the Lyapunov-exponent spectrum, it is found that the error-doubling time is about 2 to 3 days in Fort Collins, Colorado, about 4 to 5 days in Los Angeles, California, and about 5 to 8 days in the North Atlantic Ocean. The predictability time is longer over regions with a higher climatic signal-to-noise ratio (e.g., Los Angeles), and the predictability time of summer and/or winter data is longer than for the entire year. The difference between our estimates of the error-doubling time and estimates based on General Circulation Models (GCMs) is discussed.

Second, chaos theory is applied to the study of daisyworld, which is defined as a cloudless flat or cylindrical planet with negligible atmospheric greenhouse gases in which bare soil and daisies of different colors interact so as to maintain stable climatic conditions. It is found that periodic, and even chaotic, states can exist when the parameter controlling the feedback between biota and environmental temperature is changed. The existence of periodic and chaotic solutions is verified by their power spectra, fractal dimensions, and Lyapunov exponents. These results show that stable climatic conditions are not always maintained in daisyworld, despite the presence of daisies which supply the required feedback. While daisyworld is a simple model, the mathematical analysis of this model raises important questions regarding the validity and interpretation of the Gaia hypothesis.

Finally, using the CSU Regional Atmospheric Modeling System (RAMS) in its nonhydrostatic and compressible configuration, over 200 two-dimensional simulations with  $\Delta x = 2$  km and  $\Delta z = 100$  m are performed to study in detail the initial adjustment process and the error-growth dynamics of surface thermally-induced circulations including the sensitivity to initial conditions (i.e., the traditional predictability), boundary conditions, and model parameters, and to study the predictability as a function of the size of surface heat patches under calm mean wind. It is found that the error growth (at least at the stage when the surface forcing is strong) is not sensitive to the characteristics of the initial perturbations. The numerical smoothing has a strong impact on the initial adjustment process and on the error-growth dynamics. The predictability is variable-dependent. The mesoscale flow is insensitive to lateral and top boundary conditions. Among the conclusions regarding the influence of the boundary layer structures and model parameters on

the predictability and flow structures, it is found that the vertical velocity field is strongly affected by the mean wind, and the flow structures are quite sensitive to the initial soil water content. The transition from organized flow to the situation in which fluxes are dominated by non-coherent turbulent eddies under calm mean wind is quantitatively evaluated and this transition is different for different variables. The relationship between the predictability of a realization and of an ensemble average is discussed. The predictability and the coherent circulations modulated by the surface inhomogeneities are also studied by computing the autocorrelations and the power spectra. The three-dimensional mesoscale and large-eddy simulations are performed to verify the above results. It is found that the two-dimensional mesoscale (or fine-resolution) simulation yields close or similar results regarding the predictability as those from the three-dimensional mesoscale (or large-eddy) simulation. The horizontally averaged quantities based on two-dimensional fine-resolution simulations agree with those based on three-dimensional large-eddy simulations. By computing the fractal dimensions from the numerical model output, it is found that low (less than 5) -dimensional attractors are present for the surface thermally-induced circulations. Possible physical processes related to these low dimensions are also discussed.

Xubin Zeng  
Department of Atmospheric Science  
Colorado State University  
Fort Collins, Colorado 80523  
Summer 1992

To my grandmother and my parents

## ACKNOWLEDGEMENTS

I would first like to express my gratitude to my Committee members, Professors Roger A. Pielke, Richard E. Eykholt, David A. Randall, Wayne H. Schubert, and Ronald M. Errico for their help and many suggestions over the years of my research here. My advisor, Professor Roger Pielke, facilitated my entry into the exciting field of chaos. His suggestions and physical insights concerning the direction of my research proved invaluable, and his supervising philosophy of providing students with the maximum opportunity to perform independent, innovative investigations proved helpful for my research (for example, I was, therefore, able to develop a practical method for computing Lyapunov exponents), and I believe that it will also prove helpful for my future career. Professor Richard Eykholt helped me to understand chaos. Many philosophical discussions with him about comparing the development of chaos theory with other theories, such as quantum mechanics, helped me to stand higher in my research. His very thorough revision of our published papers, which are parts of my dissertation, significantly strengthened our papers and helped me to improve my English. Many discussions with Professor David Randall in broad areas and suggestions from him not only helped my research, but also inspired a few new ideas about future research on various subjects. Some lengthy discussions with Professor Wayne Schubert and suggestions from him improved my understanding of mesoscale dynamics and related problems. Discussions with Dr. Ronald Errico and suggestions from him were especially helpful in explaining the numerical results on mesoscale predictability.

I would also like to give special thanks to Professor Qingcun Zeng, director of Institute of Atmospheric Physics, Chinese Academy of Sciences, for his suggestions about my research and for many fruitful discussions when I was in China and when he visited our department.

I am also indebted to many students and staff in our department, especially Dr. Bob Walko, John Lee, Dr. Craig Trembach, Joe Eastman, Mike Moran, and Dallas McDonald for their help. Dr. Bob Walko gave me some help when I set up the initial 2-D fine-resolution simulations, and he is also thanked for some helpful discussions regarding the influence of surface inhomogeneity on coherent structures in the convective boundary layer. John Lee helped me to use different computer softwares, and he is also thanked for some general discussions. Dr. Craig Trembach answered some model-related questions. Joe Eastman gave me some help when I set up the initial 2-D mesoscale simulations. Mike Moran is thanked for some discussions regarding boundary layer dynamics and pollutant dispersion. Dallas McDonald is thanked for some editorial assistance in the preparation of this work.

I cannot overstate my gratitude to my wife, Qingqiu, for her unwavering support and many helpful discussions. In fact, I first knew of chaos from her, because she worked on chaos a few years ago. This work could not have been completed in time without the help of my parents, who took care of my baby, David, in the final six months of this work.

Numerical computations were performed on the IBM RISC 6000 workstations in the Department of Atmospheric Science, on the CRAY-XMP and CRAY-YMP computers at the National Center for Atmospheric Research (NCAR), which is supported by the National Science Foundation, and on the CYBER 205 computer at Colorado State University. The observational data were accessed from the Colorado Climate Center with the help of T. Mckee and J. Kleist, and from the Mass Storage archive at NCAR with the help of D. Joseph and R. Jenne. This research was funded by the National Science Foundation under grants ATM-8616662 and ATM-8915265. The living allowance for the first year was provided by the Chinese Academy of Sciences.

## TABLE OF CONTENTS

<b>1 Introduction</b>	<b>1</b>
1.1 Bifurcation and Routes to Turbulence . . . . .	3
1.2 Characterization of Chaos . . . . .	5
1.2.1 Dimensions of attractors . . . . .	5
1.2.2 Lyapunov exponents of attractors . . . . .	6
1.3 Application of Chaos Theory . . . . .	8
<b>2 Computation of dimensions and Lyapunov exponents</b>	<b>11</b>
2.1 Phase-Space Reconstruction . . . . .	11
2.2 Computation of Fractal Dimensions . . . . .	15
2.3 Computation of Lyapunov Exponents . . . . .	19
<b>3 Fractal dimension and predictability of the atmosphere</b>	<b>32</b>
3.1 The Data . . . . .	32
3.2 Fractal Dimensions of Weather Attractors . . . . .	33
3.3 Lyapunov Exponents and Predictability of the Atmosphere . . . . .	44
<b>4 Chaos in Daisyworld</b>	<b>50</b>
4.1 Introduction . . . . .	50
4.2 Differential Model for Daisyworld . . . . .	51
4.2.1 Differential model . . . . .	51
4.2.2 Steady-state behavior of the system . . . . .	53
4.3 Discrete Model for Daisyworld . . . . .	57
4.3.1 Discrete model . . . . .	57
4.3.2 Theoretical analysis of the chaotic regime in the daisyworld model . . . . .	59
4.4 Numerical Results on Chaos in Daisyworld . . . . .	60
4.4.1 Daisyworld with only black daisies. . . . .	61
4.4.2 Daisyworld with only white daisies. . . . .	63
4.4.3 Daisyworld with both black and white daisies. . . . .	66
4.4.4 Verification of chaos in daisyworld . . . . .	69
4.5 Conclusions . . . . .	69
<b>5 Error-growth dynamics and predictability of surface thermally-induced circulations</b>	<b>72</b>
5.1 Introduction . . . . .	72
5.1.1 Definition of predictability . . . . .	72
5.1.2 Large-scale atmospheric predictability . . . . .	76
5.1.3 mesoscale atmospheric predictability . . . . .	80
5.2 Numerical Models . . . . .	84

5.2.1	Governing equations . . . . .	84
5.2.2	Numerical schemes . . . . .	85
5.2.3	Parameterizations . . . . .	85
5.2.4	Boundary conditions . . . . .	86
5.2.5	Grid structure . . . . .	87
5.2.6	Initial conditions . . . . .	88
5.2.7	Miscellaneous aspects . . . . .	88
5.3	Error-Growth Dynamics . . . . .	90
5.3.1	Influence of initial uncertainties . . . . .	90
5.3.2	Impact of numerical smoothing . . . . .	96
5.3.3	Effect of boundary layer structure and surface heating . . . . .	100
5.3.4	Sensitivity to boundary conditions and model parameters . . . . .	102
5.4	Predictability as a Function of the Size of Surface Heat Patches . . . . .	107
5.5	Three-Dimensional Experiment . . . . .	117
5.6	Further Analysis of Model Output . . . . .	120
5.6.1	Analysis tools . . . . .	121
5.6.2	Results of further analysis . . . . .	123
5.7	Conclusions . . . . .	143
<b>6</b>	<b>Conclusions and suggestions for future work</b>	<b>149</b>
6.1	Conclusions . . . . .	149
6.2	Suggestions for Future Work . . . . .	153
<b>7</b>	<b>References</b>	<b>156</b>
<b>A</b>	<b>Explanation for some features in Figures 4.3-4.4, and 4.6-4.8</b>	<b>178</b>

## LIST OF FIGURES

2.1	Mean-error growth for the logistic map $z_{n+1} = 3.8z_n(1 - z_n)$ . . . . .	25
2.2	(a) Autocorrelation function and (b) convergence of Lyapunov exponents. . . . .	29
3.1	(a) Time evolution of the surface temperature at Fort Collins, Colorado; (b) time trajectory of the above time series evolving in a two-dimensional phase space; (c) autocorrelation function. . . . .	35
3.2	Power spectrum $E_T$ of the daily surface temperature at Fort Collins, Colorado. . . . .	36
3.3	Plots of $\ln C(r)$ versus $\ln r$ for embedding dimensions $k = 5, 7, \dots, 19$ (ordered from left to right) for the sea surface pressure at BOX 139. (a) daily data; (b) winter data; (c) summer data. . . . .	38
3.4	Plots of the dimensionality $\nu$ as a function of embedding dimension $k$ for the same circumstances as in Fig. 3.3. . . . .	39
4.1	Steady-state behavior of daisyworld. (a) Areas of four species. (b) effective temperatures for the cases of one to four species. . . . .	54
4.2	Steady-state responses of daisyworld with Eq. (4.8). (a) Areas of black and white daisies; (b) effective temperature $T_e$ . . . . .	56
4.3	Chaotic behavior of the effective temperature $T_e$ in daisyworld with only black daisies at $L = 0.90$ and $C = 4.0$ . (a) $\gamma_b = 1.0$ ; (b) $\gamma_b = 0.9$ ; (c) $\gamma_b = 0.8$ ; (d) $\gamma_b = 0.3$ . . . . .	61
4.4	The same as in Fig. 4.3, except for the area $a_b$ occupied by black daisies. . . . .	62
4.5	Values of $a_b$ and $T_e$ in the model with only black daisies at $L = 0.90$ and $C = 3.0$ , and $\gamma_b = 0.3$ . (a) $a_b$ ; (b) $T_e$ . . . . .	64
4.6	Chaotic behavior of $a_w$ and $T_e$ in daisyworld with only white daisies at $L = 0.92$ and $C = 4.0$ . (a) $a_w$ with $\gamma_w = 1.0$ ; (b) $T_e$ with $\gamma_w = 1.0$ ; (c) $a_w$ with $\gamma_w = 0.8$ ; (d) $T_e$ with $\gamma_w = 0.8$ . . . . .	65
4.7	Chaotic behavior of $a_w$ , $a_b$ , and $T_e$ in daisyworld with black and white daisies at $L = 0.80$ , $C = 4.0$ , and $\gamma_w = \gamma_b = 1.0$ . (a) $a_w$ ; (b) $a_b$ ; (c) $T_e$ . . . . .	67
4.8	Periodic behavior of daisyworld with two species at $L = 0.80$ , $C = 3.0$ , and $\gamma_b = \gamma_w = 0.8$ . (a) $a_w$ ; (b) $a_b$ ; (c) $T_e$ . . . . .	68
4.9	Power spectra $E_T$ of the effective temperature for the cases of one and two species in daisyworld. (a) periodic state; (b) slightly chaotic state; (c) chaotic state. . . . .	70
5.1	Mean error growth for the logistic map $z_{n+1} = 3.8z_n(1 - z_n)$ . . . . .	75
5.2	The first-hour adjustment process of the initial random perturbations $\theta'_0$ with mean value of 0.1 K and RMS difference of 0.114 K in the subdomain C. . . . .	93
5.3	RMSP for $\theta$ , $u$ , and $w$ in the subdomain C. . . . .	95
5.4	The same as in Fig. 5.2. except for an integration of 12 hours. . . . .	97
5.5	RMSP for $\theta$ , $u$ , and $w$ in the subdomain C with $K_H$ and FILT4. . . . .	98

5.6	The signal (RMSC) and noise (RMSP) of $\theta$ , $u$ , and $w$ in the subdomain C for the standard run ST. . . . .	101
5.7	The signal (RMSC) and noise (RMSP) of $w$ in the subdomain C for the same case as ST except with the synoptic wind $U = 3, 6, \text{ or } 9 \text{ m/s}$ . . . . .	103
5.8	The RMSD of $\theta$ , $u$ and $w$ in the subdomain C between the standard run ST (with $SLM = 0.6$ ) and the simulations of $SLM = 0.54, 0.57, 0.63, \text{ or } 0.66$ . . . . .	106
5.9	RMSC( $w$ ), denoted by the solid line, and RMSP( $w$ ), denoted by the dotted line, for $L = 0$ to 40 km. . . . .	109
5.10	RMSC( $w$ ), denoted by the solid line, and RMSP( $w$ ), denoted by the dotted line, for $L = 50$ to 150 km, based on $\Delta x = 2 \text{ km}$ . . . . .	110
5.11	Same as Fig. 5.9 but for $u$ . . . . .	113
5.12	Same as Fig. 5.10 but for $u$ . . . . .	114
5.13	Same as Fig. 5.9 but for $\theta$ . . . . .	115
5.14	Same as Fig. 5.10 but for $\theta$ . . . . .	116
5.15	RMSC and RMSP of $\theta$ , $u$ and $w$ in the 3-D mesoscale simulations with $L = 50 \text{ km}$ . . . . .	119
5.16	Same as Fig. 5.15 but for the 3-dimensional large-eddy simulation with $L = 0 \text{ km}$ . . . . .	120
5.17	The horizontally averaged quantities for the horizontally homogeneous case ( $L = 0 \text{ km}$ ) from 3-D large-eddy simulation. . . . .	124
5.18	Same as Fig. 5.17 except from 2-D fine-resolution simulation. . . . .	125
5.19	The horizontally averaged quantities at time $t = 9 \text{ hours}$ for the case of $L = 1 \text{ km}$ . . . . .	127
5.20	The same as Fig. 5.19, except for the case of $L = 5 \text{ km}$ . . . . .	128
5.21	The autocorrelation coefficients of $\theta$ , $u$ , and $w$ at time $t = 9 \text{ hours}$ and at the fourth vertical level. . . . .	129
5.22	Same as Fig. 5.21 except for the error fields between the control and perturbed simulations. . . . .	131
5.23	The power spectra of $\theta$ and $u$ at the height $z = 108 \text{ m}$ , and $w$ at the height $z = 132 \text{ m}$ for the cases of $L = 0$ and $1 \text{ km}$ . The panels of (a), (c), and (e) represent the homogeneous case; the panels of (b), (d), and (f) represent the case of $L = 1 \text{ km}$ . . . . .	132
5.24	The power spectra of $u$ , denoted by the solid line, and of the error field of $u$ , denoted by the dotted line, at the height $z = 108 \text{ m}$ for the cases of $L = 0$ and $5 \text{ km}$ , and at $z = 112 \text{ m}$ for $L = 30 \text{ km}$ at time $t = 9 \text{ hours}$ . . . . .	134
5.25	The power spectra of $w$ , denoted by the solid line, and of the error field of $w$ , denoted by the dotted line, at the height $z = 132 \text{ m}$ for the cases of $L = 0 \text{ km}$ , and at $z = 139 \text{ m}$ for $L = 30$ and $100 \text{ km}$ at time $t = 9 \text{ hours}$ . . . . .	135
5.26	The power spectra (denoted by the solid lines) of $\theta$ and $u$ at the height $z = 108 \text{ m}$ , and $w$ at the height $z = 132 \text{ m}$ for the homogeneous case (i.e., $L = 0 \text{ km}$ ) at time $t = 9 \text{ hours}$ . . . . .	136
5.27	Correlation dimension plot for $\theta$ , $u$ , and $w$ , using the data at all grid points. . . . .	138
5.28	The same as in Figure 5.27 except for the cases of $L = 10, 30, 50, \text{ and } 100 \text{ km}$ . . . . .	140
5.29	Correlation dimension plot for $\theta$ , $u$ , and $w$ , using the data at 66 grid points (11 points at each of six selected levels in the boundary layer). . . . .	141
5.30	Correlation dimension plot for the case of $L = 5 \text{ km}$ . The phase space is reconstructed by using variables at different grids as separate coordinates. . . . .	142

5.31 Correlation dimension plot of  $w$  for the case of  $L = 5$  km. The phase space is reconstructed from the large time series created by catenating the different time series from 11 grids. . . . . 144

## LIST OF TABLES

2.1	Lyapunov-exponent spectrum for various known model systems. . . . .	31
3.1	Dimensionality $\nu$ as a function of embedding dimension $k$ for the analyzed data.	41
3.2	Kolmogorov-Sinai entropy $K$ and error-doubling time $T$ of the sea surface pressure (SSP) at BOX 139 and BOX 244 and of the surface temperature (ST) at Los Angeles (LA). . . . .	46
3.3	Lyapunov-exponent spectrum with the parameters given in the text. . . . .	46
4.1	Correlation dimension $\nu$ and Lyapunov exponents $\lambda$ for some cases of chaos from Subsection 4.4.4 . . . . .	70

## Chapter 1

### INTRODUCTION

Nonlinear phenomena occur in nature in a wide range of apparently different contexts such as hydrodynamic turbulence, chemical kinetics, electronics, ecology, and biology; yet they often display common features, or can be understood using similar concepts, permitting unification of their study. The similarity of complicated behaviors is not a superficial similarity at the descriptive level; instead, it concerns experimental details. This similarity results from the modern theory of nonlinear systems, or, more precisely, the qualitative theory of differential dynamical systems, which deals with order within chaos and chaos out of order. The former includes such features as solitons, coherent structures, and pattern formation, and the latter can be studied by computing fractal dimensions, Lyapunov exponents, and the Kolmogorov-Sinai entropy, and by other methods.

Li and Yorke (1975) seem to be the first to introduce the word *chaos* into the mathematical literature to denote the apparently random output of some mappings, although the use of the word *chaos* in physics dates back to L. Boltzmann in the nineteenth century in another context unrelated to its present usage. However, there is still no generally accepted definition of the word *chaos*. Usually, chaos (deterministic chaos) refers to the irregular, unpredictable behavior in deterministic, dissipative, and nonlinear dynamical systems. It should be emphasized that chaos can not be equated simply with disorder, and it is more appropriate to consider chaos as a kind of order without periodicity. It is demonstrated in Lorenz (1963) that the sensitive dependence on initial conditions of a system is related to the aperiodic behavior of the system. By dynamical system we mean any system, whatever its nature (e.g., physical), which can take various mathematical forms: differential equations or iterative mappings. A vast number of modes die out due

to friction in a dissipative dynamical system, and the asymptotic state of the system can be described in a subspace of a much lower dimension, called the attractor. Chaos can also occur in Hamiltonian or conservative systems, but this subject requires special methods due to the absence of an attractor.

There were some classical physicists and mathematicians, even in the previous century, who had thought about dynamical systems. Hadamard (1898) first observed the sensitivity of the solution to initial conditions at the end of the last century in a rather special system called geodesic flow. Subsequently, Poincaré (1908) discussed sensitivity to initial conditions (SIC) and unpredictability at the level of scientific philosophy. (Poincaré even went on to discuss the problem of weather predictability!) However, their ideas seem to have been forgotten until Lorenz (1963) rediscovered them independently in his elegant paper entitled “Deterministic nonperiodic flow” more than half a century later. Therefore, Lorenz is regarded as the first to discover the irregular behavior and to analyze it quantitatively in completely deterministic dissipative systems. Lorenz used a simple model system of three coupled, first-order, nonlinear, ordinary differential equations, a model which carries his name, to model the nonlinear evolution of the Rayleigh-Bénard instability, i.e., the instability which results when a fluid layer subjected to gravity is heated sufficiently from below. By a combination of careful analysis of the numerical solutions and analytical reasoning, Lorenz was able to deduce that the solution of his equations is eventually trapped in a region of the phase space of the system which has a very intricate (strange) geometric structure, and the solution is sensitive to initial conditions. Eight years later, Ruelle and Takens (1971), making use of then recent developments in mathematics, proposed a possible mechanism for the transition from laminar flow to turbulence. Ruelle and Takens were the first to introduce the concept of a strange attractor, which is topologically different from other attractors, such as point attractors which lead to steady-state solutions, limit cycles which lead to periodic solutions, and tori which lead to quasiperiodic solutions. The name *strange attractor* refers to its unusual properties, the most crucial being SIC; i.e., two initially close trajectories on the attractor eventually diverge from one another. These two independent, pioneering papers triggered an upsurge of research interest among

researchers in different fields in an attempt to gain new insights. Since then, especially since 1975, publications related to chaos have grown extremely rapidly, and it is not the purpose of this study to review all of this progress. Many of the historical papers on chaos were assembled into a single reference volume by Hao (1984). A comprehensive treatment of chaos with a readable account of many aspects of the subject may be found in Bergé *et al.* (1984). Some more recent references can be found in, for example, Campbell (1990) and Marek and Schreiber (1991). However, most of the progress in this field so far may be roughly divided into two different categories: one involves bifurcation and routes to turbulence, and the other consists of quantitative means to recognize, characterize, and classify attractors. Here, we only give a brief review. For theories not related to our work, only the original references and a few review papers will be cited; for theories related to our work, relatively complete references will be cited.

### 1.1 Bifurcation and Routes to Turbulence

Ruelle and Takens (1971) showed that the Landau-Hopf route (Landau, 1944; Hopf, 1948) to turbulence is unlikely to occur in nature, and proposed a route based on four consecutive bifurcations: fixed point  $\rightarrow$  limit cycle  $\rightarrow$  2-torus  $\rightarrow$  3-torus  $\rightarrow$  strange attractor (turbulence). A few years later, in collaboration with Newhouse, they reduced this scheme to: fixed point  $\rightarrow$  limit cycle  $\rightarrow$  2-torus  $\rightarrow$  strange attractor; i.e., quasiperiodic motion on a 2-torus may lose stability and give birth to turbulence directly (Newhouse *et al.*, 1978). This route, called the Ruelle-Takens route to turbulence, is generic and is shown to take place in many models and laboratory experiments, but remains less well understood theoretically than the other two routes mentioned below.

In an excellent review, May (1976) called attention to the very complicated dynamics, including period-doubling and chaos, in some very simple iterative mappings. Subsequently, Feigenbaum (1978 and 1979a) discovered the scaling properties and universal constants in one-dimensional mappings, and introduced renormalization-group theory into this field. In addition, Feigenbaum proposed another route, which is now called the Feigenbaum route to turbulence: a period-doubling-bifurcation cascade with periods  $p =$

$2^n$  which quickly converge to an aperiodic orbit as  $n \rightarrow \infty$ . This scenario is extremely well tested in both numerical and physical systems. The period doublings have been observed in experiments such as Rayleigh-Bénard convection.

The third route, called the Pomeau-Manneville route to turbulence, is through intermittency (Pomeau and Manneville, 1980; Manneville and Pomeau, 1980). The term *intermittency* in the context of chaos refers to random alternations of chaotic and regular behavior in time without involving any spatial degrees of freedom, which is slightly different from the original meaning of intermittency in the hydrodynamic theory of turbulence, where intermittency denotes random bursts of turbulent motion on the background of laminar flow. This scenario and the Feigenbaum scenario are in fact twin phenomena (Hao, 1984), but its mathematical status is somewhat less satisfactory than that of the other two scenarios mentioned above, because its parameter region contains an infinity of (very long) stable periods, and because there is no mention as to when the turbulent regime is reached or what is the exact nature of this turbulence (Eckmann, 1981). Intermittent transitions to turbulence have been seen in many physical experiments.

Although we are facing a situation of “all routes lead to turbulence”, the above three routes are the most thoroughly studied. The Ruelle-Takens route is related to Hopf bifurcation where a pair of complex eigenvalues cross the unit circle; the Feigenbaum route is associated with pitchfork bifurcation where an eigenvalue crosses the unit circle at  $-1$ ; and the Pomeau-Manneville route is associated with saddle-node bifurcation where an eigenvalue crosses the unit circle at  $+1$ . A more detailed discussion of these routes is given in a review paper by Eckmann (1981). Related to bifurcations is the crises of chaotic attractors, i.e., the abrupt changes of the general shapes of attractor at certain parameter values, and this is discussed by Grebogi *et al.* (1982).

The reason for such intensive studies of the routes to turbulence is that it is believed that the key to understanding turbulence may be hidden in the onset mechanism, as pointed out by Landau (1944). Turbulence has been a long-standing problem in physics. It is no longer a specific problem in hydrodynamics; instead, it has become a general concept, relevant to many fields of science such as solid-state turbulence, chemical turbulence, acoustic turbulence, and optical turbulence. On the other hand, it needs to be

emphasized that chaos, at least for the time being, concerns mainly irregular behaviors in the temporal evolution, and is related only to the onset mechanism of turbulence, i.e., to weak turbulence. In contrast, fully-developed turbulence involves both temporal and spatial irregularities.

## 1.2 Characterization of Chaos

A simple way to characterize attractors is via power-spectrum analysis, which is often used to qualitatively distinguish quasiperiodic or chaotic behavior from periodic structure and to identify different periods embedded in a chaotic signal. Chaos is characterized by the presence of broadband noise in the power spectrum. For example, Feigenbaum (1979b) used power-spectrum analysis to study the onset spectrum of turbulence. More sophisticated tools which are widely used for characterizing attractors include Lyapunov exponents and various definitions of dimensions.

### 1.2.1 Dimensions of attractors

In dissipative systems, the dimension  $D$  of an attractor is lower than the dimension  $k$  of the original phase space, since some modes may damp out due to dissipation. For a system whose state may be described by  $k$  variables, the corresponding phase space is a  $k$ -dimensional Euclidean space whose coordinates are those  $k$  variables, and each point in phase space represents a possible instantaneous state of the system. There are three distinct intuitive notions of dimension: one is the topological dimension related to the direction of a space (Hurewicz and Wallman, 1948), one is the fractal dimension (or Hausdorff dimension) related to the capacity of a space (Mandelbrot, 1983), and one is the information dimension related to the measurement of a space (Farmer, 1982). For simple attractors such as fixed points, limit cycles, or 2-tori, the separate notions of dimension converge to the same integer numbers. However, for chaotic (strange) attractors, these dimensions may be different, and they may be noninteger. The topological and fractal dimensions require only a metric (i.e., distance) for their definitions; whereas, the information dimension needs both a metric and a probability measure for its definition (Farmer, 1982). It is usually difficult and impractical to compute these dimensions directly. When

the Lyapunov-exponent spectrum can be obtained, it is easier to compute the Lyapunov dimension, which is related to the information dimension by the Kaplan-Yorke conjecture (Fredrickson *et al.*, 1983). It is also relatively easy to compute the correlation dimension (Grassberger and Procaccia, 1983a), which is related to the fractal dimension. The computation of the correlation dimension and related problems will be discussed in Chap. 2.

The fractal dimension mentioned above is sometimes called mono-fractal, and a multifractal spectrum is more appropriate for describing many systems. Multifractal measures are fundamentally characterized not by a single dimension, but by a dimension function (sometimes called the spectrum of singularities) which is simply related to the probability distribution (see, e.g., Lovejoy and Schertzer, 1990 and references therein). In the case of multifractality in fully-developed turbulence, She and Orszag (1991) offered an explanation for the physics behind the multiple exponents, namely, local distortion of turbulent structures which modifies the behavior of higher-order moments differentially.

The above fractals are called thin fractals to distinguish them from fat fractals which are sets with fractal structure but a nonzero measure (Eykholt and Umberger, 1988). These latter sets allow quantitative analyses of sensitivity to parameters, final-state sensitivity, and quantum chaos, but their fractal dimension is insensitive to their fractal structure, because they have the same (integer) dimension as the underlying space.

The dimension of an attractor measures to what extent the dynamics fills the phase space and provides a lower bound for the number of independent variables (degrees of freedom) necessary in a phenomenological model to adequately describe the time evolution of the system. However, the complexity of a strange attractor cannot be characterized merely by its dimension; it must be stretched and folded in some directions as well. These more subtle features can be described by Lyapunov exponents.

### 1.2.2 Lyapunov exponents of attractors

Lyapunov exponents are the average rates of exponential divergence or convergence of nearby orbits in phase space. The spectrum of Lyapunov exponents provides a quantitative measure of the sensitivity to initial conditions (i.e., the divergence of neighboring

trajectories exponentially in time), and it is the most useful dynamical diagnostic for chaotic systems. Lyapunov exponents are independent of initial conditions on any orbit (Eckmann and Ruelle, 1985). Any system containing at least one positive Lyapunov exponent is defined to be chaotic, with the magnitudes of the positive exponents determining the time scale for predictability. There are as many Lyapunov exponents as the dimension of the phase space (Guckenheimer and Holmes, 1983), and, for a system of coupled ordinary differential equations, one of these exponents is necessarily equal to zero, meaning that the change in the relative separation of initially close states on a given trajectory is slower than exponential. The negative exponents express the exponential approach of the initial states to the attractor. In any well-behaved dissipative dynamical system, the sum of all of the Lyapunov exponents must be strictly negative (Guckenheimer and Holmes, 1983). If the Lyapunov-exponent spectrum can be determined, the Kolmogorov-Sinai entropy (Kolmogorov, 1958; Sinai, 1959) can be estimated using the Pesin inequality (Eckmann and Ruelle, 1985), and the fractal dimension may be estimated from the Kaplan-Yorke conjecture (Fredrickson *et al.*, 1983), which seems to hold for typical attractors. Furthermore, the Lyapunov-exponent spectrum can be used to constrain the choice of mapping parameters in a prediction problem (Abarbanel *et al.*, 1990).

For low-dimensional systems, even without a knowledge of the exact values of the Lyapunov exponents (which are important, as discussed in the previous paragraph), a knowledge of their signs alone can provide a qualitative classification of attractors. For instance, in a three-dimensional phase space,  $(-, -, -)$  (i.e., three negative Lyapunov exponents) corresponds to a fixed point,  $(0, -, -)$  to a limit cycle,  $(0, 0, -)$  to a 2-tori, and  $(+, 0, -)$  to a strange attractor.

The Lyapunov exponents can be computed relatively easily for known simple model systems (Shimada and Nagashima, 1979). In many real world situations, however, all that is available is a time series of experimental data, and it is much more difficult to extract the Lyapunov exponents from such a series. This will be discussed in Chap. 2.

### 1.3 Application of Chaos Theory

Just as relativity eliminated the Newtonian illusion of absolute space and time, and as quantum theory eliminated the Newtonian and Einsteinian dream of a controllable measurement process, chaos eliminates the Laplacian fantasy of long-time deterministic predictability. Because of chaos, it is realized that even simple systems may give rise to and, hence, be used as models for complex behavior. Conversely, complex systems may give rise to simple behavior which may be predicted for a period within the predictability limits. Finally, and most important, the laws of scaling and complexity hold universally, caring not at all about the details of the system. Chaos leads to the unification of order and disorder, and leads to the unification of deterministic and stochastic descriptions (Lorenz, 1987). Chaos also acts like a bridge between scientists in traditionally unrelated fields. In addition, chaos forms a bridge between different fields; one example is this study itself: the unrelated studies in Chapters 2-4 are unified under chaos. Much of Lorenz's research presents good examples of how physical insights and new ideas can be gained by studying chaos (see, e.g., Lorenz, 1991a and references therein). However, the influence of this change of traditional viewpoints on the development of science and technology and on our daily life still needs some time to be fully observed, just as for the cases of relativity theory and quantum theory.

In addition, chaos offers a fresh way to proceed with observational data, especially those data which may be ignored because they proved too erratic. Most chaotic studies in the field of atmospheric science have concentrated on computing quantities characterizing attractors, such as Lyapunov exponents and fractal dimensions from observational data. Nicolis and Nicolis (1984) analyzed the time series of the isotope record of deep sea cores and obtained a low dimensionality (between three and four) for the climate system. Subsequently, Fraedrich (1986, 1987), Essex *et al.* (1987), and Keppenne and Nicolis (1989) analyzed daily average data over eastern North America and western Europe, and have likewise concluded the existence of low-dimensional attractors. Also, theories of deterministic chaos and fractal structure have been applied to data in the atmospheric boundary layer (Tsonis and Elsner, 1988), the pulse of storm rainfall (Sharifi *et al.*, 1990), and

some special atmospheric systems, such as the Southern Oscillation (Hense, 1987) and cyclone tracks (Fraedrich and Leslie, 1989; Fraedrich *et al.*, 1990). Using entire global fields of data rather than single-point time series, Pierrehumbert (1990) discussed the dimension of global atmospheric variability. Recently, Tsonis *et al.* (1991) claimed that the existence of low-dimensional attractors related to weather and climate should not be disregarded. On the other hand, there are still some doubts among researchers concerning strange attractors in the atmosphere (Pool, 1989). Ruelle (1990) discussed limitations to the Grassberger-Procaccia algorithm and found that many published estimates of fractal dimensions are spurious. Lorenz (1991b) discussed another possible reason for apparently finding low-dimensional attractors in the atmosphere.

Related to the application of chaos theory in the atmosphere, Meneveau and Sreenivasan (1987) proposed a multifractal cascade model for fully-developed turbulence. Bretherton (1990) applied this model to study the cloud-top entrainment. Lovejoy and Schertzer and their groups applied multifractals, generalized scale invariance, and intermittency to study radiation processes, cloud physics, and precipitation (see, e.g., Lovejoy and Schertzer, 1991 and references therein; Schertzer and Lovejoy, 1990 and references therein). Fractal dimensions have also been used to study pollutant dispersion problems (Gifford, 1991). More applications can be found in Schertzer and Lovejoy (1991) and Sreenivasan (1991).

Although chaos places a fundamental limit on long-term prediction, it suggests possibility for short-term prediction: random-looking data may contain simple deterministic relationships, involving only a few irreducible degrees of freedom. Therefore, chaos theory has also been used for prediction problems, especially when we lack proper initial data for a numerical prediction model or when we lack a good model (see, e.g., Abarbanel *et al.*, 1990 and references therein). This is currently a very active research area.

Another potentially important application of chaos theory is to deal with output from numerical models such as mesoscale simulations and general circulation models. As far as I know, there is still no published work in this field.

In Chap. 2, the computation of fractal dimensions, Lyapunov exponents and related techniques are discussed. In Chap. 3, the chaotic properties of observational data are

analyzed. Unlike the previous works mentioned above in our study, the predictability analysis is related to the climatic signal-to-noise ratio. In Chap. 4, the existence of chaos in daisyworld is explored. Mathematical analysis of this conceptual atmosphere-biosphere coupling model raises important questions concerning the validity and interpretation of the Gaia hypothesis. In Chap. 5, the initial adjustment process, the error growth dynamics (including the sensitivity to initial and boundary conditions as well as model parameters) of surface thermally-induced circulations are studied. The predictability as a function of the size of surface heat patches is quantitatively evaluated. The 3-D simulation is used to verify the 2-D results. As a first step, the model output is used to analyze chaotic properties, which may further our understanding of predictability problems. Finally, in Chap. 6, a summary of the principal conclusions of this study is given, and suggestions for further research are provided.

## Chapter 2

### COMPUTATION OF DIMENSIONS AND LYAPUNOV EXPONENTS

The computation of fractal dimensions and Lyapunov exponents is discussed in this chapter. More detailed discussions can be found in Zeng *et al.* (1991, 1992a,b). The phase-space reconstruction, which is related to the computation of the above quantities, is discussed in Section 2.1. The computation of fractal dimensions and related problems are discussed in Section 2.2. The computation of other dimensions is also briefly discussed in this section. In Section 2.3, the estimation of Lyapunov exponents and related problems are discussed.

#### 2.1 Phase-Space Reconstruction

For a system with known ordinary differential equations (ODEs) or difference equations, the set of all dependent variables constitutes a phase space, i.e., a Euclidean space whose coordinates are these variables. Each point in this phase space represents a possible instantaneous state of the system. A state which satisfies the governing equations is represented by a particle traveling along a trajectory in phase space. For a system with known partial differential equations (PDEs), the system can usually be studied by discretizing the PDEs, and the set of all dependent variables at all grid points constitute a phase space, which is an approximation to the original infinite-dimensional phase space. For such a system (e.g., the atmosphere), an additional difficulty is that the initial values of the system may be unknown. However, a time series of a single variable of a complex system may be available, and this allows the attractor of the system to be reconstructed.

When dealing with a time series  $x_i = x(i\Delta t)$  ( $i = 1, 2, \dots, N$ ), where  $N$  is the number of observations and  $\Delta t$  is the time interval between measurements, the attractor can be

reconstructed in a  $k$ -dimensional phase space of delay coordinates by forming the vectors (Takens, 1981)

$$\vec{x}_i = (x_i, x_{i+m}, \dots, x_{i+(k-1)m})^T, \quad (2.1)$$

where  $\tau = m\Delta t$  is the delay time, and the integer  $m$  must be chosen appropriately, as will be discussed later. By extending the Whitney embedding theorem, Takens (1981) showed that, for any system, an embedding can be obtained from a single time series of infinite precision by using  $(2\nu_s + 1)$  delay coordinates, where  $\nu_s$  is the fractal dimension. The physical reason for a possible phase-space reconstruction is that nonlinear systems are usually characterized by self-interaction, so that a single variable may carry information about the whole system. However, Takens' theorem gives little guidance about practical considerations for reconstructing a good phase space; e.g., the reconstruction may depend upon the coupling strength of this variable with rest of the variables of the system. When delay coordinates are used, it is also difficult to interpret the results physically; in other words, relating the local structures based on the delay coordinates back to physical principles or existing theories is often difficult, if not impossible. Furthermore, Takens' theorem does not apply to systems with noise, such as that found in observational time series (Breedon and Hübler, 1990). Recently, however, Takens' theorem has been extended by using statistical methods to incorporate the effects of observational noise and estimation error in the linear or polynomial approximation (Casdagli *et al.*, 1991). Another method for reconstruction is the method of derivatives, numerically investigated by Packard *et al.* (1980), which is related to the reconstruction by delay coordinates described above by a linear transformation.

Another method is singular-value decomposition (SVD) (Broomhead and King, 1986). This method is also referred to as principal-component analysis or factor analysis in the statistical literature, Karhunen-Loeve decomposition in the engineering literature, and empirical-orthogonal-function analysis in the literature of atmospheric science. In the  $(k, m)$ -window, which consists of  $k$  elements of the time series separated by time intervals  $\tau = m\Delta t$ , the trajectory matrix is

$$B = N_T^{-1/2}(\bar{x}_1, \bar{x}_{1+m}, \dots, \bar{x}_{1+(N_T-1)m})^T, \quad (2.2)$$

where  $N_T \leq (N - 1 - (k - 2)m)/m$  is the number of the available vectors  $\bar{x}_i$ , as defined in Eq. (2.1), and the factor of  $N_T^{-1/2}$  has been introduced as a convenient normalization.

The covariance matrix is

$$A_{ij} = (B^T B)_{ij} = \frac{1}{N_T} \sum_{l=1}^{N_T} x_{1+(l-1)m+(i-1)m} x_{1+(l-1)m+(j-1)m}, \quad i, j = 1, 2, \dots, k. \quad (2.3)$$

Each eigenvalue  $s_i^2$  (whose square root,  $s_i$ , is called a singular value) of  $A$  gives the proportion of the variance of the time series explained by projection onto the corresponding eigenvector  $\bar{u}_i$ . Since the singular values can be ordered as  $s_1 \geq s_2 \geq \dots \geq s_k \geq 0$ , the vector  $\bar{u}_1$  corresponds to the direction of maximum variability. The space reconstructed using these eigenvectors is referred to as singular space (Broomhead and King, 1986). In general, SVD provides a convenient basis set for representing data. In practice, however, SVD is affected by noise and/or measurement error. SVD is related to the above two methods by the linear transformation  $C = BU$ , where  $B$  is given in Eq. (2.2) and the columns of the orthogonal matrix  $U$  are formed by  $\bar{u}_1, \bar{u}_2, \dots, \bar{u}_k$ .

The above three methods can sometimes be improved by linear filtering, but such filtering must be done carefully, since it may increase the dimension of the time series (Badii *et al.*, 1988).

At this time, there is no general agreement about which method is best. However, for a short time series of low precision, the simple method of using delay coordinates is widely used, and it has been shown to work reasonably well in many situations (Zeng *et al.*, 1992a,b, and references therein).

When delay coordinates are used for an infinite amount of noise-free data, the time delay  $\tau = m\Delta t$  can be chosen almost arbitrarily (Takens, 1981). However, when only a limited amount of noisy data is available, the quality of the analysis depends on the value chosen for  $\tau$ . The choice of this delay time depends sensitively on the attractor under study (Frank *et al.*, 1990). Different methods have been suggested for obtaining  $\tau$ .

The first method is the space-filling method. A two-dimensional phase space is reconstructed by  $\vec{x}_i = (x_i, x_{i+m})$  in order to visualize the trajectory. If  $\tau$  is too small, then  $x_i$  and  $x_{i+m}$  will be indistinguishable, and the trajectory will appear to lie on the diagonal. Hence,  $\tau$  must be chosen to be large enough that the trajectory fills the space. However, when  $\tau$  is too large,  $x_i$  and  $x_{i+m}$  becomes a random sequence. Thus  $\tau$  should not be any larger than necessary for the trajectory to fill the space. The trajectory can also be visualized in a three-dimensional phase space, with the resulting value of  $\tau$  expected to be similar.

Alternatively, the delay time  $\tau$  may be defined as the lag time at which the autocorrelation function drops to a threshold value. This delay time guarantees linear independence. In general, the threshold value depends on the system and the data set, and it is usually taken as either zero, 0.1, or  $e^{-1}$ , with the latter being chosen in this study. The delay times obtained for observational meteorological data (which will be discussed in Chap. 3) using the above two methods also correspond to the characteristic times between independent estimates (Madden, 1976; Madden and Shea, 1978).

A more systematic method is based on the mutual information concept (Fraser and Swinney, 1986), which measures general dependence, rather than linear dependence. For a two-dimensional embedding, the mutual information can be defined as

$$I(m) = \sum_{i=1}^{N-m} P_{i,i+m} \log_2 \frac{P_{i,i+m}}{P_i P_{i+m}}, \quad (2.4)$$

where  $P_i$  is the probability of choosing  $x_i$  when making a selection from the time series, and  $P_{i,i+m}$  is the joint probability distribution of having  $x_i$  as the first component and  $x_{i+m}$  as the second component of the vector  $\vec{x}_i = (x_i, x_{i+m})$ . The best value for  $\tau$  is then the smallest value of  $m\Delta t$  for which  $I(m)$  is a local minimum. Fraser (1989) also generalized this procedure to reconstructions of arbitrary embedding dimensions (and added an analysis that determined the required embedding dimension).

For long time series, the mutual information method may be the most comprehensive method. However, it does not provide substantially different delay times for many systems. Furthermore, in practice, when the data size is limited, it may not be possible to

compute the mutual information accurately. In contrast, the autocorrelation function can be computed from small data sets, and the value of  $\tau$  computed using this method does not differ substantially from the value based on higher-order autocorrelations. Therefore, for short time series of low precision, the simple autocorrelation method, combined with the space-filling method, may be used to determine the delay time  $\tau$  for use in defining the delay coordinates.

## 2.2 Computation of Fractal Dimensions

The fractal dimension is one of the commonly used measures of the “strangeness” of attractors. It is related to the number of degrees of freedom. It also provides statistical information about the system. Among the different procedures that have been developed to compute fractal dimensions are the nearest-neighbor method (Badii and Politi, 1985), the correlation-integral method (Grassberger and Procaccia, 1983a), and the singular-system method (Broomhead and King, 1986). Some information about the quality of the results obtained with the different methods has been reported (Holzfuss and Mayer-Kress, 1986). In practice, the correlation-integral method is the most widely used, and it is the one applied in this study. The correlation dimension  $\nu_s$ , given by Grassberger and Procaccia (1983a) provides a rigorous lower bound to the information dimension and the Hausdorff dimension, and all three are generally close in value. The correlation dimension also provides a lower bound to the number of dependent variables necessary to describe the time evolution of the dynamical system, and the Whitney embedding theorem (Takens, 1981) gives an upper bound of  $(2\nu_s + 1)$  of dependent variables needed to model the dynamics of a simple system. However, for complex systems such as the atmosphere, the conditions of the Whitney embedding theorem may not be satisfied, and this upper bound may not be valid.

In a  $k$ -dimensional phase space [cf. Eq. (2.1)], the correlation function is given by (Grassberger and Procaccia, 1983a)

$$C(r) = \lim_{N \rightarrow \infty} \frac{1}{N^2} \sum_{i,j=1}^N H(r - \|\vec{x}_i - \vec{x}_j\|) , \quad (2.5)$$

where  $N$  is the total number of data points,  $H$  is the Heaviside function defined by  $H(y) = 1$  for positive  $y$ , and  $H(y) = 0$  otherwise, and the usual Euclidean norm is used:

$$\|\vec{x}_i - \vec{x}_j\| = \left[ \sum_{l=0}^{k-1} (x_{i+lm} - x_{j+lm})^2 \right]^{1/2}. \quad (2.6)$$

In other words,  $C(r)$  is the cumulative histogram for the number of pairs of trajectory points whose distance is less than  $r$ .

The relationship between  $C(r)$  and  $r$  varies with  $r$ . When  $r$  is very small, there are insufficient statistics, and the influence of noise inherent in the system or contributed by measurements is important; whereas, for  $r$  too large, the information is affected by nonlinearity, and the slope of the curve of  $\ln C(r)$  versus  $\ln r$  is smaller than that for intermediate  $r$ . However, there exists an intermediate range of  $r$  in which this slope is almost constant; i.e.,  $C(r)$  depends upon  $r$  as

$$C(r) \sim r^\nu. \quad (2.7)$$

For each embedding dimension  $k$ , this exponent  $\nu$  can be obtained from the slope of the linear part of a plot of  $\ln C(r)$  versus  $\ln r$ . If  $\nu$  approaches a value independent of  $k$  as  $k \rightarrow \infty$  (usually  $k > 2\nu$  is sufficient), this value is defined as the correlation dimension  $\nu_c$ .

For this linear range of  $r$ , a relatively easy procedure to compute the Kolmogorov-Sinai entropy  $K$  (Kolmogorov, 1958; Sinai, 1959) was also developed by Grassberger and Procaccia (1983b). The cumulative distribution  $C_k(r)$  obtained from Eq. (2.5), where the subscript  $k$  refers to the embedding dimension, may be interpreted as the probability of finding two pieces of the trajectory whose distance remains less than  $r$  during the evolution time  $(k-1)\tau$ . When the embedding dimension is increased from  $k$  to  $k+1$  at fixed  $r$ , the change from  $C_k(r)$  to  $C_{k+1}(r)$  gives the number of pairs of such trajectories escaping from a ball of radius  $r$ . With this interpretation, it can be argued that

$$C_k(r) \sim r^\nu e^{-k\tau K}. \quad (2.8)$$

When saturation is reached for sufficiently large  $k$ , Eq. (2.8) with fixed  $\tau$  can be used to obtain the Kolmogorov-Sinai entropy  $K$ :

$$K = \frac{1}{n\tau} \ln \frac{C_k(\tau)}{C_{k+n}(\tau)}, \quad (2.9)$$

where the value of  $\tau$  should be within the linear part of the plot of  $\ln C_k(\tau)$  versus  $\ln \tau$ .

It is widely accepted now that there are limitations to the Grassberger-Procaccia algorithm when the number of data is limited. Qualitatively, because of the limitations on the number of observations, the interval in  $\tau$  for which Eq. (2.7) is valid begins to shrink as the embedding dimension  $k$  increases, and this interval becomes very small after the dimension is greater than a certain value. Similar arguments have been emphasized by Essex *et al.* (1987), and Tsonis and Elsner (1990) using the concept of critical embedding dimension  $k_c$ ; i.e., the embedding dimension above which the scaling region cannot be accurately defined. The quantitative data requirement for the Grassberger-Procaccia algorithm has been a highly debated subject in recent years, and various researchers have given different criteria. According to Ruelle (1990), at least  $M = 10^{\nu_s/2}$  data points are necessary to reliably estimate fractal dimension  $\nu_s$ , and this is the least strict of several different criteria. We will use these criteria to evaluate the reliability of low-dimensional atmospheric attractors obtained by various researchers in the next chapter.

When the Lyapunov-exponent spectrum can be obtained, the Lyapunov dimension  $D_L$  is given by the Kaplan-Yorke conjecture (Fredrickson *et al.*, 1983) which is valid for typical attractors:

$$D_L = l + \frac{\sum_{j=1}^l \lambda_j}{|\lambda_{l+1}|}, \quad (2.10)$$

where  $\sum_{j=1}^l \lambda_j \geq 0 > \sum_{j=1}^{l+1} \lambda_j$ . This dimension is usually close to the correlation dimension in value. For systems of known ODEs or mappings, the Lyapunov-exponent spectrum can be obtained, as will be discussed in the next section, and Eq. (2.10) provides a very simple method for estimating dimension. However, for a very complex system (e.g.,

the atmosphere), we cannot determine all of the Lyapunov exponents accurately from observational data, so that this relation cannot be used.

Another method for computing a dimension is the use of SVD. In principle, the local dimension can be obtained by counting the number of distinct singular values whose magnitude is appreciable, with the rest of the singular values being close to zero. If all singular values are similar in magnitude, or if they decay in a fairly uniform manner, the value of this decomposition is less clear. In the presence of noise or measurement errors, mixing may occur when the difference between two nearby singular values is comparable to the sampling error (North *et al.*, 1982). When such mixing occurs, it is generally impossible to estimate the dimension of the attractor on the basis of SVD alone (North *et al.*, 1982). Similarly, it is demonstrated in Mees *et al.* (1987) that the recovered attractor in a high-dimensional embedding space does not necessarily "nest" in the low-dimensional linear subspace determined by the SVD technique, so the SVD is often of limited value as a dimension indicator.

Another simple method (Aleksic, 1991) proposes to obtain a dimension by comparing the graphical representations of the distances between the images of close points. However, this method is quite sensitive to (even 4%) noise.

As discussed before, the fractal dimension (Hausdorff dimension), information dimension, and correlation dimension are usually different, but are usually close in value. In fact, they are only three of an infinite number of different (and relevant) generalized dimensions (multifractal dimensions) that characterize an attractor. This hierarchy of generalized dimensions  $D_q$  can be expressed as (Hentschel and Procaccia, 1983)

$$D_q = \lim_{r \rightarrow 0} \left[ \frac{1}{q-1} \frac{\ln \sum_i p_i^q}{\ln r} \right], \quad (2.11)$$

where  $p_i$  is the probability that a trajectory point falls into the  $i$ th  $k$ -dimensional box (subspace) of size  $r$  in a  $k$ -dimensional phase space. It is shown in Hentschel and Procaccia (1983) that  $D_0$  corresponds to the Hausdorff dimension,  $D_1$  to the information dimension, and  $D_2$  to the correlation dimension. A formal relationship between  $D_q$  and the spectrum of singularities  $f(\alpha)$  is derived by Halsey *et al.* (1986). Further refinements are discussed

in Lovejoy and Schertzer (1990, and references therein). In this study, only the correlation dimension is computed, and this will be discussed in the following chapters.

### 2.3 Computation of Lyapunov Exponents

For a  $k$ -dimensional known model system, a “control” trajectory  $\vec{x}(t)$  can be obtained in a  $k$ -dimensional phase space by numerically solving the governing equations. Then, by solving the linearized version of these equations, the evolution of an infinitesimal initial error vector  $\delta\vec{x}(t_0)$  with time can be described by

$$\delta\vec{x}(t) = H \delta\vec{x}(t_0), \quad (2.12)$$

where the  $k \times k$  matrix  $H$  depends upon the values of the control trajectory  $\vec{x}$  between times  $t_0$  and  $t$ . Letting  $\gamma_j$  ( $j = 1, 2, \dots, k$ ) be the square roots of the eigenvalues of  $HH^T$ , where the superscript T denotes a transpose, the Lyapunov exponents can be written as

$$\lambda_j = \lim_{t \rightarrow \infty} (\ln \gamma_j) / (t - t_0). \quad (2.13)$$

The exponents  $\lambda_j$  can be ordered as  $\lambda_1 \geq \lambda_2 \geq \dots \geq \lambda_k$ , which gives the spectrum of Lyapunov exponents. These exponents are independent of the initial condition  $\vec{x}(t_0)$  if the system is ergodic (Oseledec, 1968).

In practice, when  $(t - t_0)$  is made very large, the eigenvalues of  $HH^T$  are likely to differ by many orders of magnitude (Wolf *et al.*, 1985; Lorenz, 1984a). Furthermore, for a chaotic system, the vector  $\delta\vec{x}(t)$  tends to align with the local direction of most rapid growth, and the roundoff errors and noises may completely falsify all except the largest Lyapunov exponent (Wolf *et al.*, 1985; Lorenz, 1984a). These two problems can be circumvented by using special algorithms [e.g., Gram-Schmit (GS) orthonormalization, Householder QR decomposition, or singular-value decomposition] which decompose  $H$  into a product of factors  $T_i$  giving the evolution over a succession of subintervals between  $t_0$  and  $t$ .

In many real-world situations, however, all that is available is a time series of experimental data, and it is much more difficult to extract the Lyapunov exponents from

such a series. Only in the past few years have such methods been proposed. These methods differ only with respect to the orthonormalization method (GS orthonormalization or QR decomposition), the local mapping method (linear or higher-order polynomial), and some technical details. Early methods were based on the linearized mapping and either GS orthonormalization (Wolf *et al.*, 1985; Sano and Sawada, 1985) or QR decomposition (Eckmann *et al.*, 1986). Most of the later methods were based on Eckmann *et al.* (1986), replacing the linearized mapping with higher-order Taylor series (Briggs, 1990; Bryant *et al.*, 1990; Brown *et al.*, 1991), and/or using the singular-value decomposition technique to determine the local dimension (Stoop and Parisi, 1991). Based on the work of Sano and Sawada (1985) and Eckmann *et al.* (1986), we have recently proposed a practical method for estimating the Lyapunov-exponent spectrum from short time series of low precision (Zeng *et al.*, 1991). A comparison of different algorithms and related techniques in Zeng *et al.* (1992b) has shown that our algorithm (Zeng *et al.*, 1991) works for short time series of low precision, while most of the above methods are useful only when the time series are long and/or have high precision.

For each point  $\vec{x}_i$  of the control trajectory in  $k$ -dimensional phase space [see Eq. (2.1)], consider the shell between two spheres centered at  $\vec{x}_i$  of radii  $r_{min} < r$ , and consider the set of trajectory points  $\vec{x}_j$  within this  $i$ th shell:

$$r_{min} \leq \|\vec{x}_j - \vec{x}_i\| = \left[ \sum_{l=0}^{k-1} (x_{j+lm} - x_{i+lm})^2 \right]^{1/2} \leq r . \quad (2.14)$$

The use of a shell, rather than a ball, is to minimize the effects of noise or measurement error, since these effects are greatest when  $\|\vec{x}_j - \vec{x}_i\|$  is small.  $r_{min}$  is taken to have the magnitude of the noise length scale. The choice of the radius  $r$  is a compromise between two conflicting requirements:  $r$  must be sufficiently small that the effect of the nonlinearity can be neglected, but  $r$  must be sufficiently large that there are at least  $n_i$  [cf. Eq. (2.17)] neighbors of the control trajectory point  $\vec{x}_i$ . In practice,  $r$  is taken as the smallest value for which the shell contains somewhat more than  $n_i$  neighbors for each control trajectory point  $\vec{x}_i$ . To find the neighbors  $\vec{x}_j$  around the control trajectory point  $\vec{x}_i$  is quite time

consuming, and some efficient methods such as the box-grid approach (Kostelich and Yorke, 1990) and the tree-search algorithm (Bentley and Friedman, 1979) are proposed.

After a time  $n\Delta t$ , the small vectors  $(\vec{x}_j - \vec{x}_i)$  evolve to the small vectors  $(\vec{x}_{j+n} - \vec{x}_{i+n})$ . Suppose that the evolution of  $\vec{x}_i$  is given by the map  $\vec{x}_{i+n} = \vec{F}(\vec{x}_i)$ . Then, with the definition  $\vec{y}_{j,i} = \vec{x}_j - \vec{x}_i$ , the  $J$ th component of  $\vec{y}_{j+n,i+n}$  can be approximated by a Taylor series:

$$\begin{aligned}
y_{j+n,i+n}(J) &= x_{j+n}(J) - x_{i+n}(J) = F_J(\vec{x}_i + \vec{y}_{j,i}) - F_J(\vec{x}_i) \\
&= \sum_{l=1}^k \frac{\partial F_J}{\partial x_i(l)} y_{j,i}(l) + \frac{1}{2!} \sum \frac{2!}{l_1! l_2! \dots l_k!} \frac{\partial^2 F_J}{\partial x_i(1)^{l_1} \partial x_i(2)^{l_2} \dots \partial x_i(k)^{l_k}} \\
&\quad \times y_{j,i}(1)^{l_1} y_{j,i}(2)^{l_2} \dots y_{j,i}(k)^{l_k} + \dots + \frac{1}{M!} \sum \frac{M!}{l_1! l_2! \dots l_k!} \\
&\quad \times \frac{\partial^M F_J}{\partial x_i(1)^{l_1} \partial x_i(2)^{l_2} \dots \partial x_i(k)^{l_k}} y_{j,i}(1)^{l_1} y_{j,i}(2)^{l_2} \dots y_{j,i}(k)^{l_k} + \dots,
\end{aligned} \tag{2.15}$$

where the restrictions on the second sum are  $0 \leq l_m \leq 2$  ( $m = 1, 2, \dots, k$ ) and  $\sum_{m=1}^k l_m = 2$ , and the restrictions on the last sum are  $0 \leq l_m \leq M$  ( $m = 1, 2, \dots, k$ ) and  $\sum_{m=1}^k l_m = M$ .

The Jacobian of the underlying dynamics is given by the first term on the right-hand side of Eq. (2.15), which leads to the approximation (written in matrix form):

$$\vec{y}_{j+n,i+n} = T_i \vec{y}_{j,i} \tag{2.16}$$

[cf. Eq. (2.12)]. The coefficients in Eq. (2.15), or the matrix in Eq. (2.16), can be determined by using a least-square-error algorithm (Brown *et al.*, 1991) to fit the evolution of the small vectors  $(\vec{x}_j - \vec{x}_i)$ , where  $\vec{x}_j$  is in the  $i$ th shell. The number  $n_i$  of independent parameters for fitting a polynomial of degree  $M$  in  $k$  dimensions can be obtained from Eq. (2.15):

$$n_i = \sum_{l=1}^M \frac{(k+l-1)!}{l!(k-1)!} = \frac{(k+M)!}{k! M!} - 1. \tag{2.17}$$

Note that, to determine all of these parameters for a given  $i$ , there must be at least  $n_i$  points  $\vec{x}_j$  within the  $i$ th shell, and, in practice, more points are used to reduce the statistical scatter.

The evolution time  $n\Delta t$  in Eqs. (2.15) and (2.16) should be small enough that Eq. (2.15) is satisfied not only for  $\vec{y}_{j,i}$ , but also for  $\vec{y}_{j+n,i+n}$ . On the other hand, the evolution time should be as large as possible, so that the orientation errors associated with each evolution (i.e., with the computation of each matrix  $T_i$ ) are reduced, and the computational cost is reduced considerably. Another potential problem with a large evolution time is that, if the direction vectors  $\vec{J}_i$  (Brown *et al.*, 1991) change significantly within the evolution time interval, then different Lyapunov exponents may tend to collapse into the direction of the largest exponent, and all except the largest exponents may be overestimated. In addition, for attractors with a multi-lobed structure, such as the Lorenz attractor (Lorenz, 1963), two neighboring points  $\vec{x}_j$  and  $\vec{x}_i$  may eventually evolve along different lobes, leading to erroneous Lyapunov exponents.

When the evolution time is taken as the delay time, i.e.,  $n = m$ , the matrix  $T_i$  in Eq. (2.16) is very simple: it consists of 1's just above the diagonal and 0's elsewhere, except for the last row of elements. This may save some computational time [though maybe not much (Brown *et al.*, 1991)]. Furthermore, our computations have shown that results using  $n = m$  are usually as good as, or even better than, those for  $n \neq m$  (Zeng *et al.*, 1991). Therefore, it seems reasonable to use  $n = m$  in the computation of the Lyapunov exponents.

A sufficient condition for the delay coordinates to reconstruct an attractor with fractal dimension  $\nu_s$  is that the embedding dimension be greater than or equal to  $2\nu_s + 1$ . This embedding dimension is called the global dimension  $d_G$ . Under this condition, intersections of trajectories on the attractor are avoided. However, since  $d_G$  is greater than  $\nu_s$ , there will be  $d_G - \nu_s$  spurious exponents caused by noise, which is infinite-dimensional, and by nonlinearity, since the lower-order coefficients in the fitting polynomial will be altered from their true values in attempting to fit the unrepresented higher-order nonlinear curvature. Therefore, a lower local dimension  $d_L$  is used to construct the matrix  $T_i$  by several researchers (Eckmann *et al.*, 1986; Bryant *et al.*, 1990; Brown *et al.*, 1991). On the other hand, for short time series of low precision, the embedding dimension cannot be made too large, due to the limited number of data. Furthermore, it is best to have

as few free parameters as possible. Therefore, for short time series of low precision, it is probably not an advantage to use different global and local dimensions, and several researchers (Wolf *et al.*, 1985; Sano and Sawada, 1985; Briggs, 1990; Zeng *et al.*, 1991) have used  $d_G = d_L$  successfully in their studies, and it is used in this study.

The linear approximation of Eq. (2.16) places a twofold burden on the Jacobian  $T_i$  (Brown *et al.*, 1991): it must yield the correct Lyapunov exponents, and, at the same time, map  $\vec{y}_{j,i}$  into  $\vec{y}_{j+n,i+n}$ . When the higher-order polynomial approximation of Eq. (2.15) is used, the latter burden is removed; i.e., the higher-order polynomial is responsible for mapping  $\vec{y}_{j,i}$  into  $\vec{y}_{j+n,i+n}$ , and its first term involving  $T_i$  is responsible only for obtaining the correct Lyapunov exponents. On the other hand, when the higher-order polynomial is used, the minimum number  $n_i$  of points  $\vec{x}_j$  in the  $i$ th shell can be seen from Eq. (2.17) to increase rapidly; e.g., for a local embedding dimension of  $k = 5$ , and Taylor series of orders  $M = 1, 2, 3, 4$ , and  $5$ , these minimum numbers are  $n_i = 5, 20, 55, 125$ , and  $251$ , respectively. Furthermore, many more neighboring points are needed in practice to improve statistical accuracy. This leads to the two disadvantages of higher-order Taylor series: the computation time is larger, and, more important, the data set must be larger. These disadvantages become more significant for noisy data sets, where  $r_{min}$  must be made larger. Therefore, the higher-order polynomial approximation may be expected to improve the estimation of the Lyapunov exponents relative to the linear approximation only when a very long time series of high precision is used, as demonstrated by several researchers (Briggs, 1990; Bryant *et al.*, 1990; Brown *et al.*, 1991). Especially, the higher-order polynomial approximation greatly improves the computation of the negative exponents, and helps to identify spurious positive exponents.

The negative Lyapunov exponents describe the exponential approach of the initial states to the attractor. The possibility of obtaining reasonable negative Lyapunov exponents depends on their magnitudes and the signal-to-noise ratio of the data (Sano and Sawada, 1985; Zeng *et al.*, 1991). For post-transient, model-generated or observational data, the attractor becomes very thin in the directions associated with the negative exponents, and, in general, it is impossible to estimate these exponents accurately. However,

the use of the linear or higher-order polynomial approximation implicitly assumes analyticity of the local neighborhood-to-neighborhood maps in phase space, which extend off of the attractor, thus allowing analytic continuation away from the given data. Hence, when noise is absent, the higher-order polynomial gives a better local mapping on fine scales and leads to improved estimates of the negative exponents as mentioned above.

The identification of the spurious exponents is related to the computation of the principal-direction vectors  $\vec{J}_i$  along which the Lyapunov exponents are obtained (Brown *et al.*, 1991). Once the  $\vec{J}_i$  are obtained, the data thickness in each of these directions can be computed. The thickness is essentially the root-mean-square displacement of the data points within a local neighborhood in the  $\vec{J}_i$  direction, with corrections for the curvature of the data set (Bryant *et al.*, 1990). Since a true positive exponent should exhibit significant thickness, a spurious positive exponent may be identified by comparing the magnitude of its thickness with those of the true positive exponents. As shown in Table 2 of Bryant *et al.* (1990), when a higher-order polynomial is used, it is easier to identify spurious positive exponents.

When only a short time series is available, the advantages of a higher-order polynomial map may disappear. We will illustrate this qualitatively with a simple example. Figure 2.1 shows the mean error growth for the logistic map  $z_{n+1} = 3.8z_n(1 - z_n)$ . The curve is characterized by the initial exponential stage, the intermediate quasi-linear stage, and the final saturation stage. All attractors and, more generally, all unstable dynamical systems having the property of mixing are expected to give rise to similar behavior (Nicolis and Nicolis, 1991). The first stage reflects local (linearized) properties, and the positive Lyapunov exponent can be obtained from the error growth in this stage. The remaining two stages depend on global properties (Nicolis and Nicolis, 1991). Suppose that the radius  $r$  in Eq. (2.14) is within the first stage for linear maps. When the higher-order polynomial map is used for a short time series, in order to obtain enough neighboring trajectory points, it may become necessary to increase the radius  $r$ , and this may lead to the inclusion of points in the intermediate stage. In this scenario, the Taylor series of higher order will not lead to a good estimate of the positive exponent, since the intermediate stage is determined by the global properties of the system.

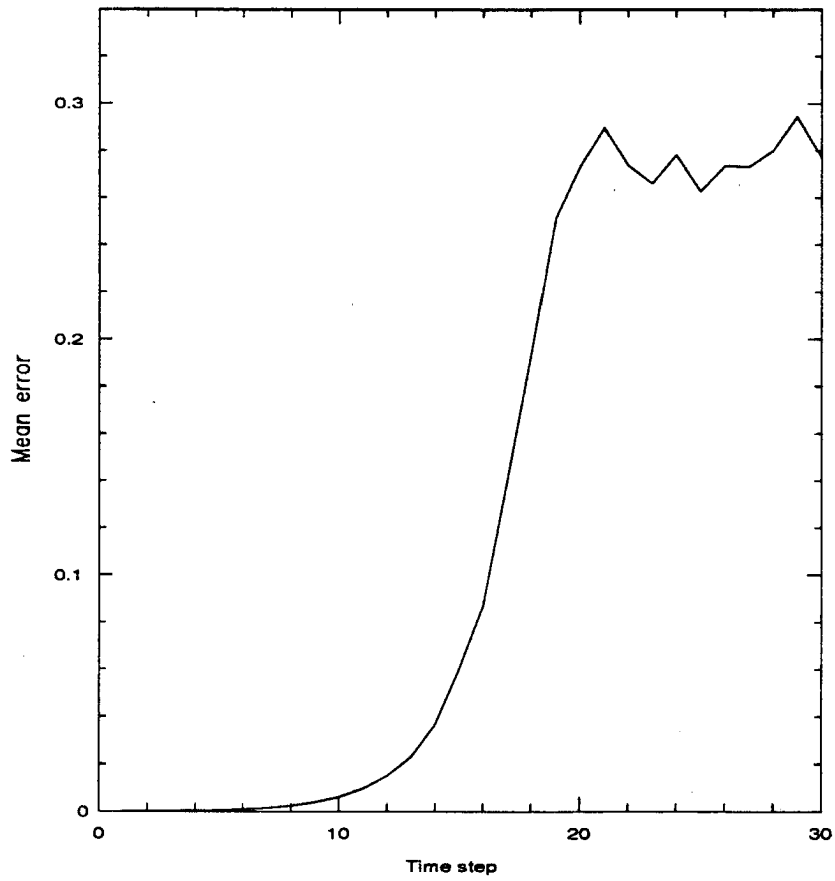


Figure 2.1: Mean-error growth for the logistic map  $z_{n+1} = 3.8z_n(1 - z_n)$ .

Also, when the higher-order fitting is used, large matrices need to be inverted in the least-square fitting. Sometimes, all of the points in a neighborhood of the control trajectory point  $\bar{x}_i$  lie along only a few directions; i.e., within the available resolution, the dimension of the attractor appears to be lower than the true fractal dimension of the system. Although it is possible to measure the expansion rates along the unstable manifold at  $\bar{x}_i$ , there are not enough data points in the other directions to estimate the contraction rates. In such a case, any attempt to estimate the Lyapunov-exponent spectrum using a local embedding dimension greater than or equal to the fractal dimension will result in large relative errors in the estimate of the Jacobian elements (Eckmann and Ruelle, 1985; Kostelich and Yorke, 1990). This kind of least-squares problem is ill-conditioned. Because of this, the matrix inversion problem is sensitive to (even small) noise in the data, especially when the matrix is large. Therefore, it is not surprising that the estimation of Lyapunov exponents (positive, zero, and negative) using Taylor series of higher order is reported to be sensitive to even small noise (Briggs, 1990; Bryant *et al.*, 1990; Brown *et al.*, 1991). In contrast, when the linear map is used together with other appropriate considerations (Zeng *et al.*, 1991), it is shown that the Lyapunov-exponent spectrum can be reasonably obtained from short time series of low precision. Therefore, the linear map is used in this study.

In the linearized case, the matrix  $T_j$  can be successively orthonormalized to avoid the two problems mentioned in the paragraph after Eq. (2.13). One such algorithm, which has been widely used, is Householder QR decomposition (Eckman and Ruelle, 1985):

$$T_{1+jn}Q_j = Q_{1+j}R_{1+j}, \quad j = 0, 1, \dots, K-1, \quad \text{or} \quad (2.18)$$

$$T_{1+jn} = Q_{1+j}R_{1+j}Q_j^{-1}, \quad j = 0, 1, \dots, K-1, \quad (2.19)$$

where  $Q_j$  is an orthogonal matrix,  $R_j$  is an upper-triangular matrix with non-negative diagonal elements, and  $K \leq (N - (k-1)m - 1)/n$  is the number of subintervals. The first orthogonal matrix  $Q_0$  may be chosen arbitrarily, and it is usually taken to be the unit matrix for convenience. If each  $T_j$  is invertible, then this decomposition is unique.

Multiplying the matrices  $T_i$  for the subintervals yields the matrix  $H$  for the entire interval:

$$H = T_{1+(K-1)n} T_{1+(K-2)n} \dots T_1 = Q_K R_K R_{K-1} \dots R_1 Q_0^{-1}. \quad (2.20)$$

Since each  $R_i$  is an upper-triangular matrix,  $R = R_K R_{K-1} \dots R_1$  is also upper triangular, and its eigenvalues are  $R_{ll} = (R_K)_{ll} (R_{K-1})_{ll} \dots (R_1)_{ll}$ , where  $(R_i)_{ll}$  is the  $l$ th diagonal element of  $R_i$ . Also, since each  $Q_i$  is an orthogonal matrix, then  $Q_i^T = Q_i^{-1}$ , and Eq. (2.20) yields

$$H H^T = Q_K R R^T Q_K^{-1}, \quad (2.21)$$

which means that  $H H^T$  is an orthogonal transformation of  $R R^T$ , so that the eigenvalues of  $H H^T$  are  $R_{ll}^2$ . Therefore, we can obtain the Lyapunov exponents from Eq. (2.13):

$$\lambda_l = \frac{1}{n\Delta t K} \ln \prod_{j=1}^K (R_j)_{ll} = \frac{1}{n\Delta t K} \sum_{j=1}^K \ln (R_j)_{ll}, \quad l = 1, 2, \dots, k. \quad (2.22)$$

The QR decomposition can also be performed using GS orthonormalization, as has been done by several researchers (Shimada and Nagashima, 1979; Wolf *et al.*, 1985; Sano and Sawada, 1985), although these researchers did not refer formally to QR decomposition (Geist *et al.*, 1990). However, Householder triangularization is preferable to GS orthonormalization, since Householder triangularization leads to (numerically determined) matrices which are more nearly orthogonal. Furthermore, it is very stable numerically, and, in fact, the sizes of the eigenvalues do not lead to problems (Eckmann and Ruelle, 1985). Therefore, only the Householder QR decomposition is used in this study.

We have tested our algorithm on various model systems, including the Lorenz equations (Lorenz, 1963) and the Rossler equations (Rössler, 1976), which are finite-dimensional systems, and the Mackey-Glass equations (Mackey and Glass, 1977), which constitute an infinite-dimensional system. The  $x$  components of numerical data for these systems are treated as experimental data. The first two systems are solved by the Runge-Kutta method, and the last system is solved by a very efficient algorithm of second-order precision (Grassberger and Procaccia, 1983c). We use a time step  $\Delta t = 0.01$  for the Lorenz

equations and  $\Delta t = 0.1$  for the Rössler equations. A time step of  $(0.01)T$ , where the parameter  $T$  is given in Table 2.1, is used to integrate the Mackey-Glass equations. However, we then include only every fifth value in our data set, producing a time series with  $\Delta t = 0.05T$ , so that the delay time  $\tau$  is not too large compared with  $\Delta t$  [usually,  $\tau \approx 10\Delta t$  is desired (Atmanspacher *et al.*, 1988)].

The first 10,000 data are discarded from the generated time series to eliminate transients, and the number  $N$  of observations is taken to be 5000, except for the Mackey-Glass equations with  $T = 30$ , for which a 5-dimensional phase space is used, and we take  $N = 10,000$ . For the Lorenz and Rössler equations, all values are rounded off to the first decimal, producing a precision of  $10^{-1}$ , and, for the Mackey-Glass equations, all values are rounded off to a precision of  $10^{-2}$  (this is because the horizontal extent of the attractor is much smaller in this case). We take  $K = \min(2000, (N - (k - 1)m - 1)/m)$  to guarantee saturated Lyapunov exponents, although convergence of  $\lambda_i$  is actually reached with fewer matrices (Fig. 2.2 shows the convergence of  $\lambda_i$  for the Mackey-Glass equations). The autocorrelation function is also illustrated in Fig. 2.2, and it is seen that the delay time  $\tau$  (i.e., the e-folding time of the autocorrelation curve) is about  $9\Delta t$ .

Table 2.1 shows the computed Lyapunov-exponent spectrum for the various model systems described above. The error bars are computed from a few runs with changes in the parameters  $\tau$ ,  $\tau_{\min}$ , and  $r$ . It is seen that all error bars are relatively small, which shows that the results from our algorithm are insensitive to the choice of these parameters. For the Lorenz equations, the computed value of the largest positive Lyapunov exponent  $\lambda_1$  differs from the accepted value by less than 9%. Since the value obtained for  $\lambda_2$  is only about 3% of  $\lambda_1$ , its relative error is very large. However, one exponent must be zero, and this exponent is easily identified as  $\lambda_2$ , so that the relative error for  $\lambda_2$  has little meaning. For the Rössler equations,  $\lambda_1$  is obtained with a relative error less than 7%, and  $\lambda_2$  is less than 7% of  $\lambda_1$ . For the Mackey-Glass equations with  $T = 23$  and only 5000 data points,  $\lambda_1$  is obtained with a relative error less than 2%, and  $\lambda_2$  is less than 1% of  $\lambda_1$ . For the Mackey-Glass system with  $T = 30$ , a 5-dimensional phase space is used, requiring 10,000 data points, rather than 5000, so that the density of data points defining the attractor is

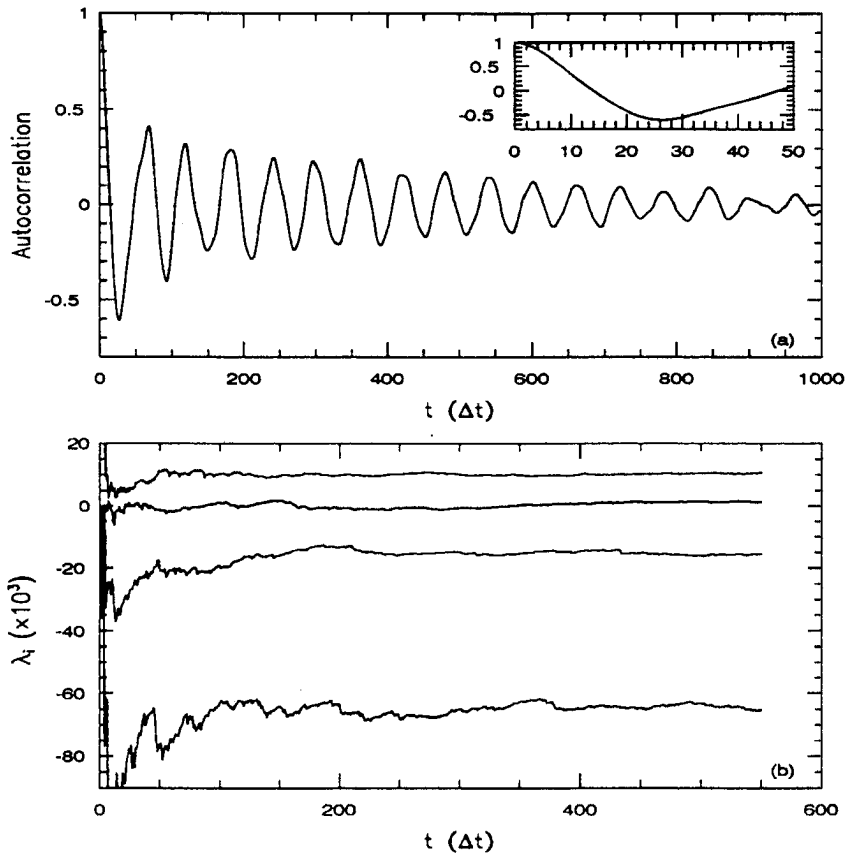


Figure 2.2: (a) Autocorrelation function and (b) convergence of Lyapunov exponents for the Mackey-Glass equations with parameters  $a = 0.2$ ,  $b = 0.1$ ,  $c = 10$ ,  $T = 23$ , and other parameters as described in the text. The inset graph is a magnification of the region close to the origin in a).

still acceptable. In this case,  $\lambda_1$  is obtained with a relative error less than 6%, and the second positive exponent  $\lambda_2$  is also obtained with a relative error of only about 11%. When data of higher precision was used, much smaller relative errors were obtained; however, given the low precision of this data (i.e., the high noise level), better agreement with the values in the absence of noise is not to be expected.

The possibility of obtaining reasonable negative Lyapunov exponents depends on their magnitudes and the signal-to-noise ratio of the data (Sano and Sawada, 1985). Since a precision of  $10^{-1}$  or  $10^{-2}$  is prescribed (i.e., the signal-to-noise ratio of the data is low), and  $|\lambda_3|$  is more than a hundred times larger than  $\lambda_1$  for the Rössler equations, the computed  $|\lambda_3|$  is too small compared with the reported  $|\lambda_3|$ . However, when the absolute values of the negative exponents are comparable with  $\lambda_1$ , as for the Mackey-Glass equations with  $T = 30$  or  $23$ , we obtain negative exponents which are comparable to the reported values. Therefore, using various known model systems, both finite- and infinite-dimensional, we have shown that our algorithm can be used to evaluate the Lyapunov-exponent spectrum from only 5000 data points of very low precision ( $10^{-1}$  or  $10^{-2}$ ) in a phase space whose dimension is less than 5, and from 10,000 points of low precision in 5-dimensional phase space.

In summary, the computation of Lyapunov exponents and related techniques are thoroughly reviewed. This computation is simple in principle but very subtle in practice. Based on theoretical reasoning and our experiences, suitable options are selected to constitute our method. All parameters are tuned so that no adjusting of free parameters is needed. Besides, using known model systems, it is found that our method can be used to obtain reasonable results from short time series of low precision. Therefore, our algorithm is particularly easy to apply and may find widespread applications in practice.

Table 2.1: Lyapunov-exponent spectrum for various known model systems. All parameters other than those given in the Table are as described in the text. The reported values are based on Wolf *et al.* (1985), except for the Mackey-Glass equation with  $\tau = 9\Delta t$ , for which the reported values are from Grassberger and Procaccia (1984).

System	Reported $\lambda_i$ ; (in the absence of noise)	Computed $\lambda_i$ ; (in the presence of noise)
Lorenz ( $\tau = 20\Delta t$ ) ( $\sigma = 16$ , $b = 4.0$ , $R = 45.92$ ) ( $N = 5000$ , $10^{-1}$ precision)	1.50	$1.63 \pm 0.15$
	0.00	$0.05 \pm 0.25$
	-22.46	$-3.59 \pm 0.41$
Rossler ( $\tau = 12\Delta t$ ) ( $a = 0.15$ , $b = 0.2$ , $c = 10$ ) ( $N = 5000$ , $10^{-1}$ precision)	0.090	$0.096 \pm 0.008$
	0.00	$-0.006 \pm 0.004$
	-9.8	$-0.735 \pm 0.057$
Mackey-Glass ( $\tau = 9\Delta t$ ) ( $a = 0.2$ , $b = 0.1$ , $c = 10$ , $T = 23$ ) ( $N = 5000$ , $10^{-2}$ precision)	$0.00956 \pm 0.00005$	$0.00938 \pm 0.00040$
	0.00000	$0.00008 \pm 0.00020$
	$-0.0119 \pm 0.0001$	$-0.0160 \pm 0.0010$
	$-0.0344 \pm 0.0001$	$-0.0734 \pm 0.0227$
Mackey-Glass ( $\tau = 9\Delta t$ ) ( $a = 0.2$ , $b = 0.1$ , $c = 10$ , $T = 30$ ) ( $N = 10,000$ , $10^{-2}$ precision)	0.0071	$0.0075 \pm 0.0007$
	0.0027	$0.0030 \pm 0.0010$
	0.000	$-0.0027 \pm 0.0010$
	-0.0167	$-0.0156 \pm 0.0006$
	-0.0245	$-0.0394 \pm 0.0064$

## Chapter 3

# FRACTAL DIMENSION AND PREDICTABILITY OF THE ATMOSPHERE

A huge amount of observational data has been accumulated in the past one hundred years in different branches of science (including atmospheric science), but the way to extract useful information from them is quite limited: most of the time, statistical methods are used. In this chapter, the chaos theory discussed in the previous chapter is used to study fractal structure and predictability for observational atmospheric data. More detailed discussion is given in Zeng *et al.* (1992a). The analyzed data is discussed in Section 3.1. The fractal dimension and the controversial issue of the existence of low-dimensional attractors in the atmosphere are discussed in Section 3.2. Atmospheric predictability is discussed in Section 3.3.

### 3.1 The Data

The data utilized in this study include the daily surface temperature (ST) over a period of 100 years (1/1, 1889 – 1/31, 1989) and the daily surface pressure (SP) over a period of 90 years (6/1, 1889 – 12/31, 1979, except the periods 8/1, 1940 – 10/31, 1940 and 9/1, 1961 – 12/31, 1961) observed in Fort Collins, Colorado. Also used are the surface temperatures over a period of 39 years (1/1, 1947 – 12/31, 1985) observed in Los Angeles, California. There are a limited number of missing data (less than 1%) in the above time series, and linear interpolations in time were used to fill in for these missing data. These two stations of Fort Collins and Los Angeles in the United States were selected in this study based on the climatic signal-to-noise ratio (SNR), which is lower in Fort Collins and higher in Los Angeles (Madden and Shea, 1978).

We also use the sea surface temperature (SST) and sea surface pressure (SSP) of two regions (BOX 244:  $20^{\circ}$ – $30^{\circ}$  N,  $300^{\circ}$ – $310^{\circ}$  W; BOX 139:  $50^{\circ}$ – $60^{\circ}$  N,  $330^{\circ}$ – $340^{\circ}$  W) over the North Atlantic Ocean, with the SNR being relatively lower in BOX 139 and higher in BOX 244 (Madden, 1976). Daily average data were computed from the Compressed Marine Reports (CMR5) of the Comprehensive Ocean-Atmosphere Data Set (COADS) (Woodruff *et al.*, 1987). COADS is widely accepted as the best data set over the global ocean, with state-of-the-art data quality control. Since the number of global marine reports were relatively small during World War II, only the data from 1/1, 1950 – 12/31, 1987 are used. In addition, our computations show that there is a considerable number of missing daily observations for  $2^{\circ} \times 2^{\circ}$ ,  $2^{\circ} \times 10^{\circ}$ , or  $5^{\circ} \times 5^{\circ}$  areas within BOX 244 and BOX 139. Therefore, we only used the  $10^{\circ} \times 10^{\circ}$  box (i.e., BOX 244 and BOX 139) to compute time series of SST and SSP, with a small number of missing data for which linear interpolations were used to fill in the voids. Since the observational data at different stations over the whole of western Europe seem to derive from a single deterministic dynamical system (Keppenne and Nicolis, 1989), it is not unreasonable to expect that the averaging of observations within a  $10^{\circ} \times 10^{\circ}$  box over an ocean can only slightly affect the computations of chaotic properties from the time series.

In an effort to minimize the effects of seasonal variations of temperature, a mean temperature is computed for each day by averaging temperatures over the record for that day of every year. These daily means are then subtracted from each daily value. For brevity, the term temperature is used to refer to the temperature perturbation in subsequent sections of this chapter. The above procedure does not apply to the observational values of the pressure. The total numbers of data points are given in Table 3.3.

In this chapter, we analyze not only the daily data described above, but also winter/summer data (daily data of winter/summer seasons which last 120 days commencing on November 1 and May 1, respectively).

### 3.2 Fractal Dimensions of Weather Attractors

The phase space reconstruction by delay coordinates [cf. Eq. (2.1)], discussed in Sec. 2.1, is used in this chapter. The time delay  $\tau$  is obtained by the space-filling method and

by computing the autocorrelation function, as discussed in Sec. 2.1. As an example, Fig. 3.1 depicts the time dependence of the surface temperature for the Fort Collins station and gives a two-dimensional view of the trajectory with  $\tau = 3$  days (or  $m = 3$ ). It is seen that the trajectory fills the entire space, suggesting that the data are independent for  $\tau = 3$  days (and that the system is in a phase space of greater than two dimensions). The corresponding autocorrelation function is given in Fig. 3.1c. It is seen that  $\tau$ , taken as the e-folding time, can be selected as 3 days. In this way,  $\tau$  is selected in the range from 2 to 10 days for temperature or pressure data at the different locations, and these choices are shown in Table 3.1. These values also correspond with the characteristic times between independent estimates (Madden, 1976; Madden and Shea, 1978).

The existence of chaos can be verified and the strange attractors can be characterized by examining the power spectra and computing fractal dimensions and Lyapunov exponents. Before we discuss the fractal dimensions, we present a brief discussion of power-spectrum analyses.

Power-spectrum analysis is often used to qualitatively distinguish quasiperiodic or chaotic behavior from periodic structure, and to identify different periods embedded in a chaotic signal. Chaos is characterized by a power spectrum of continuous appearance. Fig. 3.2 shows such a power spectrum for the surface temperature at Fort Collins. There is no clear peak corresponding to the annual cycle, since this annual cycle has been removed before computation by subtracting the daily averages. However, such a peak does appear in the power spectrum of surface pressure data, which is not shown here. It is also seen from Fig. 3.2, and from the power spectra of all other analyzed data that the spectra tend to resemble white noise beyond a cutoff frequency of about 0.4 cycles per day. This is consistent with the result of Keppenne and Nicolis (1989), which implies that a cutoff frequency of 0.4 cycles per day may be very common in the power spectra of any daily average data in the atmosphere. On the other hand, the power spectrum itself cannot distinguish chaotic signals from noisy periodic or quasiperiodic signals. Therefore, the computation of fractal dimensions or Lyapunov exponents becomes necessary to verify the existence of chaos and extract the dynamics from the time series.

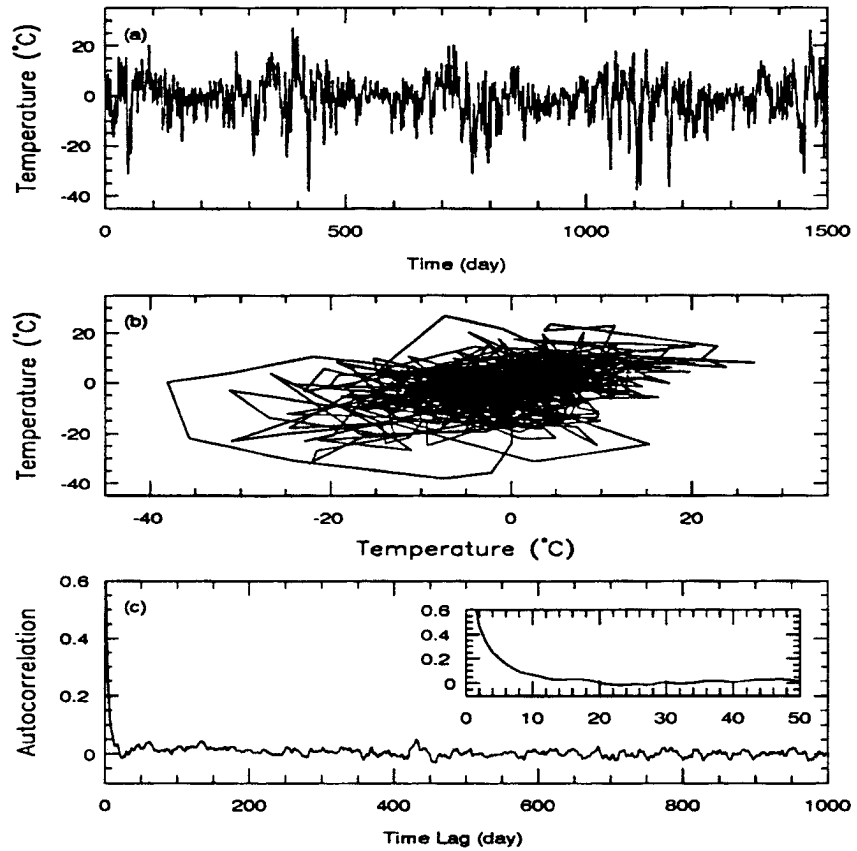


Figure 3.1: (a) Time evolution of the surface temperature at Fort Collins, Colorado; (b) time trajectory of the above time series evolving in a two-dimensional phase space of time-delay coordinates with  $\tau = 3$  days; (c) autocorrelation function of the above time series. The inset graph is a magnification of the region close to the origin in (c).

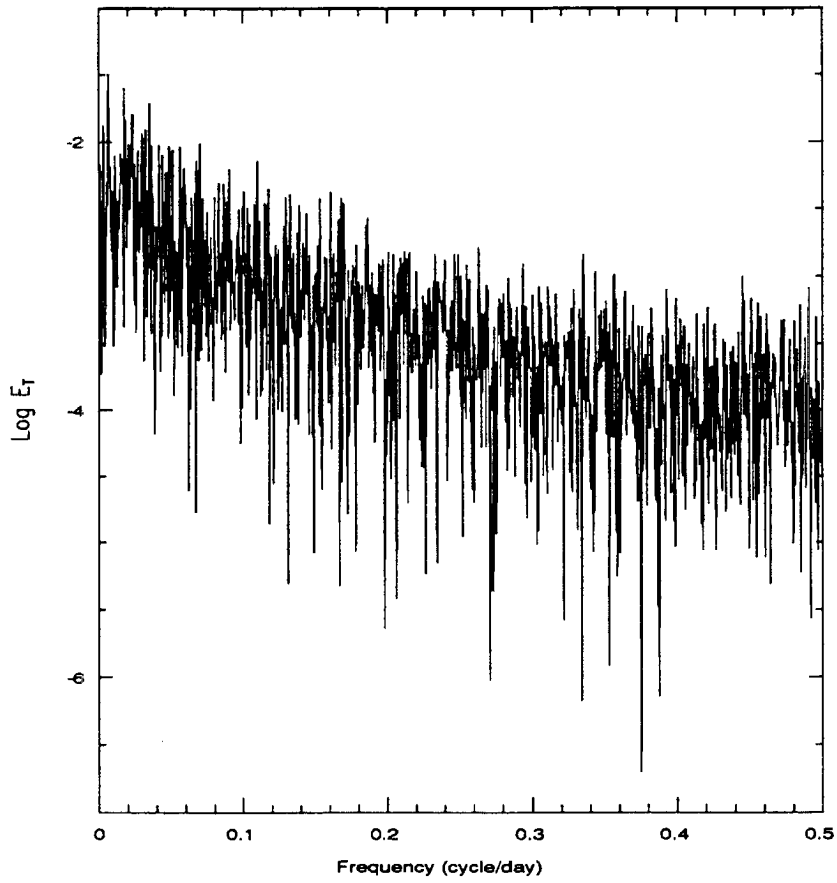


Figure 3.2: Power spectrum  $E_T$  of the daily surface temperature at Fort Collins, Colorado.

The attempts to compute fractal dimensions in the past have been motivated by the speculation that climatic fluctuation may be governed by low-dimensional attractors. We will show that, at least for surface observational daily data, no low-dimensional attractors exist. Even if the saturated fractal dimension  $\nu_s$  can be obtained, it may still be impossible to estimate the sufficient number of dependent variables needed to model the atmospheric dynamics, and it is impossible to construct simple equations to describe the dynamics. This does not necessarily mean that all calculations related to fractals in the atmosphere are useless. Pierrehumbert (1990) argued that they may tell us something about the statistics of atmospheric variability. The dynamical aspects of the fractality have also been considered for 2-D turbulence by Osborne and Caponio (1990).

Once the phase space is reconstructed, the correlation dimension  $\nu_c$  can be computed, as discussed in Sec. 2.2. Fig. 3.3 shows the plot of  $\ln C(r)$  versus  $\ln r$  for embedding dimensions  $k = 5, 7, \dots, 19$  for the sea surface pressure at BOX 139. The value of  $\nu$  is obtained from Eq. (2.7) in the intermediate range of  $r$  in which the slope is almost constant. Fig. 3.4 shows the dimensionality  $\nu$  of the weather attractor as a function of the number  $k$  of phase-space coordinates for the same time series. It is seen from Fig. 3.4 that saturated values seem to be approached. However, if we look at Fig. 3.3 carefully, we can see that, consistent with the qualitative limitation to the Grassberger-Procaccia algorithm discussed in Sec. 2.2, the interval of almost constant slope is very small when  $k > 13$ . Furthermore, the number of data is less than the quantitative requirement, i.e.,  $10^{\nu_c/2}$ , of Ruelle (1990). Therefore, the fractal dimensions obtained from this data set are actually spurious.

Table 3.1 summarizes the dependence of  $\nu$  on  $k$  for all data. Though saturation values seem to be approached for the sea surface pressure at BOX 244 and BOX 139, or for the surface temperature at Los Angeles, they are unreliable based on the above qualitative and quantitative arguments. It is also found from Table 3.1 that no saturation values can be reached for the sea surface temperatures at BOX 139 or BOX 244, or for the surface pressure and temperature at Fort Collins. Therefore, we cannot obtain saturated fractal dimensions for all data sets in the paper. For the total length of our data, we can conclude only that the saturated fractal dimension is well above 8.

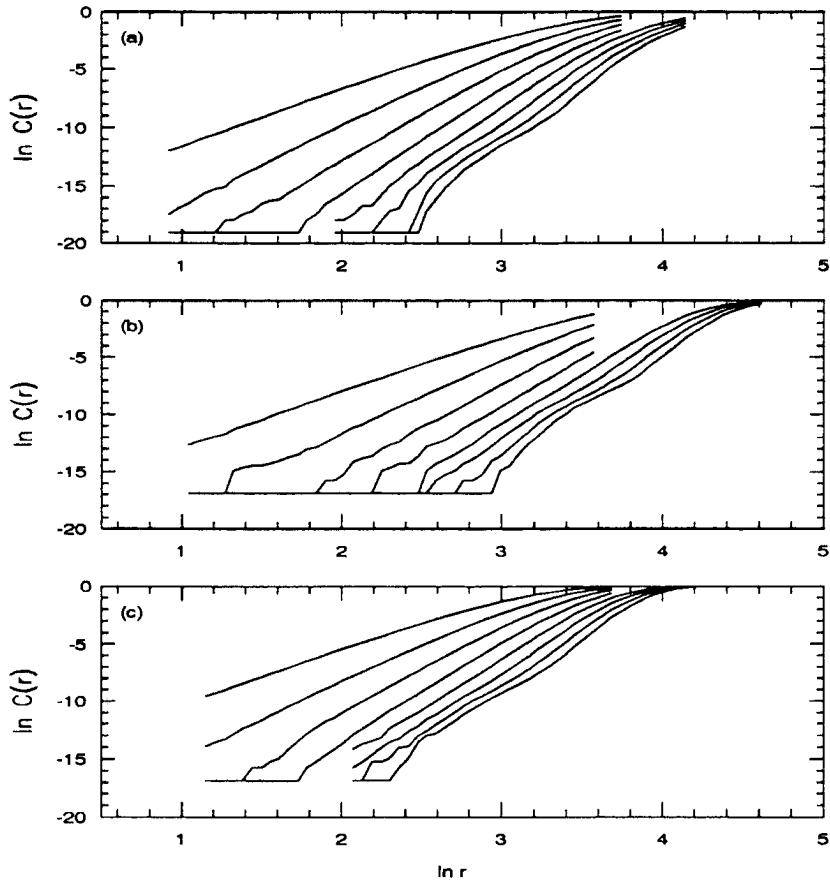


Figure 3.3: Plots of  $\ln C(r)$  versus  $\ln r$  for embedding dimensions  $k = 5, 7, \dots, 19$  (ordered from left to right) for the sea surface pressure at BOX 139. (a) daily data; (b) winter data; (c) summer data.

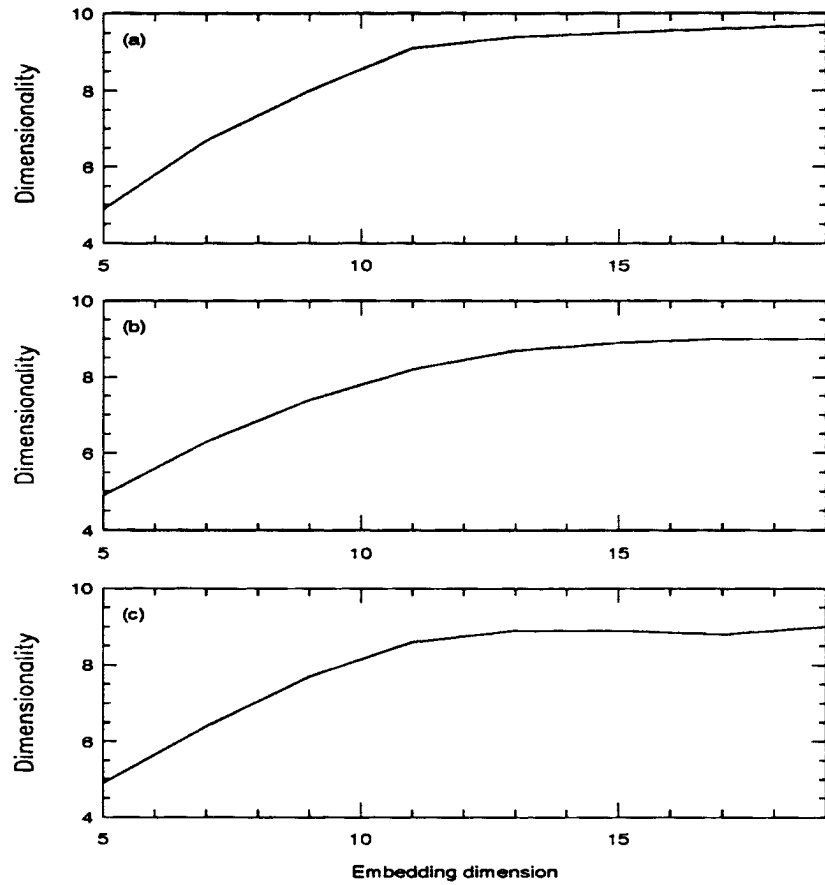


Figure 3.4: Plots of the dimensionality  $\nu$  as a function of embedding dimension  $k$  for the same circumstances as in Fig. 3.3.

We have also computed the dependence of  $\nu$  on  $k$  for random data produced by a random-number generator. It is found that the relationship between  $\nu$  and  $k$  for the observational data is similar to that for random data of a similar length (number of observations) (note: for random data of infinite length,  $\nu = k$ ). However, the above data are not random, as shown by their power spectra and autocorrelation functions (note: for Gaussian white noise, the autocorrelation function is zero; i.e., random data are independent of each other). The above results only show that the correlation dimension  $\nu$ , is so large that even an embedding dimension of  $k = 19$  is not sufficient; i.e., the dynamics of the weather attractors are controlled by too many degrees of freedom, and there exist no low-dimensional attractors.

Caputo *et al.* (1986) pointed out that saturation could be reached to obtain spurious correlation dimensions even in very-high-dimensional embeddings for any dynamical system whatsoever, including cases of infinite-dimensional, stochastic signals. Recently, Osborne and Provenzale (1989) proved that a simple class of colored random noises whose power spectrum shows a power-law decay have a finite and predictable value for the correlation dimension. Therefore, it is necessary to verify that the observed data are indeed deterministic chaos rather than colored noise. First, the autocorrelation function approaches zero slowly for all data (see, e.g., Fig. 3.1c). Second, it is impossible to fit a power law to the spectrum over the whole range of frequencies (see, e.g., Fig. 3.2). Finally, the exponent of the power-law fit to the spectrum in Fig. 3.2 is about 1.7, which would indicate a fractal dimension of only about 2.9 for colored noise (Osborne and Provenzale, 1989). This value is much smaller than those in Table 3.1. Therefore, we can conclude that the data are not colored noise.

Table 3.2 shows the values of Kolmogorov-Sinai entropy  $K$  computed from Eq. (2.9) for the sea surface pressures at BOX 244 and BOX 139 and the surface temperature at Los Angeles, where spurious saturated fractal dimensions are reached. The error-doubling time  $T$ , which is also given in Table 3.2, is computed from

$$T = (\ln 2)/K. \quad (3.1)$$

Table 3.1: Dimensionality  $\nu$  as a function of embedding dimension  $k$  for the analyzed data. All abbreviations are explained in Section 3.1. No saturation values ( $\nu_s$ ) were obtained for some of the data, and this is indicated in the Table by a horizontal line. The question mark after a value indicates that it is probably spurious.

location	variable	$\tau$ (day)	data	$k$							$\nu_s$	
				5	7	9	11	13	15	17		19
BOX 139	SST	5	daily	4.9	6.5	8.0	9.3	10.2	11.0	11.5	12.3	—
			winter	4.6	6.3	7.7	8.1	8.8	9.5	10.0	10.7	—
			summer	4.9	6.5	8.4	9.2	10.6	11.8	10.9	11.3	—
BOX 139	SSP	5	daily	4.9	6.7	8.0	9.1	9.4	9.5	9.6	9.7	9.6?
			winter	4.9	6.3	7.4	8.2	8.7	8.9	9.0	9.0	9.0?
			summer	4.9	6.4	7.7	8.6	8.9	8.9	8.8	9.0	8.9?
BOX 244	SST	5	daily	4.8	6.6	8.7	10.4	11.7	12.7	13.0	13.5	—
			winter	4.7	6.3	7.5	9.0	10.1	11.4	12.6	14.3	—
			summer	4.7	6.4	8.0	9.9	10.8	11.4	12.1	12.4	—
BOX 244	SSP	7	daily	4.8	6.5	8.3	9.2	9.5	10.2	10.2	10.0	10.1?
			winter	4.8	6.8	7.4	8.1	8.6	8.4	8.5	8.3	8.5?
			summer	4.8	6.5	7.7	8.8	9.5	10.0	10.0	9.9	10.0?
FCL	ST	3	daily	4.8	6.7	8.1	9.7	11.1	11.7	13.1	13.8	—
			winter	5.0	6.8	8.2	9.8	11.5	12.5	12.2	12.7	—
			summer	4.8	6.5	8.5	9.7	10.4	11.6	12.3	13.4	—
FCL	SP	2	daily	5.0	6.8	8.5	10.2	11.3	12.0	13.7	14.0	—
			winter	5.0	6.7	8.3	9.8	11.6	13.2	13.6	14.6	—
			summer	4.7	6.7	8.3	9.7	10.4	11.6	12.9	13.9	—
LA	ST	4	daily	4.8	6.5	7.8	8.8	9.3	10.2	10.2	10.3	10.3?
			winter	4.8	6.7	7.6	8.8	9.5	10.3	10.3	10.3	10.3?
			summer	4.8	6.4	7.4	8.5	9.5	9.9	9.9	9.8	9.9?

Since saturated fractal dimensions are not actually reached, Eq. (2.9) should not be used, and the error-doubling times in Table 3.2 are unreliable. For example, although the potential predictability is larger in BOX 244 than in BOX 139 (Madden, 1976), the error-doubling times for both regions are similar in Table 3.2. Also, for the Lorenz system (Lorenz, 1963), or other known systems, our computations show that the values of  $K$  and  $T$  are not sensitive to the time delay  $\tau$ ; whereas, the values of  $K$  and  $T$  in Table 3.2 vary significantly when the time delay  $\tau$  is increased. For example, in contrast to the values in Table 3.2 (with  $\tau$  as given in Table 3.1),  $T$  is 14.6 days for BOX 244 SSP with  $\tau = 10$  days,  $T$  is 8.3 days for BOX 139 SSP with  $\tau = 8$  days, and  $T = 6.3$  days for LA ST with  $\tau = 6$  days. Since saturated fractal dimensions were not reached in previous studies, such estimates of the error-doubling time based on Eqs. (2.9) and (3.1) are also unreliable (e.g., in Fraedrich, 1987).

Although the number of observations in our data set at each location is comparable with or more than those used in previous studies, we still cannot obtain low-dimensional attractors from these data. However, low-dimensional attractors are claimed in previous studies. The existence of low-dimensional atmospheric attractors is currently a highly debated subject. The qualitative and quantitative limitations to the Grassberger-Procaccia algorithm have been discussed in Sec. 2.2, and it is mentioned that the quantitative requirement of Ruelle (1990); i.e., at least  $M = 10^{\nu_s/2}$  data points are necessary to reliably estimate fractal dimension  $\nu_s$ , is the least strict one among different criteria. With this in mind, Ruelle (1990) has shown that the estimate of  $\nu_s = 7.3$  in Tsonis and Elsner (1988) is spurious. Using the same argument, we can show that the estimate of  $\nu_s = 7.0$  in Fraedrich (1987) is also an artifact of the short time series (only 1680 daily data of the surface pressure for 14 winter seasons at Berlin) and thus is unreliable. (By the way, Fraedrich (1986) did mention that 5475 daily data for 15 years only lead to unsaturated fractal dimensions) The estimate of a fractal dimension of about 8.0 in Keppenne and Nicolis (1989) is also unreliable, because only about 9000 daily 500 mb geopotential records were used for each station over western Europe. Although the data in Essex *et al.* (1987) and Sharifi *et al.* (1990) satisfy the requirement of Ruelle (1990), their estimates of low-dimensional attractors are still not so reliable according to the estimate of

Nerenberg and Essex (1990) with the condition that the critical embedding dimension  $k_c$  be greater than the fractal dimension  $\nu_s$ . The requirement that  $k_c > \nu_s$  seems necessary in order to guarantee the saturation of the fractal dimension. A dimension of about 8.0 is also obtained in Keppenne and Nicolis (1989) using 63000 records ( $9000 \times 7$  stations). However, since the time series at the seven stations may describe the same attractor (as demonstrated by them), and since these time series describe the evolution of the attractor during the same period, 63000 data ( $9000 \times 7$  stations) may contain less information compared with 63000 data observed at a single station. Even if 63000 data is utilized, this number is still only marginally satisfied with the quantitative requirement of Nerenberg and Essex (1990).

By mentioning these examples (more can easily be found in the recent literature), we illustrate that most, if not all, of the previous estimates of low-dimensional attractors in the atmosphere are unreliable. However, Tsonis *et al.* (1991) recently relaxed the requirement  $k_c > \nu_s$ , using  $k_c = \nu_s$  instead, and claimed that the existence of low-dimensional attractors in weather and climate should not be disregarded based on the analysis of Nerenberg and Essex (1990). Finally, based on simple models, Lorenz (1991) recently proposed that, if a low fractal dimension can be obtained from observational data, this may instead reflect only the weak nonlinear interaction between the observed variable and the other variables in the atmosphere, and not the true dimensionality of the atmosphere.

Only single-point time series are used in our study and in most previous publications. In contrast, Pierrehumbert (1990) used the entire data sets of the monthly-average heights of the 500 mb surface covering the Northern Hemisphere poleward of  $30^\circ N$  latitude, and showed that these data sets are also insufficient to draw firm conclusions about the dimensionality of the global atmosphere, and that no low-dimensional ( $< 20$ ) global attractors exist.

The global attractor is probably multifractal (Halsey *et al.*, 1986). This means that the globally-averaged dimension will be dominated by the larger local dimensions; many local dimensions may be smaller than the global dimension, and the dimension may vary with location. Corresponding to this, the unsaturated dimensions  $\nu(k)$  in Table 3.1 vary

qualitatively with location. The geographic variability of fractal dimensions may also be related to the climatic signal-to-noise ratio. For instance,  $\nu(k)$  for the surface temperature in Los Angeles is lower than in Fort Collins where the climatic signal-to-noise ratio is smaller (Madden and Shea, 1978). On the other hand, the climatic signal-to-noise ratio in BOX 244 is higher than that in BOX 139 (cf. Fig. 6 in Madden, 1976), but the values of  $\nu(k)$  for the sea surface pressure in both regions are similar. However, these speculations about the geographical variability of fractal dimensions need further verification, since no saturated fractal dimensions can be obtained with confidence in Table 3.1. Similarly, although the correlation dimension of daily data appears to be larger than those of winter and summer data in Table 3.1, due to the fact that the (total) daily data include the transition-season (spring and fall) data as well, this also needs further verification.

In summary, we have shown in this section that most, if not all, of the previous estimates of low-dimensional attractors in the atmosphere are unreliable. Using longer time series of observational data, we still cannot obtain a saturated fractal dimension  $\nu_s$ , and we can claim only that  $\nu_s$  is well above 8. Because saturated values cannot be reached, the computation of the Kolmogorov-Sinai entropy and the error-doubling time based on Eqs. (2.9) and (3.1) is unreliable. We have also shown that our data are neither white noise nor colored noise. The geographic variability of fractals is qualitatively discussed in relation to the global multifractal assumption and the climatic signal-to-noise ratio.

### 3.3 Lyapunov Exponents and Predictability of the Atmosphere

We have shown in the previous section that no saturated fractal dimensions can be reached and predictability cannot be estimated reliably. Though some people may question the usefulness of computing fractal dimensions for the atmosphere, nobody questions the importance of predictability. Therefore, in this section, we evaluate the Kolmogorov-Sinai entropy and the error-doubling time in the atmosphere by estimating the Lyapunov-exponent spectrum from our practical and reliable method discussed in Sec. 2.3.

Noise is an infinite-dimensional process and tends to decrease the density of data points defining the attractor as the embedding dimension  $k$  increases (Wolf *et al.*, 1985).

Because of the limitations due to the noise level and the total number of data points, we believe that the results with  $k \leq 5$  are more reliable than those with  $k > 5$ . Since our goal is to obtain with confidence as many Lyapunov exponents as possible, we report our results for  $k = 5$  only. As shown in Sec.2.3, at least the positive Lyapunov exponents can be computed reliably for  $k = 5$ . (In our computations, we also find that, as  $k$  increases beyond 5, the Lyapunov exponents decrease slowly, but the Kolmogorov-Sinai entropy and the error-doubling time change very little.)

Table 3.3 summarizes the Lyapunov-exponent spectrum for each analyzed data set. It is seen that at least two Lyapunov exponents are positive with comparable magnitude. Furthermore, at least one exponent must be zero, and we can easily identify this exponent as  $\lambda_3$  in each case (since  $\lambda_3$  is zero to within the error bars). Therefore, the atmosphere has a hyperchaotic attractor with a folded, multidimensional fractal structure, and unstable motion of comparable importance occurs along two directions. We then obtain the Kolmogorov-Sinai entropy  $K$ , as the sum of the two positive Lyapunov exponents, and the error-doubling time  $T$  for each data set. We can conclude from Table 3.3 that the predictability time  $T$  is about 5 to 8 days at BOX 139 and BOX 244, about 4 to 5 days in Los Angeles, and about 2 to 3 days in Fort Collins. It is also seen from Table 3.3 that the predictability time  $T$  is shorter for the daily data than for the summer and/or winter data, since the daily data includes not only summer and winter data, but also transition-season (spring and fall) data. Besides, it is found that the predictability time  $T$  is larger in summer than in winter for all variables. Possible reasons for this result are that weather events of short life time (such as summer thunderstorms) are filtered out in daily average data used in this study, and there are more propagating weather systems in winter than in summer.

Local predictability is controlled by large-scale advection processes and local forcing. Due to the regulation on the weather and climate in Los Angeles by the eastern portion of the subtropical ridge associated with the descending portion of the Hadley cell, and the much more frequent influence of the polar front on the weather and climate in Fort Collins, the potential climatic predictability which is a sort of climatic signal-to-noise

Table 3.2: Kolmogorov-Sinai entropy  $K$  and error-doubling time  $T$  of the sea surface pressure (SSP) at BOX 139 and BOX 244 and of the surface temperature (ST) at Los Angeles (LA).

Location		BOX 244	BOX 139	LA
variable		SSP	SSP	ST
K(day <sup>-1</sup> )	daily	0.095	0.093	0.173
	winter	0.061	0.079	0.159
	summer	0.084	0.068	0.155
T(day)	daily	7.3	7.5	4.0
	winter	11.4	8.8	4.4
	summer	8.3	10.2	4.5

Table 3.3: Lyapunov-exponent spectrum with the parameters given in the text. The error-doubling time  $T$  is computed from Eq. (3.1), where the Kolmogorov-Sinai entropy  $K$  is obtained by summing the first two Lyapunov exponents.

location	variable	daily data number	data	Lyapunov exponent (day <sup>-1</sup> )					$T$ (day)
BOX 139	SST	13,870	daily	0.063	0.031	-0.006	-0.052	-0.134	7.4
			winter	0.064	0.026	-0.005	-0.047	-0.131	7.7
			summer	0.064	0.019	-0.011	-0.059	-0.142	8.4
BOX 139	SSP	13,855	daily	0.098	0.044	0.004	-0.047	-0.133	4.9
			winter	0.117	0.055	0.021	-0.048	-0.142	4.0
			summer	0.075	0.037	-0.000	-0.042	-0.136	6.2
BOX 244	SST	13,860	daily	0.102	0.046	0.001	-0.042	-0.132	4.7
			winter	0.086	0.040	0.006	-0.048	-0.130	5.5
			summer	0.078	0.030	-0.007	-0.043	-0.138	6.4
BOX 244	SSP	13,877	daily	0.068	0.033	0.003	-0.031	-0.089	6.9
			winter	0.078	0.034	0.006	-0.028	-0.098	6.2
			summer	0.060	0.028	-0.002	-0.033	-0.096	7.9
FCL	ST	36,555	daily	0.195	0.081	0.016	-0.077	-0.220	2.5
			winter	0.191	0.089	0.011	-0.063	-0.228	2.5
			summer	0.144	0.058	-0.010	-0.068	-0.228	3.4
FCL	SP	32,870	daily	0.283	0.119	0.022	-0.089	-0.348	1.7
			winter	0.238	0.089	-0.000	-0.108	-0.340	2.2
			summer	0.215	0.105	0.000	-0.122	-0.325	2.2
LA	ST	14,245	daily	0.121	0.065	0.004	-0.059	-0.174	3.7
			winter	0.122	0.053	-0.001	-0.058	-0.169	4.0
			summer	0.101	0.046	-0.002	-0.052	-0.162	4.7

ratio, is higher in Los Angeles than in Fort Collins (see, e.g., Madden and Shea, 1978). Corresponding to this, as shown in Table 3.3, the predictability time  $T$  is larger for surface temperature in Los Angeles than in Fort Collins.  $T$  is also larger for sea surface pressure in BOX 244 than in BOX 139, where the climatic signal-to-noise ratio is also smaller and the potential predictability is shorter (Madden, 1976).

Our estimates of the error-doubling time in Table 3.3 are from about 2 to 8 days for various locations. However, twin experiments of General Circulation Models (GCMs) by Smagorinsky (1969) give an error-doubling time of about 2.5 days for the vertically integrated standard deviation of the temperature in the Northern Hemisphere. Using an ECMWF GCM, Lorenz (1982) obtained an error-doubling time of about 2 days for small initial errors of 500 mb heights in the Northern Hemisphere with the aid of a quadratic hypothesis for the nonlinear terms in the equation governing the growth of errors. The difference between their estimates and our estimates may be explained as follows. First, we use single-point time series and study local predictability, but they used data for the entire Northern Hemisphere and studied the global predictability, which is controlled by areas of lower local predictability (i.e., higher Kolmogorov-Sinai entropy). Therefore, it is natural that our estimates of the error-doubling time are approximately equal to or greater than their estimates. Second, the error-doubling time depends on the magnitude of initial errors: this time is short for small initial errors and long for larger initial errors (cf. Fig. 2.1). Because our data is from observations, our estimates of error-doubling time are generally larger (and more physically relevant) than those based on truly small initial errors. Third, daily-averaged data are used in this study, but instantaneous values were used in their studies. The averaging process smooths data and increases the error-doubling time. Fourth, we use observational data, but they used model-generated data and it is not clear that the error-doubling time in the GCMs is the same as in the real atmosphere. Finally, we use surface observations, but they used results above ground. The last two points will cause differences between our estimates of error-doubling time and theirs, but do not necessarily increase the error-doubling time in our estimates. Using the 500 mb geopotential record over western Europe, Keppenne and Nicolis (1989) obtained

a error-doubling time of about 19 days. This discrepancy with our estimates may also be explained by the second and last points in the above discussion. In other words, we use surface temperature and pressure data but they used 500 mb geopotential record, and, because of this, the magnitude of initial errors may also be different.

Traditional predictability studies (e.g., Lorenz, 1982) by means of numerical models in atmospheric science usually study the error growth from a reference state disturbed by various methods of perturbation (ECMWF Workshop, 1988). Both the traditional approach and the analysis presented in this paper share a common conclusion: when the initial error is small, its growth rate depends on the dynamics of the system, rather than on the initial error itself. On the other hand, traditional predictability studies provide only the largest (positive) Lyapunov exponent; whereas, our analysis provides all of the positive exponents, which allows a more appropriate quantitative measure of predictability, since different positive Lyapunov exponents correspond to the divergence of initial errors in different directions. The traditional approach uses entire global fields of data; in contrast, we only use single-point time series. We do not expect to extract all of the information about the global dynamics, but we do expect to gain an insight concerning predictability from local time-series analyses. As recommended by the ECMWF Workshop (1988, p.17), the evaluation of the dimensionality of atmospheric attractors may have an impact on the number of elements needed in a Monte Carlo ensemble forecast of the extended range. We also anticipate that the analysis of predictability will aid the selection of initial states for the Monte Carlo ensemble extended-range forecast.

Finally, we discuss a problem which needs further study using more data. For known systems (e.g., the Lorenz equations), we found that the computation of the Lyapunov-exponent spectrum is insensitive to the selection of  $\tau$ , which is approximately the e-folding time of the autocorrelation function. For Gaussian white noise, our computations show that Lyapunov exponents are inversely proportional to  $\tau$ . However, when we analyze our data, we find that the Lyapunov exponents decrease slightly as  $\tau$  increases, although they are not inversely proportional to  $\tau$ , as would be the case for Gaussian white noise. This may be due to the high fractal dimension of the atmosphere. This uncertainty could

increase the estimates of  $T$  by as much as 50%. Much more data may be required so that the Lyapunov-exponent spectrum can be evaluated for higher embedding dimensions to improve the estimates of the predictability time  $T$ .

Since the noise level in our data may be assumed to be typical for daily data of the atmosphere, and since the total number of data points (from about 13,800 to about 36,500) is larger than those used in previous studies (e.g., about 5500 in Fraedrich, 1986; about 9000 for each station in Keppenne and Nicolis, 1989), it is not unreasonable to assume that the above problem may be very common for similar studies using daily data of the atmosphere, and sensitivity studies should be conducted to determine its importance in estimating predictability.

In summary, by means of computing the Lyapunov exponents, we obtain error-doubling times varying from about 2 to 3 days in Fort Collins to about 4 to 5 days in Los Angeles and to about 5 to 8 days in BOX 139 (midlatitude North Atlantic) and BOX 244 (subtropical North Atlantic). These time scales are smaller than those inferred by Keppenne and Nicolis (1989) for western Europe, and are approximately equal to or larger than those obtained by Smagorinsky (1969) and Lorenz (1982) using GCMs. The reasons are discussed in detail. The predictability time in an area (e.g., Los Angeles) of high climatic signal-to-noise ratio is longer than that in an area (e.g., Fort Collins) where the climatic signal-to-noise ratio is small. The predictability time for daily data for the entire year is shorter than for summer and/or winter data, since the daily data includes not only summer and winter data, but also data for the transition seasons (spring and fall), whose predictability is poorer and whose dynamics are apparently controlled by more variables than in summer and winter. Finally, we have discussed the slight sensitivity of the calculation of the Lyapunov-exponent spectrum to the choice of the time delay  $\tau$ .

## Chapter 4

### CHAOS IN DAISYWORLD

In the previous chapter, we have discussed the application of chaos theory to the observational data analysis which goes beyond the traditional statistical or linear analyses. Another possible application of chaos is the inspiration of new ideas by the concept of chaos. In this chapter, we will explore chaos in daisyworld. More detailed discussions can be found in Zeng *et al.* (1990 and 1992c).

#### 4.1 Introduction

It is now widely accepted that the Earth is a single system which consists of the biota and their environment. These two elements of the system are closely coupled: the biota regulate the environment (e.g., climate on a planetary scale) and, in turn, the environment restricts the evolution of the biota and dictates what type of life can exist as a consequence of Darwinian natural selection. In order to qualitatively understand this very complex interaction mechanism, a model, daisyworld, which is an active system where the biota and the environment are tightly coupled, was first described by Lovelock (1982) and then used to study the interaction between daisies of one or two species and the temperature of the environment (Watson and Lovelock, 1983, hereafter denoted by WS in this chapter). These authors found that the inclusion of feedback from the environment, regardless of its direction, stabilized daisyworld, and this was consistent with the earlier Gaia hypothesis that the climate and the chemical composition on the Earth have been and are maintained at a steady state by the presence of life itself (Lovelock and Margulis, 1974). Later, Gaia is stated more scientifically as a theory in Lovelock (1989) that views the evolution of the biota and of their environment as a single, tightly coupled process, with the self-regulation of climate and chemistry as an emergent property. Among the many examples to show the

widespread influence of the Gaia theory (or hypothesis) are the 1988 Chapman Conference on Gaia of the American Geophysical Union and the scientific journal *Gaian Science* for geophysiology researchers and teachers.

Though the feedback in daisyworld is much simpler than that on the Earth, research on such an imaginary planet may provide insight into the properties of the Earth's climate. Therefore, further studies are needed. The purpose of this chapter is to study this fictional world in more detail, and, especially, to evaluate the chaotic properties of this model. Both qualitative and quantitative methods from modern chaos theory have been utilized to verify the presence of chaos in daisyworld.

## 4.2 Differential Model for Daisyworld

Daisyworld is a cloudless flat or cylindrical planet with negligible atmospheric greenhouse gases that bears life only in the form of different species of daisy. The behavior of the daisyworld governed by differential equations described in WS will be studied first. For completeness, these equations are written here except in a more general way. A more realistic model for daisyworld, the discrete model, will be discussed in the next section.

### 4.2.1 Differential model

The growth rate of the daisies is given by a set of equations in population ecology theory (Carter and Prince, 1981):

$$\frac{da_i}{dt} = a_i(x\beta_i - \gamma_i) \quad (i = 1, 2, \dots, m), \quad (4.1)$$

where  $a_i$  is the area covered by the  $i$ th species of daisy, which is measured as a fraction of the total surface area of daisyworld. The variable  $x$  is the unoccupied fertile area in which daisies could grow, i.e.,

$$x = p - \sum_{i=1}^m a_i, \quad (4.2)$$

where  $p$  is the total area of fertile ground.  $\gamma_i$  is the death rate per unit time and is taken to be the same constant for each species.  $\beta_i$  is the growth rate per unit time and per unit area, and it is assumed to be a parabolic function of the local temperature  $T_i$ :

$$\beta_i = C[1 - 0.003265(22.5 - T_i)^2] , \quad (4.3)$$

which is zero at  $T_i = 5^\circ\text{C}$  or  $40^\circ\text{C}$ , and reaches its maximum value of  $C$  (where  $C$  is a constant) at  $T_i = 22.5^\circ\text{C}$ . WS restricted their attention to  $C = 1$ ; in this chapter, we consider the range  $1 \leq C \leq 4$ .

The effective temperature  $T_e(^{\circ}\text{C})$  at which the planet's surface radiates can be obtained by the radiation budget equation on the surface:

$$\sigma(T_e + 273)^4 = SL(1 - A) , \quad (4.4)$$

where  $\sigma$  is Stefan's constant,  $S$  is a constant having units of energy flux,  $L$  is a dimensionless measure of the luminosity of the sun of daisyworld, and  $A$  is the average albedo of the planet, which is given by

$$A = (1 - p)A_{gs} + xA_{gf} + \sum_{i=1}^m a_i A_i , \quad (4.5)$$

where  $A_{gs}$  is the albedo of the sterile area in which the daisies cannot grow,  $A_{gf}$  the albedo of the unoccupied fertile area, and  $A_i$  the albedo of the  $i$ th species.

The local temperature of different types of surface can be determined using a conservation of energy balance for the planet. For the daisies, it can be expressed as

$$(T_i + 273)^4 = q(A - A_i) + (T_e + 273)^4 , \quad (4.6)$$

where  $q$  is the conduction coefficient of solar energy among different types of surface. Equation (4.6) can be simplified with small error for the temperatures of interest:

$$T_i = q'(A - A_i) + T_e , \quad (4.7)$$

where  $q' = 0.25 q / (295.5)^3$ . Alternatively, for the particular value  $q = SL/\sigma$ , Eq. (4.6) can be rewritten by means of Eq. (4.4):

$$(T_i + 273)^4 = q(1 - A_i) , \quad (4.8)$$

which means that the local temperatures are determined solely by the local radiation balance; i.e., there is no feedback between the daisies and their environment.

Equations (4.1)–(4.5) and (4.7) [or (4.8)] constitute a closed set of equations. The differential equation (4.1) can be solved by a forward-difference scheme with small  $\Delta t$ :

$$a_i^{n+1} = a_i^n + \Delta t a_i^n (x^n \beta_i^n - \gamma_i^n) \quad , \quad (4.9)$$

where  $\Delta t$  is the time step and implies, in physical terms, that there is a time delay in the interaction between the daisy population and the local temperatures.

#### 4.2.2 Steady-state behavior of the system

As in WS, it is assumed in this subsection, unless explicitly stated otherwise, that  $p = 1$  (i.e., the planet's surface is totally fertile),  $S$  [in Eq. (4.4)] =  $9.17 \times 10^5$  ergs  $\text{cm}^{-2} \text{s}^{-1}$  (or  $917 \text{ Wm}^{-2}$ ), the albedo  $A_{gf}$  [in Eq. (4.5)] =  $0.5$ ,  $q' = 20$ ,  $\gamma_i$  is constant,  $\Delta t = 0.01$ , and  $C = 1$ .

Just as the Sun has been increasing in solar luminosity since the formation of the Solar System (Owen *et al.*, 1979), the luminosity of the sun of daisyworld is assumed to rise slowly, so that, at each value of  $L$ , the possible steady state of daisyworld is evaluated by solving the governing equations forward in time with the initial values of different daisies set at the previous steady-state values, or 0.01 if these are zero.

Fig. 4.1 shows the steady-state behavior of four species of daisy and the temperature  $T_e$  as the luminosity  $L$  is incremented. The effective temperatures for one to three species are also included in Fig. 4.1 for comparison. It is seen from Fig. 4.1a that the area occupied by daisies is almost constant, i.e.,  $\sum_{i=1}^4 a_i \approx 0.7$ , within the range of  $L$  from 0.7 to 1.7; however, as the luminosity increases, the species with lower albedos become extinct in the battle for survival of the fittest, and the species with the higher albedo dominates the planet. For each value of luminosity from 0.7 to 1.7, only one or two species exist. Though not shown here, with only two or three species, daisyworld exhibits the same characteristics. This is just one example that daisyworld can give insights on biodiversity, but further study using more species is needed.

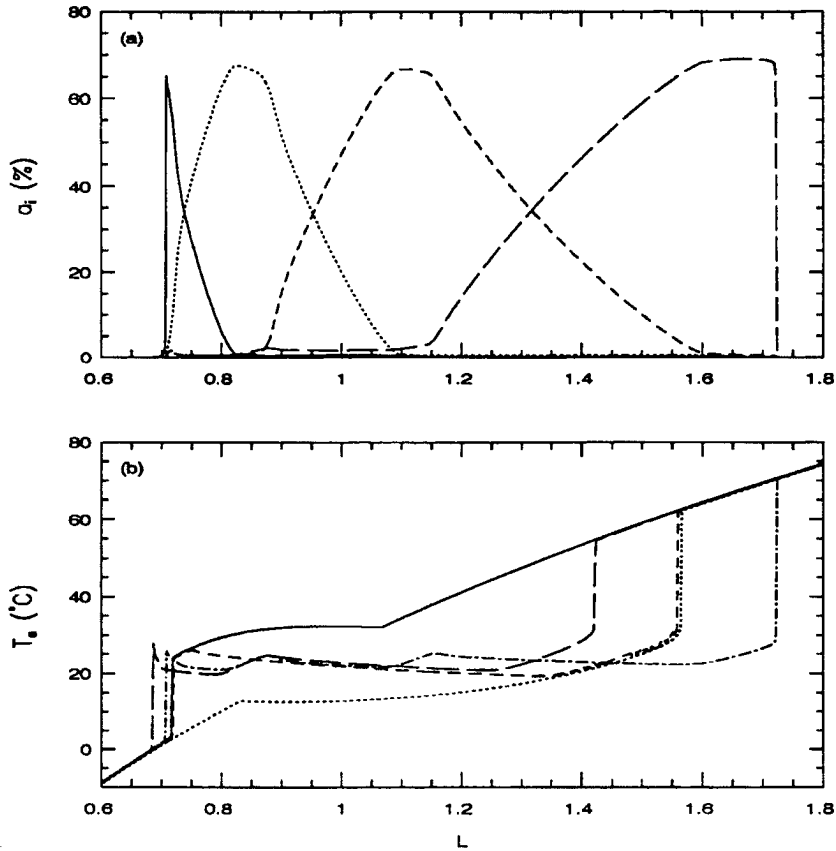


Figure 4.1: Steady-state behavior of daisyworld. (a) Areas of four species where  $A_1$ ,  $A_2$ ,  $A_3$ , and  $A_4$  are 0.2, 0.4, 0.6, and 0.8, denoted by solid, dotted, short-dashed, and long-dashed curves, respectively. (b) effective temperatures for the cases of one to four species: solid and dotted curves denote the cases of one species with  $A_1 = 0.25$  and  $0.75$  respectively; short-dashed curve denotes the case of two species with  $A_1 = 0.25$  and  $A_2 = 0.75$ ; long-dashed curve denotes the case of three species with  $A_1$ ,  $A_2$ , and  $A_3$  being 0.1, 0.4, and 0.7; and dash-dotted curve denotes the case of four species with albedos as given in (a).

Once the non-zero steady state is reached for a value of luminosity, it can be seen from Eqs. (4.1) and (4.2) that

$$\sum_{i=1}^m a_i = p - \gamma_j / \beta_j , \quad (4.10)$$

where the subscript  $j$  can be any number among  $1, 2, \dots, m$  for which  $a_j \neq 0$ . This means that the area occupied by all daisies must be constant no matter how many different kinds of daisies exist. The results discussed in the previous paragraph are consistent with this general conclusion.

Fig. 4.1b shows that the temperature regulation of the planet is similar for two, three, or four species, and, therefore, for the remainder of this chapter, we will consider only one or two species for simplicity. One species, with  $A_1 = 0.25$ , will be referred to as “black”, and the other,  $A_2 = 0.75$ , will be referred to as “white” to emphasize the contrast, though neither of them is perfectly black or white. Hereafter, subscripts  $b$  and  $w$  will be used to indicate black and white daisies.

When Eq. (4.8) is used to compute  $T_i$ , instead of Eq. (4.7), i.e.,  $q = SL/\sigma$ , the steady-state behavior for two species is shown in Fig. 4.2. It is found that, for the range of  $L$  from 0.8 to 1.5, both black and white daisies are eliminated, and the temperature increases almost linearly. Computations also show that the daisyworld model for one or two species using Eq. (4.8) exhibits no hysteresis when the luminosity decreases; whereas, the system using Eq. (4.7) does (see Fig. 1c in WS). Therefore, unlike Eq. (4.7), Eq. (4.8) does not yield a self-regulating system. Figures. 4.1 and 4.2 also show that the inclusion of the feedback (Fig. 4.1) stabilizes the environment compared with the no-feedback case (Fig. 4.2).

Calculations also show that the steady-state behavior is the same for time steps  $\Delta t$  of 0.01, 0.5, or 1.0, although the time needed to obtain the steady state is different. Furthermore, it is found that, when steady-state behavior is reached, it is similar for different parameter values, e.g., changing  $q'$  from 20 to 40 or 60, or changing  $C$  in Eq. (4.3) from 1 to 2.

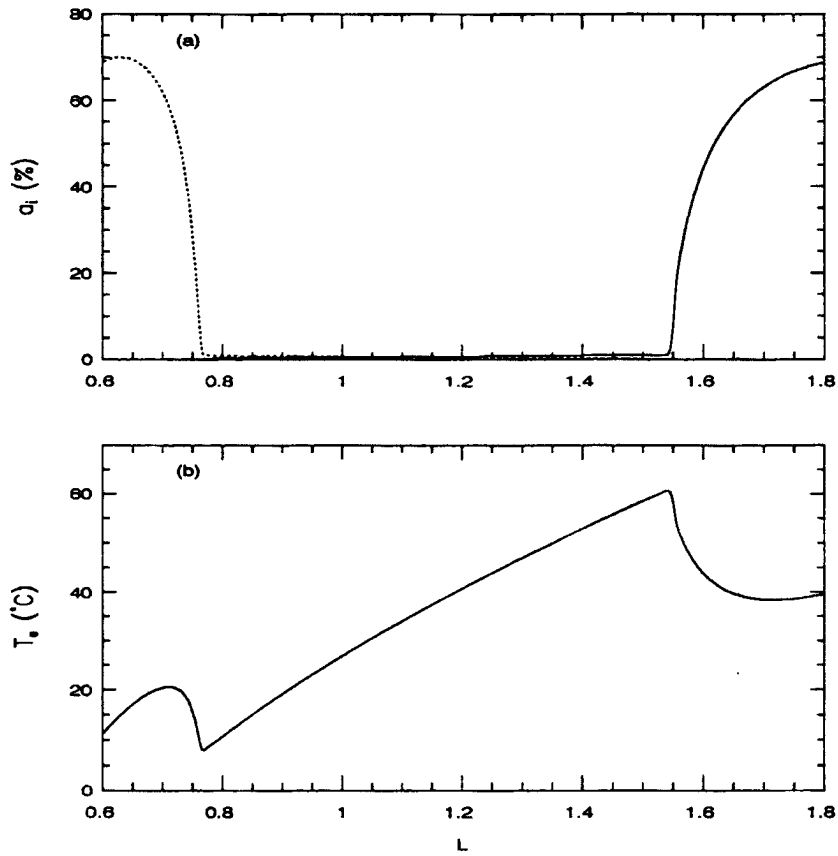


Figure 4.2: Steady-state responses of daisyworld with Eq. (4.8). (a) Areas of black and white daisies, denoted by dotted and solid curves, respectively; (b) effective temperature  $T_e$ .

Therefore, we have shown that, not only for one or two species (which have been discussed in WS), but also for more than two species, the inclusion of the feedback between the daisies and their environment stabilizes the daisyworld when the differential equation (4.1) is used. However, as will be argued in the next section, a more realistic model for daisyworld is a discrete model, rather than a differential model.

### 4.3 Discrete Model for Daisyworld

#### 4.3.1 Discrete model

As mentioned in Subsection 4.2.1, the time step  $\Delta t$  in Eq. (4.9) represents, in physical terms, the time delay in the interaction between the daisy population and the local temperatures. As a result, in order to accurately approximate the differential equation (4.1),  $\Delta t$  must be chosen to be small. However, this allows the daisies to adjust to temperature variations instantaneously (i.e., without delay), which is unphysical. A more realistic model is to let  $\Delta t$  be the generation time, since this is the characteristic response time of the daisy population. Therefore, we will modify the above model by replacing Eq. (4.1) by Eq. (4.9) with  $\Delta t = 1$  (i.e., with the generation time chosen as the unit of time):

$$a_i^{n+1} = a_i^n + a_i^n(x^n\beta_i^n - \gamma_i^n). \quad (4.11)$$

We will refer to the closed set of equations (4.2)-(4.5), (4.7) or (4.8), and (4.11) as the discrete model. We also refer to both the differential and discrete models as daisyworld, since we consider them to be two different models of the same physical system in which daisies interact strongly with their environment. For one species, this equation is the same as that considered by May (1974), and he has shown that the important parameter is  $(\beta - \gamma)$ , which he takes as high as 5. Hence, we consider the ranges  $0.3 \leq \gamma \leq 1$  and  $1 \leq C \leq 4$  (and, thus,  $\beta_i \leq 4$ ).

With regard to the question of whether the discrete model or the differential model is more appropriate, we refer to Carter and Prince (1981). While they do write down a differential equation, to which WL refer as the basis for their differential model, Carter and Prince (1981) also conduct an experiment and show that the experimental data actually

agree closely with the discrete equation similar to Eq. (4.11) above (see their Fig. 1). The main problems with the differential model are that it allows an instantaneous response to any change, and it does not allow extinction to occur in a finite time. In contrast, the discrete model avoids both of these drawbacks. Furthermore, the discrete model with a finite generation time is a first step toward including seasonal variation, since it synchronizes the birth at the beginning of each new generation, which corresponds to the beginning of the growing season, rather than allowing continuous birth throughout the year.

In order to discuss the coupling constant  $C$  in Eq. (4.3) and the generation time  $\Delta t$ , we rewrite Eq. (4.9) as

$$\begin{aligned} a_i^{n+1} &= a_i^n + a_i^n(x^n\beta_i^n - \gamma_i^n) \Delta t \\ &= a_i^n + a_i^n[x^n(\beta_i^n/\lambda) - (\gamma_i^n/\lambda)] (\lambda\Delta t), \end{aligned} \tag{4.12}$$

which shows that changing  $\Delta t$  is equivalent to changing both the growth rate  $\beta_i$  and the death rate  $\gamma_i$ . This simply illustrates that the numerical values of these rates depend on the unit of time chosen for  $\Delta t$ . Physically, the generation time is nearly fixed (and chosen as the unit of time; i.e., time is measured in generations, leading to Eq. (4.11) above): unlike the growth rate, it changes only slightly as the climate changes. We will investigate the effect of varying the growth rate  $\beta_i$  by varying its coupling to the local temperature (as given by the coupling constant  $C$ ). Note that one can mathematically vary  $\Delta t$  as well, but this is not physically meaningful, since the generation time  $\Delta t$  is not physically variable.

It should be emphasized that the discrete model will yield different results from the differential model. It is known from basic chaos theory, even without any computations, that, for differential daisyworld, chaos can never occur in the one- and two-species cases. This is verified in WL and in Section 4.2. It is further shown in Section 4.2 that steady-state behavior is obtained in differential daisyworld with more than two species for a wide range of parameters. In contrast, for discrete Daisyworld, it will be shown later that periodic and even chaotic oscillations can occur in the one- and two-species cases. First, however, an analytic analysis is presented.

### 4.3.2 Theoretical analysis of the chaotic regime in the daisyworld model

When Eq. (4.8) is used in the model, constant luminosity leads to constant  $T_i$  in Eq. (4.8) and, hence, constant  $\beta_i$  from Eq. (4.3). The difference equation (4.11) with the above constants can be written as

$$a_i^{n+1} = (1 + \beta_i - \gamma_i)a_i^n - \beta_i a_i^n \sum_{j=1}^m a_j^n \quad (i = 1, 2, \dots, m) \quad , \quad (4.13)$$

where  $\beta_i$  and  $\gamma_i$  are constants.

For one species, we let

$$y = \frac{\beta}{1 + \beta - \gamma} a \quad , \quad (4.14)$$

so that Eq. (4.13) may be rewritten as

$$y^{n+1} = (1 + \beta - \gamma) y^n (1 - y^n) \quad , \quad (4.15)$$

which is the well known logistic difference equation (see, e.g., May, 1976, among others).

The solution  $y^{n+1}$  of this equation is chaotic for many values of  $1 + \beta - \gamma$  in the range

$$3.57 \leq 1 + \beta - \gamma \leq 4 \quad . \quad (4.16)$$

On the other hand, the physical restriction on  $a$  is  $0 \leq a \leq 1$ , and the maximum value of  $y$  in Eq. (4.15) can be easily obtained as  $(1 + \beta - \gamma)/4$ . Therefore, Eq. (4.14) yields the condition

$$(1 - \sqrt{\gamma})^2 \leq \beta \leq (1 + \sqrt{\gamma})^2 \quad . \quad (4.17)$$

Combining this with Eq. (4.16) yields

$$\max \left[ (1 - \sqrt{\gamma})^2, (2.57 + \gamma) \right] \leq \beta \leq \min \left[ (3 + \gamma), (1 + \sqrt{\gamma})^2 \right] \quad , \quad (4.18)$$

and, for  $\gamma \leq 1$ , this becomes

$$2.57 + \gamma \leq \beta \leq (1 + \sqrt{\gamma})^2 , \quad (4.19)$$

which also implies that

$$0.616 \leq \gamma \leq 1 . \quad (4.20)$$

For more than one species, with  $\gamma_i = \gamma$  (i.e., the same for each species), we let

$$a = \sum_{i=1}^m a_i, \quad \beta = \frac{1}{a} \sum_{i=1}^m \beta_i a_i, \quad Y = \frac{\beta}{1 + \beta - \gamma} a , \quad (4.21)$$

and we sum Eq. (4.13) over  $i$  to yield

$$Y^{n+1} = (1 + \beta - \gamma) Y^n (1 - Y^n) , \quad (4.22)$$

which is the same as Eq. (4.15). However, while Eq. (4.22) indicates that chaos should again be expected, the specific results for the case with one species are not applicable, since  $\beta$  now depends on  $n$ . If, instead of Eq. (4.8), we use the more realistic Eq. (4.7), then  $\beta_i$  is no longer independent of  $n$ . However, the analysis leading to Eqs. (4.15) and (4.22) is still valid, with  $\beta$  now dependent on  $n$  in both cases. Therefore, chaos is again expected to occur, although we can give no quantitative prediction of the parameter regime. In the numerical results which follow, we use Eq. (4.7), rather than Eq. (4.8), since only the former can lead to self-regulation (cf. Figs. 4.1b and 4.2b).

#### 4.4 Numerical Results on Chaos in Daisyworld

Computations in this section are based on Eqs. (4.2)-(4.5), (4.7), and (4.11). Besides those related parameters specified in Section 4.2, other parameters are taken as follows:  $\Delta t = 1.0$ ,  $A_b = 0.25$  for black daisies, and  $A_w = 0.75$  for white daisies.

During a stage when the luminosity is fixed with time in daisyworld, we alter the internal environment by increasing the interaction between the daisies and the environmental effective temperature  $T_e$ , and by increasing the death rate; i.e., the parameters  $C$  in Eq. (4.3) and  $\gamma_i$  in Eq. (4.11) are increased. Note that the discrete equation (4.11) is

valid only when  $a_i \geq 0$ . If  $a_i$  becomes zero, extinction has occurred, after which it remains zero. It is meaningless to continue using the discrete equations and allow  $a_i$  to become negative.

#### 4.4.1 Daisyworld with only black daisies.

Figures 4.3 and 4.4 show a chaotic state of the planet using Eq. (4.7) with only black daisies at  $L = 0.90$ ,  $C = 4.0$ , and different values of  $\gamma_b$ . Other parameters are as previously specified. The plots are generated by solving the governing equations with the initial value of  $a_b$  (the area covered by black daisies) set at the steady-state value in Subsection 4.2.2.

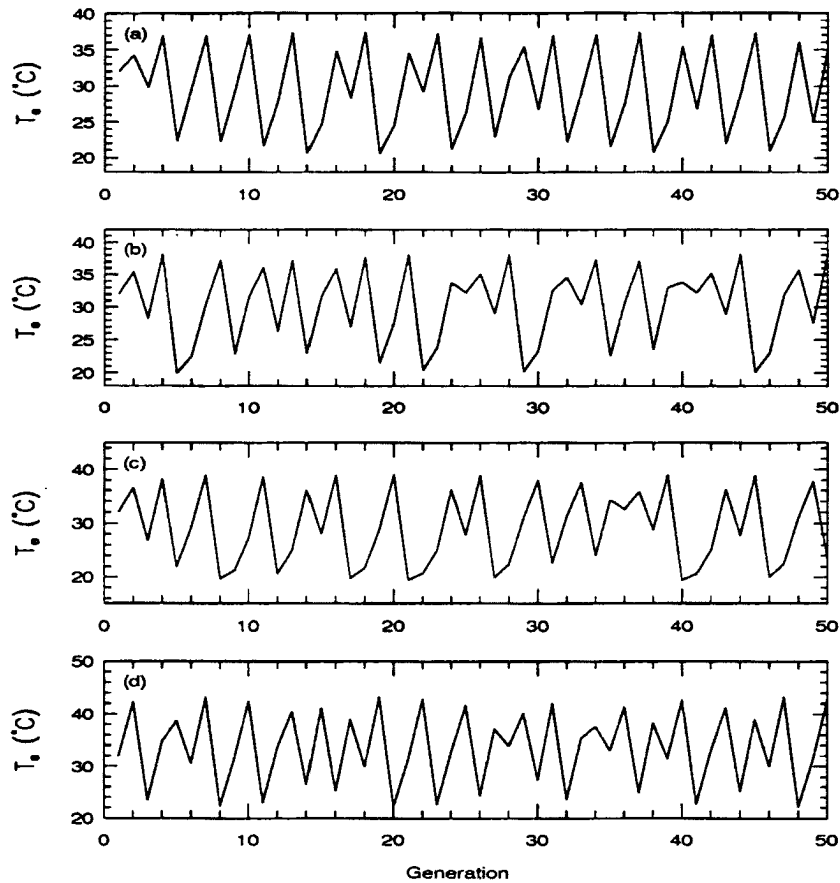


Figure 4.3: Chaotic behavior of the effective temperature  $T_e$  in daisyworld with only black daisies at  $L = 0.90$  and  $C = 4.0$ . (a)  $\gamma_b = 1.0$ ; (b)  $\gamma_b = 0.9$ ; (c)  $\gamma_b = 0.8$ ; (d)  $\gamma_b = 0.3$ .

It is obvious in these figures that black daisies alone can adjust to drastic change in the environmental temperature  $T_e$  (as large as  $19^\circ\text{C}$ ) without becoming extinct. However

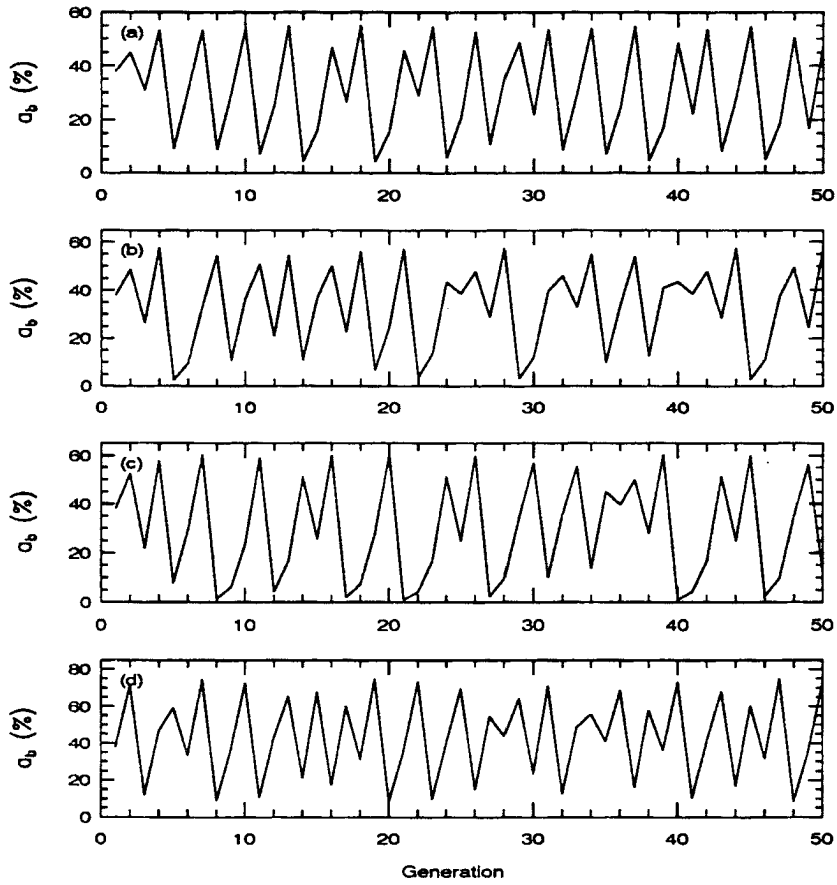


Figure 4.4: The same as in Fig. 4.3, except for the area  $a_b$  occupied by black daisies.

homeostasis is not maintained; instead, the effective temperature and the area covered by black daisies is chaotic and unpredictable. It is also interesting to note that variations of  $a_b$  and  $T_e$  in Figs. 4.3 and 4.4 are quite similar (cf., e.g., Fig. 4.3a and Fig. 4.4a). This feature is explained in the Appendix A.

According to Eqs. (4.19) and (4.20), no chaos occurs in the logistic difference equation when  $\gamma = 0.3$  and  $\beta = \text{constant}$ . However, using Eq. (4.7), in which case,  $\beta \neq \text{constant}$ , daisyworld is chaotic at  $\gamma_b = 0.3$ , which shows that the inclusion of the feedback from the environmental temperature widens the chaotic regime of daisyworld. This also illustrates the well known fact that, once the coefficient in the logistic map given by Eq. (4.15) becomes variable, it is difficult to analytically predict the occurrence of chaos from the equation.

The occurrence of chaos in the model is sensitive to the value of  $C$ , though not sensitive to the value of  $\gamma_b$  in this case. Figure 4.5 shows the results for  $C = 3.0$  and  $\gamma_b = 0.3$ . We see from Fig. 5 that both  $T_e$  and  $a_b$  are in stable cycles of period 2. The amplitude of the oscillation is  $10^\circ\text{C}$  for  $T_e$  and 32% for  $a_b$ . Both amplitudes are smaller than those for the chaotic states. When  $C = 3.0$  and  $\gamma_b = 0.8, 0.9$ , or  $1.0$ , periodic solutions are also obtained, and the amplitudes of  $a_b$  and  $T_e$  decrease with the increase of  $\gamma_b$ . At  $C = 2.0$ , the daisyworld model reaches a steady state for  $\gamma_b = 0.3, 0.8, 0.9$ , or  $1.0$ . Chaos occurs with  $C = 4.0$  for a wide range of values of the luminosity.

#### 4.4.2 Daisyworld with only white daisies.

The results with  $L = 0.92$  and  $C = 4.0$  are shown in Fig. 4.6. At  $\gamma_w = 1.0$ , the environmental temperature and the area occupied by white daisies appear to oscillate periodically with a period of 10. However, as will be shown later, they are, in fact, slightly chaotic. When  $\gamma_w$  is changed from 1.0 to 0.8, the apparent periodicity disappears and the chaos is apparent. The largest amplitudes of the variations of  $T_e$  and  $a_w$  are roughly  $7^\circ\text{C}$  and 18% for  $\gamma_w = 1.0$ , and roughly  $10^\circ\text{C}$  and 25% for  $\gamma_w = 0.8$ . It is also found that, at  $\gamma_w = 0.3$ , the white daisies become extinct by the fourth generation.

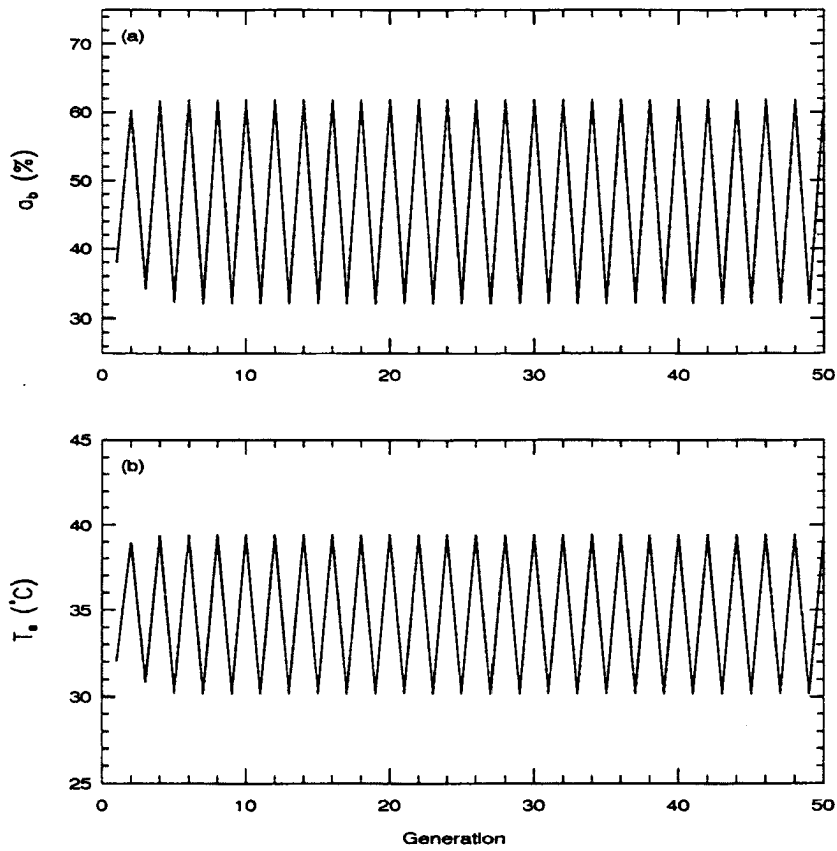


Figure 4.5: Values of  $a_b$  and  $T_e$  in the model with only black daisies at  $L = 0.90$  and  $C = 3.0$ , and  $\gamma_b = 0.3$ . (a)  $a_b$ ; (b)  $T_e$ .

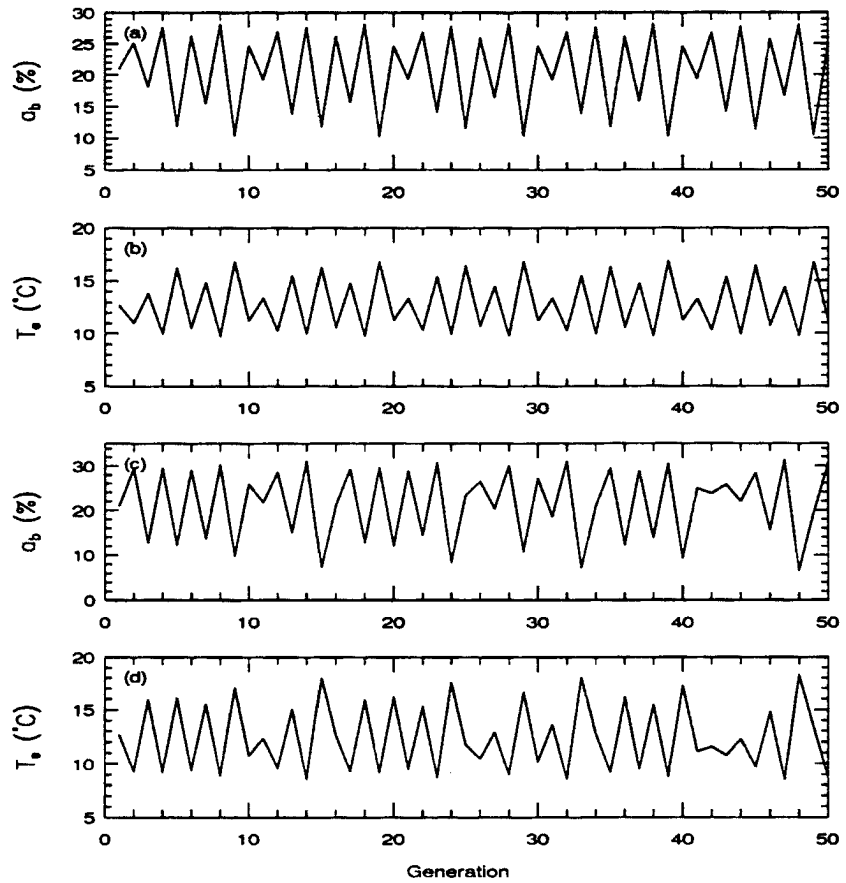


Figure 4.6: Chaotic behavior of  $a_w$  and  $T_e$  in daisyworld with only white daisies at  $L = 0.92$  and  $C = 4.0$ . (a)  $a_w$  with  $\gamma_w = 1.0$ ; (b)  $T_e$  with  $\gamma_w = 1.0$ ; (c)  $a_w$  with  $\gamma_w = 0.8$ ; (d)  $T_e$  with  $\gamma_w = 0.8$ .

In this case, the variations of  $a_w$  and  $T_e$  in Fig. 4.6 have opposite phase and are inverted versions of each other (cf. Figs. 4.6a and b; Figs. 4.6c and d), which is different than in case for only black daisies. Appendix A gives the explanation for this difference.

Computations with white daisies also show that  $T_e$  and  $a_w$  oscillate with period 2 at  $C = 3.0$ ,  $\gamma_w = 0.3$ , and are in a steady state at  $C = 3.0$ ,  $\gamma_w = 0.8, 0.9$ , or  $1.0$ , and at  $C = 2.0$ ,  $\gamma_w = 0.3, 0.8, 0.9$ , or  $1.0$ . Finally, for  $C = 4.0$ , the range of luminosities giving rise to chaos is smaller for white daisies than for black daisies. Unlike the case with only black daisies, the occurrence of chaos is sensitive to both  $C$  and  $\gamma_w$  in this case.

#### 4.4.3 Daisyworld with both black and white daisies.

Chaos occurs in daisyworld not only with one species, but also with two species. Figure 4.7 shows the chaotic state of the model for  $L = 0.80$  and  $C = 4.0$ . The largest amplitudes of variations of  $a_w$ ,  $a_b$ , and  $T_e$  are roughly 12%, 80%, and 23°C, respectively. At  $C = 3.0$ ,  $a_w$ ,  $a_b$ , and  $T_e$  in daisyworld vary in stable cycles of period 2 for  $\gamma_b = \gamma_w = 0.8, 0.9$ , or  $1.0$ . The periodic state for  $\gamma_b = \gamma_w = 0.8$  is shown in Fig. 4.8. It is seen that  $a_w$  and  $a_b$  increase or decrease at the same time and the trend in variation of both of them is opposite to that of  $T_e$ . The largest amplitudes of variations for  $a_w$ ,  $a_b$ , and  $T_e$  are roughly 4%, 24%, and 7°C, respectively. At  $C = 2.0$ , homeostasis is maintained in the model for  $\gamma_b = \gamma_w = 0.3, 0.8, 0.9$ , or  $1.0$ , just as with only one species. It is also found that variations of  $T_e$  and  $a_b$  have the same phase, but they have no phase relationship with  $a_w$  for the parameters used in Figs. 4.7 and 4.8 (cf. Figs. 4.7b and c; Figs. 4.8b and c). This is discussed in Appendix A.

The coupling strength  $C$  is the most important parameter in determining the qualitative behavior of daisyworld. As  $C$  is increased from 1.0 to 4.0, the behavior of daisyworld will change from a steady state to periodicity to chaos over a wide range of values of luminosity, and, thus, the system will become extremely sensitive to minor changes in the initial values of  $a_w$  and  $a_b$ . As a result, homeostasis can not be maintained by the presence of one or two species on the planet. Furthermore, since the chaos is more pronounced with two species than with one, there is no reason to believe that it will be eliminated by including additional species (also, recall Fig. 4.1, which showed that only one or two

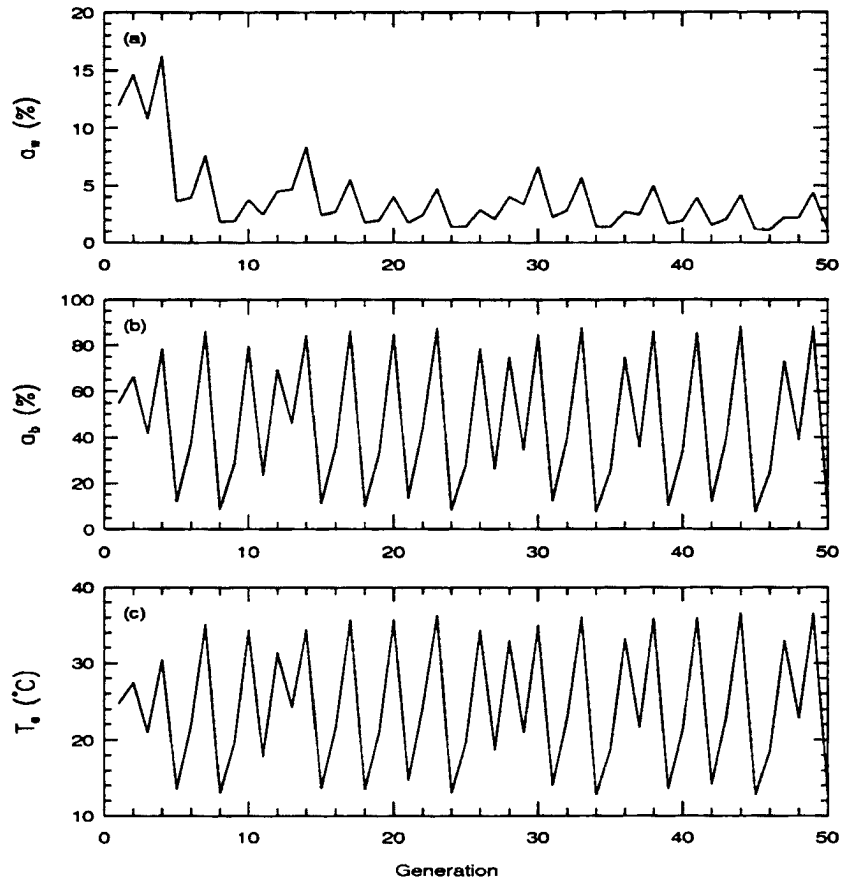


Figure 4.7: Chaotic behavior of  $a_w$ ,  $a_b$ , and  $T_e$  in daisyworld with black and white daisies at  $L = 0.80$ ,  $C = 4.0$ , and  $\gamma_w = \gamma_b = 1.0$ . (a)  $a_w$ ; (b)  $a_b$ ; (c)  $T_e$ .

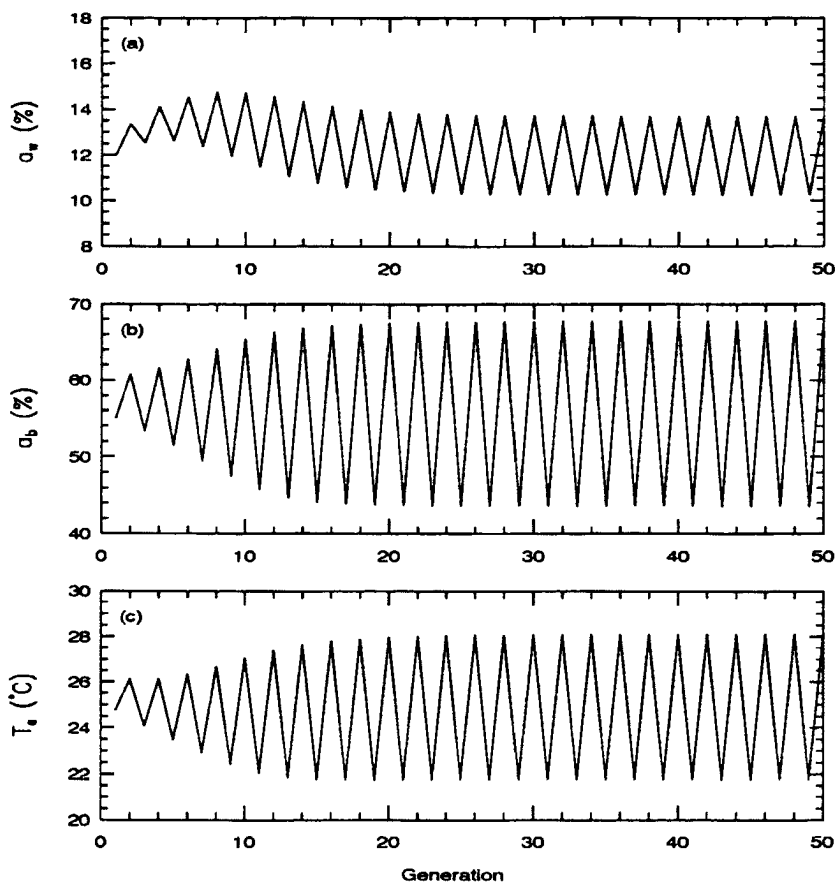


Figure 4.8: Periodic behavior of daisyworld with two species at  $L = 0.80$ ,  $C = 3.0$ , and  $\gamma_b = \gamma_w = 0.8$ . (a)  $a_w$ ; (b)  $a_b$ ; (c)  $T_e$ .

species at a time were involved in maintaining the steady-state behavior). Therefore, the conclusion of Watson and Lovelock (1983), based on the differential equation (4.1), that daisyworld always shows greater stability with daisies present, is not a general result, and the remarks made by Lovelock (1986) that the inclusion of feedback from the environment appears to stabilize the system is also not true in general.

#### 4.4.4 Verification of chaos in daisyworld

The existence of chaos in daisyworld is verified by examining power spectrum and computing fractal dimensions and Lyapunov exponents. When the power spectra are computed for the cases discussed in the previous subsections, broadband noise is found for the chaotic behavior in Figs. 4.3, 4.4, 4.6, and 4.7, and sharp peaks for the periodic behavior in Figs. 4.5 and 4.8. Some examples are shown in Fig. 4.9. In particular, for daisyworld with only white species and  $\gamma_w = 1.0$ , the power spectra shows unambiguously that the behavior is slightly chaotic (note the low noise level), even though this is not apparent from Figs. 4.6a and b.

The fractal dimensions are computed from Eqs. (2.5)-(2.7). The Lyapunov exponents are computed from Bennetin *et al.* (1976), which is based on Eqs. (2.12)-(2.13), since the governing equations are known. Of course, the more complex algorithm based on Eqs. (2.14)-(2.22) will yield the same results. The correlation dimensions and Lyapunov exponents for some cases of chaos discussed in the previous three subsections are given in Table 4.1. Note that there is only one exponent for the case of only one species. It is seen that, in each case, the correlation dimension is fractional and the exponent  $\lambda_1$  is positive, which shows unambiguously that chaos is present.

In summary, by analyzing the power spectra, fractal dimensions, and Lyapunov exponents, we have verified the existence of chaos in daisyworld with one or two species.

#### 4.5 Conclusions

The simple daisyworld model has been used to study the interaction between biota and their environment. When the differential equation (4.1) is used, it is shown that steady-state behavior is always reached, not only for one or two species (as in WS), but also for



more than two species. However, it is argued that a more appropriate model for daisyworld is the discrete model [Eq. (4.11)] rather than the differential model [Eq. (4.1)]. When the discrete equation (4.11) is used, it is found that periodic, and even chaotic, behavior exists in daisyworld with one or two species, with the controlling parameter being the strength of the coupling between the daisies and the environmental temperature. Computations of the power spectra, fractal dimensions, and Lyapunov exponents verify the existence of periodic and chaotic behaviors in the model.

As shown in May (1976) and in Subsection 4.3.2, when the discrete equation (4.11) is used, chaos is possible when the feedback is excluded. Chaos is also possible, as shown in this chapter, when the feedback is included under the condition that the coupling to the environment is large enough that the daisies cannot respond quickly enough to achieve equilibrium.

These results show that daisyworld is not always in a steady state as predicted by the Gaia hypothesis; instead, the state of daisyworld can show extreme sensitivity to minor fluctuations in the effective temperature or the areas covered by daisies when in its chaotic regime. Therefore, the presence of daisies on the imaginary planet does not always stabilize the climate conditions of the environment, and the inclusion of negative feedback from the environment does not always lead to steady-state behavior.

## Chapter 5

# ERROR-GROWTH DYNAMICS AND PREDICTABILITY OF SURFACE THERMALLY-INDUCED CIRCULATIONS

In the previous two chapters, we have discussed two applications of chaos theory, i.e., data analysis and inspiration of new ideas. Another possible application of chaos theory, i.e., numerical model output analysis, will be discussed in this chapter. As an example, the error growth dynamics and the atmospheric predictability of surface thermally-induced mesoscale and small-scale circulations will be studied in detail. Several preliminary chaotic analyses of model output will also be presented, which improve our understanding concerning atmospheric predictability problems. (For the convenience of publication of this chapter, some materials in the previous chapters are repeated here.)

### 5.1 Introduction

The predictability problem of atmospheric flows encompasses, in principle, all the complexities of understanding of the atmosphere, since prediction is after all the true test of our understanding. Weather forecasting has been the driving force behind predictability studies; in fact, the predictability problem has been extensively studied only after the advent of numerical weather prediction in 1950s. Predictability studies help the improvement of forecasting and define the likely range of errors in any forecast, as demonstrated in ensemble forecasting (e.g., Murphy, 1988). In addition to its practical application, prediction is a fundamental theoretical issue in the analysis of nonlinear systems in various branches of science and engineering.

#### 5.1.1 Definition of predictability

In the general usage, the verb *predict* is defined as “to declare in advance, especially, to foretell on the basis of observation, experience, or scientific reason” (*Webster’s Ninth*

*New Collegiate Dictionary*). However, a precise and universally accepted definition of the term *predictability* has not been achieved. Traditionally, predictability is defined as the dependence of a system on the initial conditions. An unpredictable flow is one which exhibits a strong sensitivity. One possible reason for this narrow definition in the atmospheric sciences is that the early weather forecasting was based on the barotropic model which is affected only by the uncertainty associated with the initial conditions. This definition is also closely related to the Lyapunov exponents which are the average rates of exponential divergence or convergence of nearby orbits in phase space (Zeng *et al.*, 1991 and 1992b). Any system containing at least one positive Lyapunov exponent (and thus sensitive to initial conditions) is defined to be chaotic, with the magnitude of the positive exponent determining the time scale for predictability. In the pioneering work of Lorenz (1963) on chaos, it is demonstrated that the sensitive dependence on initial conditions (i.e., predictability) of a system is related to the aperiodic behavior of the system. In other words, when a nonperiodic behavior is observed, the system is unpredictable.

More generally, predictability also includes the sensitivity to boundary conditions and model parameters. For a very complex dynamical system such as the atmosphere, the “unperturbed” flow itself is a complicated function of space and time. Furthermore, a model-simulated flow may not be the correct flow for the system because of deficiencies of the numerical model, including uncertainties associated with parameters related to the parameterizations of subgrid processes and the numerical solution techniques. Just as the initial conditions cannot be determined accurately for such a complicated system, the boundary conditions and model parameters cannot be determined accurately. However, uncertainties in boundary conditions and model parameters introduce uncertainties at every moment rather than just at the beginning of the integration of the governing equations of the system. A problem related to predictability is the sensitivity of the atmospheric flow to subgrid variability of model parameters (especially those associated with surface properties, such as the roughness length) (Garratt *et al.*, 1990).

From an even more general point of view, the question of predictability is philosophical, since it concerns whether the future evolves precisely and deterministically from the

present. Just as relativity eliminated the Newtonian illusion of absolute space and time, and as quantum theory eliminated the Newtonian and Einsteinian dream of a controllable measurement process, chaos eliminates the Laplacian fantasy of long-time deterministic predictability. In this chapter, the sensitivity to initial and boundary conditions as well as model parameters will be studied, but the philosophical problem of predictability will not be discussed.

An important part of the definition of predictability is the quantitative characterization of the error growth. Two useful quantities are the error-doubling time  $T$  for small initial errors and the finite time  $T_s$  when the magnitude of the initial errors reaches a limited value slightly below the saturation level (e.g., 95% of the saturation level) which is estimated as the averaged difference between two randomly chosen model states. The reason for using a limit value slightly below the saturation level is to reduce the effect of sampling fluctuations. The error growth and these two parameters can be qualitatively illustrated with a simple example, which has been studied in Zeng *et al.* (1992b) for the computation of Lyapunov exponents. Fig. 5.1 shows the mean error growth for the logistic map  $z_{n+1} = 3.8z_n(1 - z_n)$  (Note that this Figure is the same as Figure 2.1.) The curve is characterized by the initial exponential stage, the intermediate quasi-linear stage, and the final saturation stage. All attractors and, more generally, all unstable dynamical systems having the property of mixing are expected to give rise to similar behavior (Nicolis and Nicolis, 1991). The first stage reflects local (linearized) properties, and the positive Lyapunov exponent as well as the error-doubling time can be obtained from the error growth in this stage. The error-doubling time  $T$  is independent of the magnitude of the initial error in this stage. The error-growth dynamics in this stage has also been studied by Farrell (1990), using a simple baroclinic shear model and a barotropic channel model with a localized jet. The remaining two stages depend on global properties (Nicolis and Nicolis, 1991). Note that, in contrast to the error-doubling time  $T$ , the finite time  $T_s$  when the mean error reaches 95% of the saturation level is dependent upon the magnitude of the initial error.

In addition to the above two quantities  $T$  and  $T_s$ , which are widely used in the predictability study of large-scale atmospheric phenomena, other measures are also used to

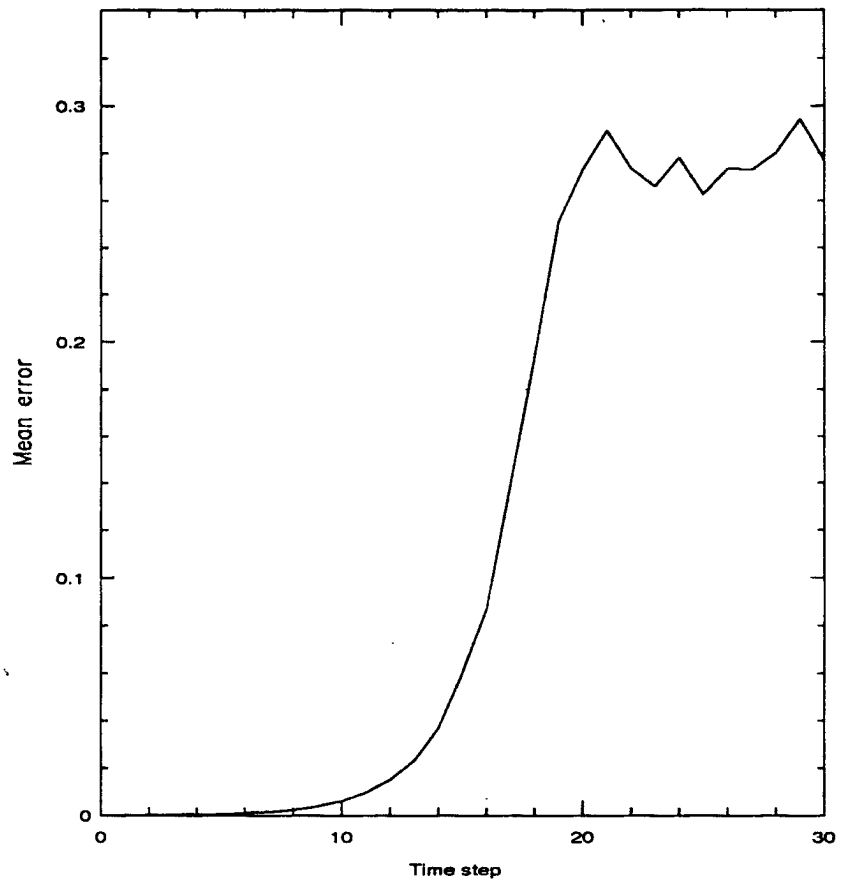


Figure 5.1: Mean error growth for the logistic map  $z_{n+1} = 3.8z_n(1 - z_n)$ .

evaluate or score the prediction. Some quantitative measures in evaluating mesoscale forecasts are reviewed in Anthes (1984a). One phenomenon may be indicated to be predictable by one measure but not by another. This is especially true for some mesoscale forecasts which are event-oriented. For example, it may be possible to predict the occurrence of a severe weather event with skill. If the measure of success is the simple prediction of the event's existence, this event is predictable. However, measures based on domain-averaged errors may show little predictability. An example is given in Anthes (1984a).

### 5.1.2 Large-scale atmospheric predictability

The atmospheric predictability study begins with the work of Thompson (1957), using a barotropic model and a two-level baroclinic model. Since then, most of predictability studies have concentrated on large-scale (i.e., synoptic and planetary scale) flow. These studies are based on three different approaches proposed by Lorenz (1969a). They include the dynamical, empirical, and dynamical-empirical approaches.

The empirical approach is based on the natural occurrence of analogs in the atmosphere, i.e., similar weather situations. This approach has been used in Lorenz (1969b) and Toth (1991a). This approach is the most attractive among the three approaches from a conceptual point of view, because it make use of real atmospheric behavior. However, it suffers from the absence of close analogs. The quantitative cumulative histogram for the number of analogs can be obtained as a by-product in the computation of the correlation dimensions [Eqs. (2.5)-(2.7)] (Grassberger and Procaccia, 1983a) (which will be used in this chapter) based on the entire global data sets (e.g., Pierrehumbert, 1990). The lack of close analogs provides an evidence that the atmosphere is aperiodic, and hence it cannot be predicted for a long time. Although close global analogs are rare, local close analogs can be obtained from observational data. However, after a few days, the local resemblance will be much weaker due to local forcing and/or large-scale advection processes. This kind of local predictability has been studied in Zeng *et al.* (1992a) (and in Chap. 3).

The dynamical-empirical approach uses derived equations for the errors, with observed spectral properties of the atmosphere appearing as coefficients. Among the three

approaches, only this approach treats the influence of smaller-scale errors on the larger-scale flow explicitly. However, it suffers from the limitation that the real atmosphere does not always behave like the idealized models, especially for mesoscale and small-scale phenomena. This approach was first used in Lorenz (1969c), for a study of error kinetic energy transfer between different scales in a two-dimensional turbulent flow with the quasi-normal approximation, and then used by Leith (1971) and Leith and Kraichnan (1972), using more general theories of two-dimensional turbulence. Instead of using the stationary energy spectra as in the above three papers, Metais *et al.* (1984) and Metais and Lesieur (1988) investigated the predictability of two- and three-dimensional freely-evolving turbulence, using the eddy-damped quasi-normal Markovian theory. The main conclusion of these studies is that initially small errors in any part of the spectrum (including at the smallest scale) will reach the neighboring scales first and then spread throughout the entire spectrum due to instability and nonlinearity of the flow. The predictability limit, defined as the time when the error kinetic energy reaches the kinetic energy of the basic flow at a given wavenumber, is inversely proportional to the wavenumber. The rate of upscale transport of small-scale error kinetic energy depends on the statistical structure of the small-scale flow field, especially its energy spectrum. The possible spectral gap in the mesoscale (which is explained in Lilly, 1989) has shown in Lorenz (1984b) and Lilly (1990) to lead to slower error spread through the energy spectrum than in the case without gap. Using the vorticity and thermodynamic energy equations for three-dimensional quasi-geostrophic flow, Thompson (1988) showed that whether the local error-variance grows or decays is crucially dependent upon the detailed structure and local scale of the basic field of potential vorticity, relative to the characteristic scale of the error fields. If the local scale of the vorticity field is very large, the error-variance grows very slowly or may even decrease; if it is very small, i.e., strong gradients of potential vorticity are confined to small regions, the error variance grows rapidly as a manifestation of the strong baroclinic instability.

The dynamical approach is based on numerical forecast models. The traditional predictability (i.e., sensitivity to initial conditions) is usually studied. This approach is

used most widely among the three approaches. It suffers from the fact that the growth of errors is model-dependent because of deficiencies of different models. The early such studies are summarized in Charney *et al.* (1966) and by Smagorinsky (1969). The more recent and detailed study of this type has been that of Lorenz (1982), using the ECMWF operational forecasts of a 100-day sequence. The error growth curves in Lorenz correspond with the quasi-linear stage in Fig. 5.1, because the initial analysis error is not very small and the saturated level has not been reached due to integration of only 10 days. It is shown in Lorenz that the lower bound on atmospheric predictability of the instantaneous weather patterns, based on the comparison of numerical forecast and analysis, is about 10 days, and the upper bound, based on the twin experiments, is about 14 days by extrapolation (since only 10-day forecasts were available). Dalcher and Kalnay (1987) extended the work of Lorenz (1982) by including the effect of growth of errors due to model deficiencies, using the same ECMWF data set. A similar predictability study is also carried out by Chen (1989), using the DERF data set which is a series of successive 30-day integrations with initial conditions separated by 24 hours conducted at the National Meteorological Center (NMC), and similar results are obtained. The true upper bound results from the instability and nonlinearity of atmospheric flows, which may be different from the upper bound determined from the twin experiment. The difference between the upper and lower bounds is caused by the deficiencies of the forecast model, especially those associated with the parameterization of unresolved or poorly resolved scales; the magnitude of this difference is also affected by the first-day forecast errors. When the first-day forecast is improved with the introduction of four-dimensional data assimilation, e.g., by the adjoint method (e.g., WMO, 1990), and with the improvement of the numerical model, the difference will be decreased. When the model is improved, the lower bound will be increased, but it is not quite certain whether the upper bound will be unchanged, decreased, or increased. Further work on this problem is needed.

The error-doubling time of about 2.5 days for small errors is obtained by Lorenz (1982) by extrapolating the error-growth curves to small errors, assuming that the nonlinear terms in the error-growth equations are quadratic. When extrapolation is required, the

error-doubling time will be sensitive to the method of extrapolation and hence is not a good measure of error growth, as pointed out in Dalcher and Kalnay (1987), since the exact location dividing the initial exponential and the quasi-linear regimes in Fig. 5.1 is unknown. In general, however, the error-doubling time is a very useful parameter to characterize the initial exponential stage in Fig. 5.1. A linear extrapolation to small errors is used in Chen (1989). However, this is correct only for an extrapolation to errors which are not so small.

Other studies using the dynamical approach include the dependence of predictability on the scales of the flows (Baumhefner, 1984; Dalcher and Kalnay, 1987; and Schubert and Suarez, 1989), on the flow regimes (Déqué, 1988; Palmer, 1988), on the time average (in contrast to the instantaneous values) (Roads, 1986), and on measures of forecast skills (Anthes, 1984a; Toth, 1991b). Many conclusions from these studies can be conceptually understood by Fig. 5.1. For example, the curve in Fig. 5.1 is an average of 400 different error-growth curves. The predictability based on different curves is different, or, more quantitatively, the average growth rate is different from the most probable for a given event (and a similar argument is also discussed in Benzi and Carnevale, 1989). In other words, predictability is case-dependent, or dependent on the flow regime in the case of the atmosphere.

The potential predictability of the low-frequency component of atmospheric motion (e.g., monthly and seasonal means) has been studied by, e.g., Shukla (1981). It is argued that the low-frequency component is more predictable because it is mainly forced by slowly varying boundary conditions. The predictability on the time scales of months to 15 years has been studied by Goswami and Shukla (1991 and references therein), using a coupled ocean-atmosphere model. On the scales of months to centuries, numerical prediction is basically a boundary-value problem for the atmospheric model when coupling to the ocean and biosphere is not included. However, for the coupled atmosphere-ocean-biosphere climate model, the numerical prediction is still an initial- and boundary-value problem, and sensitivity to initial conditions (especially those of the deep ocean) is expected.

### 5.1.3 mesoscale atmospheric predictability

Usually, mesoscale phenomena are divided into two groups: terrain-induced mesoscale systems and synoptically-induced mesoscale systems (Pielke, 1984). However, for mesoscale predictability studies, it is convenient to use four classes on the basis of categorization of the evolution of mesoscale phenomena. These four categories are (Lilly, 1984): (a) nearly homogeneous turbulent flow with well-defined variance spectra; (b) frontal and jet-like near-discontinuities, arising out of large scale processes (i.e., synoptically-induced systems); (c) response to small-scale topographic forcing (i.e., terrain-induced systems); and (d) large amplitude instability.

In contrast to large-scale predictability studies, mesoscale atmospheric predictability studies emerged only about 10 years ago. They differ from those of the large scales in several ways. In general, the energy spectrum (including the occurrence of intermittency), model resolutions, and instability mechanisms are different. Besides, mesoscale predictability is strongly affected by large-scale forcing by means of the lateral boundary conditions and small-scale surface forcing. Specifically, for category (a), the approach to predictability analysis is similar to that for the large scales, except using the mesoscale energy spectrum, and the mesoscale predictability time is shorter than that for the large scales. For category (d) such as convective storm systems, a shorter predictability time than quiescent weather in category (a) is expected. However, for a particularly important high-energy convective storm type, such as rotating super-cell storms in the presence of a well-defined stable lid at the top of the boundary layer, evidence from theory, observation, and numerical models suggest that their stable coherent structure enhances the stability and predictability, and their predictability time is much longer than turbulence predictability theory (e.g., Lorenz, 1969c) would suggest, partly due to the effects of helicity acquired from the mean state and amplified by buoyancy (Lilly, 1990, and references therein).

Most of the previous mesoscale predictability studies have fallen into the category (b), i.e., mesoscale systems forced by instabilities in traveling large-scale disturbances, which are studied in a numerical model in a domain of a few thousand kilometers in

length with grid spacings of about 50 to 100 kilometers. A numerical model in such a domain and with such a resolution is often called a regional model. Early studies are summarized in Anthes (1984b) and Anthes *et al.* (1985). The major and surprising conclusion is that the twin experiment of slightly different initial conditions shows little or no error growth over a period of 3 days under the condition of the same lateral boundary conditions. In contrast, using a global model with coarser resolution, errors grow with time in the same regional model domain. Therefore, the high predictability in regional models with grid increments of 50 to 100 km is contrary to the pessimistic conclusion from turbulence theory (e.g., Lorenz, 1969c) and is different than the results from the large-scale predictability studies. Later studies have attempted to explain this controversy. Possible explanations are offered in Errico and Baumhefner (1987), Paegle and Vukicevic (1987), Anthes *et al.* (1989), Van Tuyl and Errico (1989), Vukicevic and Errico (1990), Vukicevic and Paegle (1989), and Warner *et al.* (1989). A more recent review is given in Paegle *et al.* (1990). These explanations include the strong diffusion in the model which smooths the error fields at small horizontal scales but only slightly affects the fields in the control or perturbed runs due to diabatic or adiabatic processes (Errico and Baumhefner, 1987; Van Tuyl and Errico, 1989). Another reason for the enhanced predictability is the effect of the geostrophic adjustment process on the initial errors: part of the initial perturbations are projected onto gravity waves which interact only weakly with other, more significant motions (Warner *et al.*, 1984; Errico and Baumhefner, 1987). The third reason is the surface forcing which tends to form coherent structures, such as the sea breeze, which is insensitive to initial conditions (Paegle *et al.*, 1990). The last and maybe the most important reason is the constraints of the lateral boundary conditions. One constraint is the "sweeping out" of errors by correct or perfect lateral boundaries (Errico and Baumhefner, 1987). This mechanism may be weak at the beginning, since it is by advection. However, after a certain time (e.g., 36 hours), the whole domain will be strongly affected by the lateral boundary values. Another constraint of the lateral boundaries is the imposition of the largest spatial scale, through the specified lateral boundary conditions, that can react to the internal data uncertainty (Vukicevic and Paegle, 1989). When the

domain is not large enough (e.g., less than 7000 km), a substantial portion of the large scale flow in the domain is pre-specified, and the initial errors will not grow because of the slow interaction between the error field and the flow field due to the separation of scales, as suggested by Thompson (1957) and Lorenz (1969c). Note that this argument is based on the integral (rather than local) lateral boundary effect in the barotropic model (Vukicevic and Paegle, 1989). It is also demonstrated in Vukicevic and Errico (1990) using a complex limited-area model that, if the domain is sufficiently large, forecast differences grow with time, but only at large scales. Although the errors do not grow in the above studies due to the above reasons, the prediction of explosive cyclones, which are characterized by strong baroclinic instabilities, is still sensitive to initial uncertainties, including the magnitude and spatial distribution of initial errors in regional models (Kuo and Low-Nam, 1990).

For the category (c) situation, i.e., the surface-induced mesoscale systems, a longer predictability time than expected from turbulence predictability theory (e.g., Lorenz, 1969c) is anticipated. The surface forcing is basically linear, and can be suppressed by synoptic wind. Besides, instability on these scales is different from that for the large scales. Although strong surface forcing is used to explain the enhanced predictability for the synoptically-induced flow, there are very few predictability studies on these surface-induced mesoscale systems themselves. One such study is that of Berry and Paegle (1990) in which a hydrostatic, anelastic model is used to study the predictability of a sea breeze type of circulation. Note that there are quite a few studies on these systems which are not directly related to the predictability problem (Pielke, 1984; Schadler, 1990; Pielke *et al.*, 1992a, and references therein).

For mesoscale simulations, nested models should be used; otherwise, both the top and lateral boundary layers should be removed as far as possible from the region of significant mesoscale perturbations. The influence of the lateral boundary conditions on the predictability of synoptically-induced mesoscale flows has already been mentioned above. The importance of the top boundary conditions (including the height and the form of the top) for different mesoscale systems is discussed in Pielke (1984). The importance of the parameterization of the air/soil or air/vegetation/soil interface (which is an internal

boundary condition) to mesoscale systems is also discussed in Pielke (1984). The sensitivity of mesoscale flows to model parameters has been reported in many studies. Note that the specification of the surface parameters, such as the roughness length, can be regarded as a part of the boundary conditions. However, usually (and in this study), the surface parameters are regarded as a part of the model parameters.

All predictability studies mentioned above are carried out in the Eulerian frame. Atmospheric predictability can also be studied in the Lagrangian frame. A preliminary comparison between the Lagrangian and Eulerian predictabilities is given in Haidvogel and Holloway (1984). Further study is obviously needed.

The aim of this chapter is to systematically study the error-growth dynamics and the predictability of some surface thermally-induced circulations, and quantitatively evaluate the transition from organized flow to the less predictable flow in which fluxes are dominated by non-coherent eddies, by means of simulations of coarse resolution ( $\Delta x = 2$  km) and fine resolution ( $\Delta x = 100$  m). Such studies are of basic scientific value for their help in understanding turbulence dynamics and atmospheric predictability of large scales. The importance of organized surface forcing to predictability is also a critical problem in practice since, as discussed in Pielke *et al.* (1989), measurement-accuracy requirements in the atmosphere become increasingly more difficult as the spatial scale of the atmospheric forcing becomes smaller. Furthermore, such studies can improve the prediction of air quality on these scales and improve the parameterization of subgrid processes in large-scale numerical models.

Circulations caused by horizontal differential heating are created by such mechanisms as land-water contrasts, elevated terrain, urban-rural contrasts, gradients in soil moisture content, gradients in snow cover, variations in cloud shadowing, and contrasts in ground albedo and vegetation. Such thermal inhomogeneities may extend from a few square meters to hundreds or even thousands of square kilometers in the real world (Wetzel and Chang, 1988). We will concentrate on the circulations caused by the land-water contrasts, and it is anticipated that our results can be (at least qualitatively) applied to the circulations caused by other mechanisms. The nonhydrostatic, compressible numerical

model used in this study is discussed briefly in Section 5.2. The initial adjustment process and the error-growth dynamics of the circulations are studied in Section 5.3. The transition from organized local flow to the situations in which fluxes are dominated by non-coherent turbulent eddies, and the predictability as a function of the size of heat patches are quantitatively evaluated in Section 5.4. In Section 5.5, the results from three-dimensional simulations with two-dimensional surface forcing are compared with those of the two-dimensional simulations in Sections 5.3 and 5.4. Further analyses (including those based on chaos theory) of model output are presented in Section 5.6. Finally, conclusions are given in Section 5.7.

## 5.2 Numerical Models

Both two- and three-dimensional configurations of version 2C of the Regional Atmospheric Modeling System (RAMS) developed at Colorado State University are used in our study. We have carried out both mesoscale and fine-resolution simulations, which differ in the grid resolutions and turbulence parameterizations. RAMS is a merger of a nonhydrostatic cloud model (Tripoli and Cotton, 1989a,b, and references therein) and a hydrostatic mesoscale model (Pielke, 1974a; McNider and Pielke, 1981). It is a highly versatile numerical code of nonhydrostatic or hydrostatic, compressible, anelastic or incompressible primitive dynamical equations supplemented with one, or more than one, two-way interactive grid nestings, and with optional parameterizations of turbulence, radiation, moist processes (such as microphysics and cumulus convection), a soil layer, and a vegetation canopy. RAMS has been used successfully to simulate systems from compact atmospheric systems, such as tornadoes and boundary layer eddies, to mesoscale and synoptic systems. Overview discussions of RAMS are reported in Tremback *et al.* (1986), Cotton *et al.* (1988), Walko and Tremback (1991), Cotton *et al.* (1990), and Pielke *et al.* (1992b). Only options pertinent to our simulations will be discussed briefly.

### 5.2.1 Governing equations

The nonhydrostatic, fully compressible equations are used. RAMS solves prognostic equations in the atmosphere for the three velocity components ( $u$ ,  $v$ ,  $w$ ), potential temperature  $\theta$ , mixing ratio  $q$ , and perturbation Exner function  $\pi'$ , where the perturbation is

based on the difference from the initial state. The prognostic equation is also solved for the subgrid-scale turbulent kinetic energy  $e$  in the fine-resolution simulations.

### 5.2.2 Numerical schemes

The numerical scheme is described in Tripoli and Cotton (1982). The time-difference operator is a leap-frog scheme. An energy-conserving second-order scheme is used for the nonlinear advection terms. A time-split scheme is used so that a long time step can be used for advective processes and a shorter time step can be used for gravity-wave processes. Following Drogemeier (1985), the model sound speed is reduced. The model solutions are little affected as long as the reduced sound speed is at least a factor of 2 or 3 faster than the characteristic velocities of other disturbances, however, the efficiency of the model integration is increased by this sound speed reduction.

### 5.2.3 Parameterizations

Moisture is taken as a passive tracer, and no moist processes are considered. The radiation schemes are described in Chen and Cotton (1983a,b) for both the longwave and shortwave radiational tendencies. These schemes consider the radiative effects of condensate (which is not used in our study), water vapor, ozone, and carbon dioxide. The radiational tendencies are updated every 15 minutes. The soil model is described in Tremback and Kessler (1985), which solves the prognostic equations for the soil moisture and temperature. No vegetation canopy is included. A surface energy budget is calculated which includes shortwave and longwave radiative fluxes, latent and sensible heat fluxes, and conduction to and from the soil. The surface layer fluxes of heat, momentum, and water vapor into the atmosphere are computed using the scheme of Louis (1979).

For the fine-resolution simulations, boundary layer turbulence parameterization is based on the scheme of Deardorff (1980), in which the grid-averaged subgrid fluxes are diagnosed via down-gradient diffusion relationships. The eddy diffusivities are estimated as functions of the subgrid kinetic energy  $e$  which is computed from the prognostic equation of  $e$ . It was recently shown in Schumann (1991) that some parameters need to be modified in order to give reasonable results. However, the original scheme of Deardorff (1980) will

be used, and it is expected that the modifications recommended in Schumann (1991) will not change the conclusions. The Schumann scheme will be used in our future research.

For the mesoscale simulations used in this study, a first-order scheme is used. The formulation is similar to Smagorinsky (1963) with the modifications by Hill (1974) and Lilly (1962). The vertical and horizontal diffusion coefficients are

$$K_{Vm} = \frac{0.16}{\sqrt{2}} \Delta z^2 \sqrt{1 - 3R_i} [\sqrt{(D_{VH}^2)} + \sqrt{\max(0, -N^2)}] , \quad (5.1)$$

$$K_{Hm} = AKMIN * 0.075 * (\Delta x^2 + \Delta y^2)^{2/3} + \frac{0.25}{\sqrt{2}} (\Delta x^2 + \Delta y^2) \sqrt{(D_H^2)} , \quad (5.2)$$

$$K_{Vh} = 3K_{Vm}, \quad \text{and} \quad K_{Hh} = 3K_{Hm}, \quad (5.3)$$

where the subscripts  $H$  and  $V$  represent “horizontal” and “vertical”, respectively, the subscripts  $m$  and  $h$  represent “momentum” and “heat or moisture”, respectively.  $\Delta z$ ,  $\Delta x$  and  $\Delta y$  are grid increments in the vertical and horizontal directions, respectively.  $R_i$  is the Richardson number, and  $N$  is the Brunt-Vaisala frequency.  $D_{VH}$  is the three-dimensional deformation, and  $D_H$  is the deformation of only the horizontal components.  $AKMIN$  is the parameter to control the constant part of the horizontal diffusion coefficients.  $AKMIN$  is taken as zero. For convenience, the constant part of the horizontal diffusivity is denoted as  $K_{H0}$ , the deformation part is denoted as  $K_{HD}$ , and  $K_{H0} + K_{HD}$  is denoted as  $K_H$ .

A fourth-order filter, which is denoted as `FILT4`, can also be used in the model. This filter is very efficient in removing short waves (Walko and Tremback, 1991). `FILT4` is not used in the standard run. (When `FILT4` is used, it is activated every 10 minutes.)

#### 5.2.4 Boundary conditions

The lower surface of the atmosphere consists of soil only or of alternating soil and water strips of the same size in the  $x$ -direction. The roughness length is 0.2 m over the soil, and is computed over water from a formula similar to that of Clarke (1970). A constant water surface temperature of 293 K is used. The parameterization of the air/soil interface

has already been mentioned in the previous subsection. The soil moisture and temperature are constant at the bottom of soil which is 0.5 meter below the air/soil interface.

Periodic lateral boundary conditions are used to avoid the possible influence of lateral boundary conditions on the predictability as discussed in the Introduction. For sea-breeze type circulations, other lateral boundary conditions will yield similar results when the ambient wind is weak. The top boundary is a rigid top with a Rayleigh absorbing layer consisting of the upper 5 levels in the model. A relaxation time scale of 75 seconds is used. The purpose of the absorbing layer is to damp gravity waves and other disturbances which approach the top boundary, so that they will not be reflected back downward. A discussion of this boundary condition is given in Cram (1990).

### 5.2.5 Grid structure

The domain is located at 40°N. Cartesian coordinates are used. The grid stagger is the standard C grid (Arakawa and Lamb, 1981). This grid is staggered in both the horizontal and vertical directions. The eddy diffusion coefficients used in the mesoscale simulations are computed at the grid points for  $\theta$ .

For both fine-resolution and mesoscale simulations, 11 levels are used in the soil with the soil bottom at 0.5 m below the air/soil interface. For mesoscale models, 28 vertical levels (with the first level being the surface) are used with a grid spacing of  $\Delta z_2 = 40$  m near the surface for  $w$  and  $\Delta z_k = \min(1000 \text{ m}, 1.15\Delta z_{k-1})$  for  $k = 3, 4, \dots, 28$ . The second level for the horizontal velocities, temperature, and diffusion coefficients is 20 m above the ground, since a staggered grid is used. The domain top is at about 10 km.  $\Delta x = \Delta y = 2$  km. For the two-dimensional mesoscale model, 150 horizontal grids are used. For the three-dimensional mesoscale model, 50 (in  $x$ )  $\times$  40 (in  $y$ ) grids are used.

For the fine-mesh simulations, 40 vertical levels (with the first level being the surface) are utilized with  $\Delta z_2 = 40$  m near the surface for  $w$  and  $\Delta z_k = \min(100 \text{ m}, 1.1\Delta z_{k-1})$  for  $k = 3, 4, \dots, 40$ . The domain top is at about 3.5 km.  $\Delta x = \Delta y = 100$  m. 100 horizontal grids are used for the two-dimensional simulations. For the three-dimensional fine-resolution model, which is also called the large-eddy simulation (LES), 60 (in  $x$ )  $\times$  40 (in  $y$ ) grids are used.

### 5.2.6 Initial conditions

The initial time ( $t = 0$ ) is 6:00 am local standard time (LST) on July 1. All results are reported with respect to the time  $t$  rather than to the actual time. Initially, large-scale wind is zero, potential temperature is 293 K on the surface and increases with height at a constant lapse rate of  $\gamma = 4 \text{ K km}^{-1}$ . The time step is 15 seconds for the mesoscale model integration, and 4 seconds for the fine-resolution simulations. The model is integrated for 24 hours.

The initial soil temperature is the same as the surface temperature. The soil type is clay loam. The initial soil moisture is constant and is  $0.6\theta_{sat}$ , where  $\theta_{sat}$  is the saturation soil water content (Lee and Pielke, 1992).

### 5.2.7 Miscellaneous aspects

In the following sections, for convenience, the term *control run* is used to refer to the simulation without uncertainties or with very small initial uncertainties which are necessary to initiate the turbulence in the fine-mesh simulations, or to initiate inhomogeneities along the  $y$ -direction in the three-dimensional mesoscale simulations. The term *standard run*, denoted as ST, is used to refer to the control run with the initial and boundary conditions as well as model parameters as specified in this section (such as  $AKMIN = 0$ ). The term *perturbed run* is used to refer to a simulation with uncertainties in the initial conditions. The term *signal* is used to refer to the root-mean-square (RMS) difference of a variable  $a$  (denoting  $u$ ,  $v$ ,  $w$ , or  $\theta$ ) at time  $t$  and at the initial time:

$$RMSC(a) = \left[ \frac{1}{N} \sum_{D_o} (a_c(t) - a_c(0))^2 \right]^{1/2}. \quad (5.4)$$

The term *noise*, *error*, or *uncertainty* is used to refer to the RMS departure of a perturbed run from the control run:

$$RMSP(a) = \left[ \frac{1}{N} \sum_{D_o} (a_p(t) - a_c(t))^2 \right]^{1/2}. \quad (5.5)$$

In Eqs. (5.4) and (5.5), the subscripts  $p$  and  $c$  denote the perturbed and control runs, respectively;  $D_o$  denotes the subdomain in which  $RMSC(a)$  and  $RMSP(a)$  are computed;

and  $N$  denotes the number of  $a$  in the subdomain  $D_o$ . In addition to RMSC and RMSP, the quantity RMSD is used to denote the RMS difference between two simulations, and is also used to denote RMSC or RMSP in some figures for brevity.

When  $\text{RMSC}(a)$  is larger than  $\text{RMSP}(a)$ ; i.e., the signal/noise ratio is greater than unity, the prediction is meaningful for the variable  $a$ . When the signal/noise ratio is less than unity, the forecast is worthless. Note that this measure of predictability is somewhat different from those (such as the error doubling time and the finite time  $T_e$ ) mentioned in the previous section. Another measure of predictability used in this chapter involves the error growth characteristics.

The sensitivity of the field of a variable  $a$  to boundary conditions or model parameters depends on the ratio of the signal  $\text{RMSC}(a)$  over  $\text{RMSD}(a)$  which is the RMS difference between two simulations of different boundary conditions or model parameters. When this ratio is much larger than unity, the variable is insensitive to the boundary conditions or model parameters. When it is close to or less than unity, the variable is sensitive to the boundary conditions or model parameters.

In practice, because of the small size of the domain, initialization, or, more generally, four-dimensional data assimilation (4DDA), of the model is often based on very limited conventional observations. In this case, the actual initial data uncertainties on these scales are more likely to be systematic rather than random. On the other hand, with unconventional measurement techniques, such as profiler, satellite, lidar, and radar, enough observations can be obtained for 4DDA of the model. In this case, random initial uncertainties are more appropriate. In this study, the initial uncertainties are a combination of random and systematic errors: they are pseudo-random numbers (between 0 and 1) multiplied by a coefficient. In other words, the initial uncertainties are random with a non-zero mean value. Initial perturbations are applied to all grid points. The perturbations of model parameters or boundary conditions can be systematic or random. Only the systematic perturbations are used in this study. The random perturbations of the boundary conditions and model parameters at different grid points and the random subgrid variability of model parameters will be studied in the future.

In the following sections, in addition to the standard run (ST), different initial and boundary conditions, as well as model parameters, will be used for sensitivity studies, in which case the changes will be explicitly stated. Results in this chapter are based on more than 200 simulations. Most of the simulations are made for 24 hours starting from 600 LST, but our discussion will concentrate on the first 12 hours (i.e., daytime).

### 5.3 Error-Growth Dynamics

In this section, two-dimensional mesoscale simulations are carried out to understand the error-growth dynamics of surface thermally-induced mesoscale systems. The surface consists of land of 100 km surrounded by water for 100 km on both sides. The subdomain  $D_o$  in Eqs. (5.4) and (5.5) is the whole domain (denoted as subdomain A), or the subdomain in the lower 22 levels (below 4.5 km) (denoted as subdomain B), or the subdomain in the lower 17 levels (below 2 km) (denoted as subdomain C).

#### 5.3.1 Influence of initial uncertainties

The influence of the characteristics of initial uncertainties (e.g., the horizontal scale and the magnitude) on the predictability of regional models is emphasized by Errico and Baumhefner (1987) and Warner *et al.* (1989). For the smaller domain in our study, the impact of initial perturbations may be different due to different initial adjustment processes.

In order to understand the initial adjustment process, we first run RAMS without any diabatic processes (i.e., removing radiation, diffusion, and surface heating terms). It is found that the decrease of  $u'_0$ , when the initial perturbations are introduced into the  $u$  field, is slower than that of  $\theta'_0$ , when the initial perturbations are introduced into  $\theta$  field. For instance, after integration of 15 minutes,  $\text{RMSP}(u)$  decreases by 3.5% compared with the initial value of  $\text{RMSP}(u)$  in the subdomain C. In contrast,  $\text{RMSP}(\theta)$  decreases by 8.8% for the same period. This means that the mass field adjusts to the velocity field as a whole, although the adjustment process is different for different vertical normal modes. Our computations also show that the adjustment process is basically completed within

half an hour, because the magnitudes and the scales of the random perturbations are small.

Numerical experiments show that the adjustment process with the Coriolis force  $f$  are very close to that without  $f$ . In order to study the effect of the hydrostatic adjustment by vertical sound waves, simulations with hydrostatic or anelastic approximation can be performed. However, this involves different numerical solution techniques and different boundary conditions in RAMS, compared with the standard run. Therefore, it is difficult to study the influence of this adjustment process directly in RAMS. It is expected that this adjustment process is more important in our studies than in large-scale dynamics, but that it is still unimportant compared with the adjustment process by the gravity waves in our studies, because the adjustment time by sound waves is much shorter than 30 minutes. Therefore, the geostrophic adjustment process for our studied domain is the balance between the horizontal pressure gradient term and the nonlinear advection terms resulting from gravity wave propagation. Qualitatively, the adjustment process for initial perturbations of  $\theta$  can be described as follows:  $\theta'_0$  induce pressure perturbations  $p'$  mainly through the hydrostatic equation, and  $p'$  induce  $u'$  through the momentum equation for the  $u$ -component, and  $u'$  then induce  $w'$  mainly through the continuity equation. In this case, the available potential energy (which is proportional to the variance of  $\theta'$ ) is converted into the perturbed kinetic energy. In contrast, initial perturbations of  $u$  induce  $w'$  through the continuity equation, and  $w'$  induce  $\theta'$  mainly through the term of  $w'$  multiplied by the environmental stratification in the thermodynamical equation. In this case, the energy conversion process is reversed.

Using the above qualitative description, the adjustment process of different forms of initial perturbations can be understood easily. For instance, in one case, initial perturbations of  $\theta$  (i.e.,  $\theta'_0$ ) are random between 0 and 0.2 K with a mean value of 0.1 K and RMS difference of 0.114 K, and in another case, the initial perturbations are  $(\theta'_0 - 0.1)$  so that the mean value is close to zero and the RMS difference is about 0.055 K. Our computations show that the error growth curves for  $u$  and  $w$  are very close between these two cases, because the mean value for the former case is very small, and available potential energy is

the same between these two cases. Note that, qualitatively, if the mean value is large so that the dynamics of the circulations is changed, the error growth curve will be changed even if the available potential energy is unchanged. When initial perturbations of  $\theta$  are systematic rather than random, the available potential energy is zero. Our computations show that the kinetic energy is also close to zero for the first hour of integration due to the lack of conversion of kinetic energy from the available potential energy and due to the weak forcing.

When the fourth-order horizontal and vertical advection schemes are used, the adjustment process is very close to that using the second-order schemes which are used for all other simulations. This means that implicit smoothing in the numerical schemes is unimportant. However, the explicit smoothing through the horizontal diffusion terms  $K_H$  or the fourth-order filter FILT4 can strongly affect the adjustment process. Fig. 5.2 shows the results for different cases in subdomain C. Results for the subdomains A and B are similar. It is seen that the adjustment process is strongly affected by numerical smoothing including  $K_{HD}$ ,  $K_{K0}$ , and FILT4. The effect of FILT4 denoted by the short dashed line, which is used every 10 minutes, is stronger than the deformation part of  $K_H$ , denoted by the dotted line, since FILT4 is very effective in removing perturbations of short wavelengths, and since  $K_{HD}$  is small. Also, the constant part of  $K_H$ , i.e.,  $K_{H0}$ , with AKMIN being 0.3, is about  $567 \text{ m}^2/\text{s}$  [or about  $2.1 \times 10^{-3}(\Delta x)^2/\Delta t$ ] for momentum, and its effect is also stronger than  $K_{HD}$ .

When surface heating and radiation processes are included, the adjustment process is very close to that without these diabatic processes, because the surface heating is weak within the first half hour of integration. If we take the state after the adjustment of initial random perturbations (within 30 minutes) as the "initial" perturbations, these "initial" perturbations are not random. Furthermore, our computations show that changing the starting time of the integration from 600 LST to 630 LST does not affect our results. Therefore, whether the initial perturbations at 600 LST are random or scale-dependent does not matter (and the important thing is the characteristics of the state after the initial adjustment for our studies), although it is important for large-scale problems due to a longer adjustment time (e.g., Errico and Baumhefner, 1987).

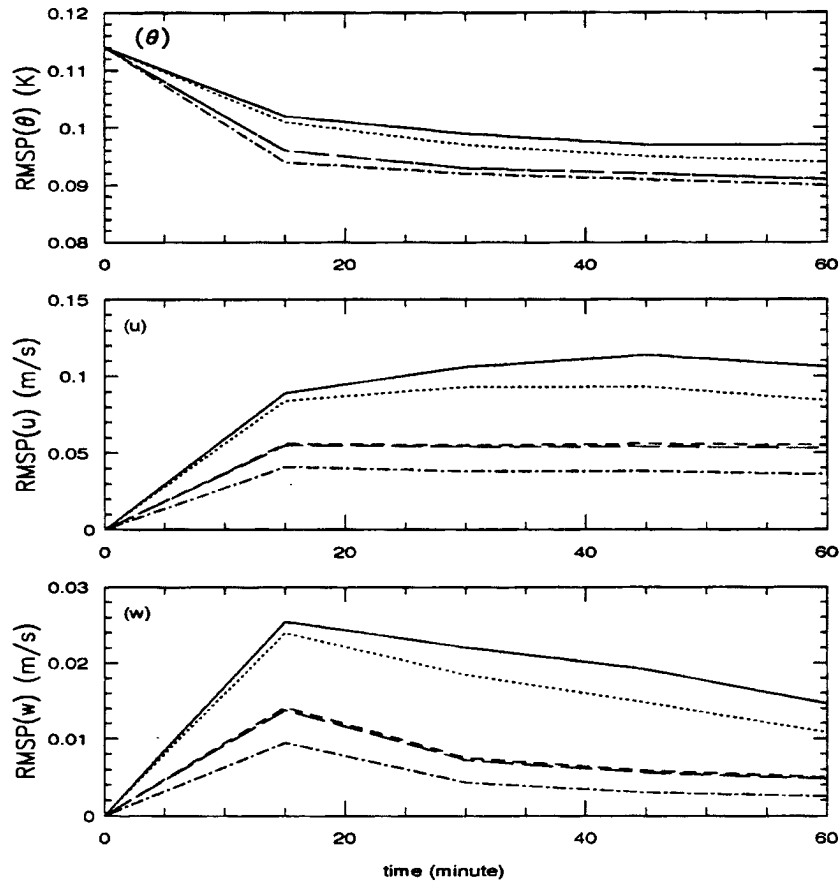


Figure 5.2: The first-hour adjustment process of the initial random perturbations  $\theta'_0$  with mean value of 0.1 K and RMS difference of 0.114 K in the subdomain C. The solid line denotes the standard run (ST) except without  $K_H$ , the dotted line denotes ST (where  $K_{HD}$  is used), the short dashed line denotes ST (except without  $K_{HD}$ ) with FILT4, the long dashed line denotes ST with FILT4, and the dotted-dashed line denotes ST with FILT4 and  $K_{H0}$  where AKMIN is 0.3.

In order to study the influence of initial error magnitude on error growth, we ran two simulations with different initial perturbations:  $\theta'_0$  with a mean value of 0.1 K and a RMS difference of 0.114 K (i.e., the standard run ST), and  $\theta'_0$  with a mean value of 1 K and a RMS difference of 1.14 K (denoted as case S2). Therefore the only difference between the two cases is that the initial perturbations in S2 are 10 times as large as in ST. Fig. 5.3 shows the results for both cases. It is seen that, after the results for S2 are scaled by a factor of 10, curves for both cases are relatively close for  $u$ ,  $w$ , and  $\theta$  for the first 5 hours. Furthermore, the change of RMSP between  $t = 0.5$  hour and 5 hours is small. It is expected that, although the surface forcing itself is not small, its influence on the error growth can be omitted due to weak motions during this period. Besides, the influence of nonlinear advection terms on the error field is quasi-linear and slightly smaller than that of diffusion, also due to weak motions. Therefore, the error growth is basically a quasi-linear process. We speculate that this is the reason for the above two features. The feature that the error growth curves of different initial magnitudes are parallel has also been observed in many predictability studies of large-scale flow (e.g., Lorenz, 1982; Dalcher and Kalnay, 1987; Chen, 1989), though no reasons are given in their studies. We speculate that the quasi-linear error growth occurs except near strongly baroclinic zones in their cases.

It is also seen from Fig. 5.3 that both RMSP( $u$ ) and RMSP( $w$ ) are similar for ST and S2 (without scaling) between  $t = 6$  and 12 hours when the surface forcing is strong. In other words, when the surface forcing is strong, coherent structures (i.e., the sea breeze circulations) appear, and the flow field is insensitive to the magnitude of initial perturbations. However, this alone cannot determine the predictability of the surface thermally-induced circulations. The signal (RMSC)-to-noise (RMSP) ratio needs to be computed in order to determine the predictability.

Therefore, for our studies, the error growth (at least at the stage when the surface heating is strong) is not very sensitive to the characteristics of the initial perturbations. In rest of the chapter, only random perturbations as in the case ST are used.

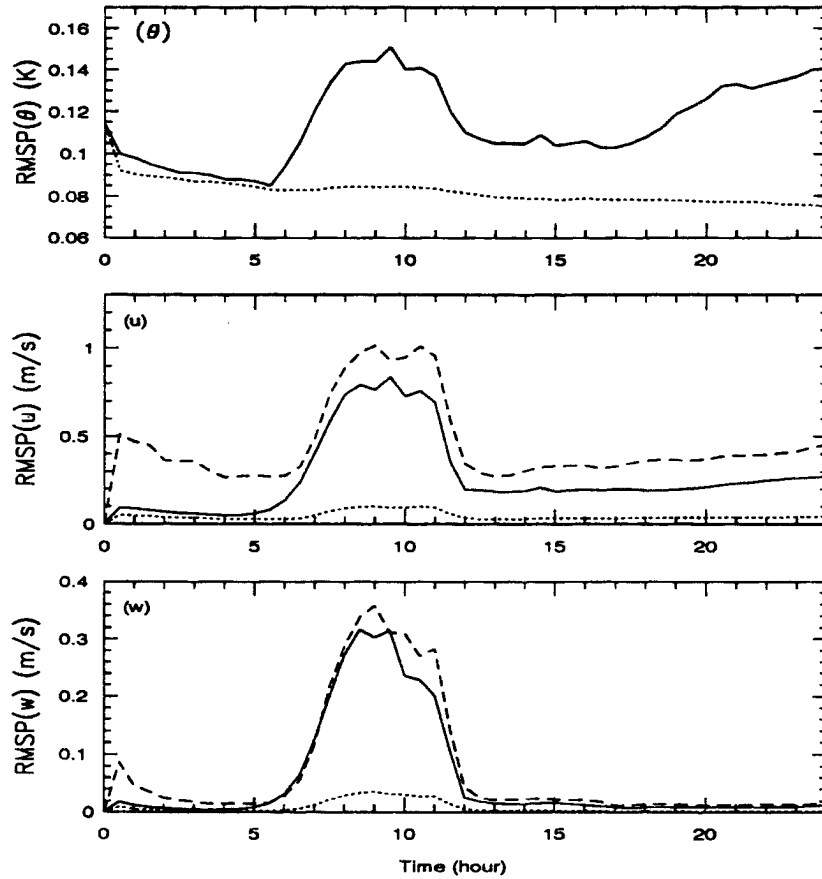


Figure 5.3: RMS for  $\theta$ ,  $u$ , and  $w$  in the subdomain C. The case ST is denoted by the solid line, and S2 is denoted by the dashed line. The dotted line is the dashed line scaled by a factor of 10. Note that the dashed line for  $\theta$  is not drawn for clarity.

### 5.3.2 Impact of numerical smoothing

In the previous subsection, the influence of numerical smoothing on the initial adjustment process was shown to be strong. In this subsection, its effect on error growth will be shown to be strong as well.

The error growth depends on the nonlinearity and instability of the flow. When the surface forcing is strong, turbulence is fully-developed, which leads to strong nonlinearity and convective instability, and hence leads to the growth of RMSP. On the other hand, the land/water contrast induces sea-breeze type of circulations which are strongest when the surface forcing is strong. These circulations are coherent and suppress the growth of RMSP. In addition, the error growth is also slowed by numerical smoothing. Fig. 5.4 summarizes the impact of different numerical smoothers on error growth. It is seen that, RMSP is small and decreases slightly from  $t = 0.5$  to 4 hours due to quasi-linear error growth as discussed in the previous subsection. In the case of no  $K_H$  or FILT4, RMSP increases rapidly from  $t = 4$  to 8.5 hours due to strong surface forcing and due to the lack of explicit numerical smoothing. The influence of numerical smoothers is also strong at this stage. The influence of FILT4, denoted by the short dashed line in Fig. 5.4, is stronger (weaker) than that of  $K_{HD}$  before (after) the time  $t = 9$  hours. When  $K_H$  is used, especially when  $K_H$  and FILT4 are used together, RMSP even decreases before the time  $t = 10$  hours — this changes the qualitative features of the error growth, compared with the case with  $K_{HD}$ . In order to understand the strong influence of numerical smoothing, we compute RMSD between the control run with  $K_{HD}$  (i.e., the standard run ST) and the standard run plus FILT4. It is found that this difference is only slightly smaller than RMSC in ST. In other words, smoothing by  $K_{H0}$  and FILT4 strongly affects the mesoscale flow.

Figure 5.5 describes the error growth for the cases S3 and S4, which are the same as ST and S2, respectively, except using both  $K_H$  and FILT4. In contrast to Fig. 5.3, the curves for S3 and S4 in Fig. 5.5 decrease slightly with time and are very close up to  $t = 8.5$  hours. This means that the increase of smoothing decreases the nonlinearity of the

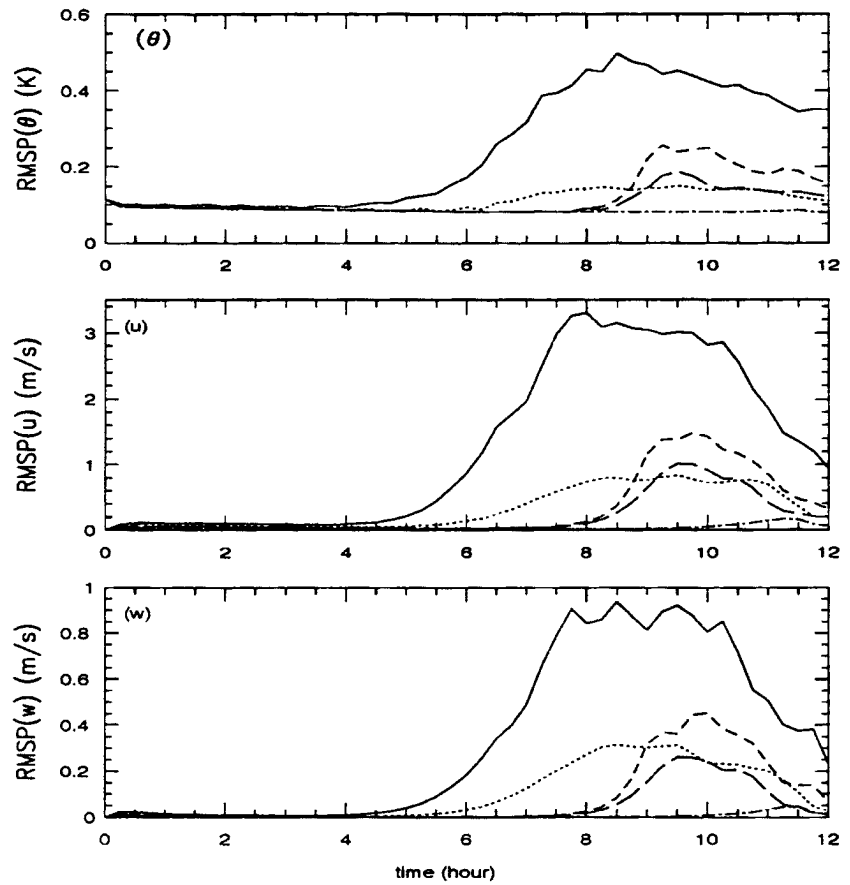


Figure 5.4: The same as in Fig. 5.2. except for an integration of 12 hours.

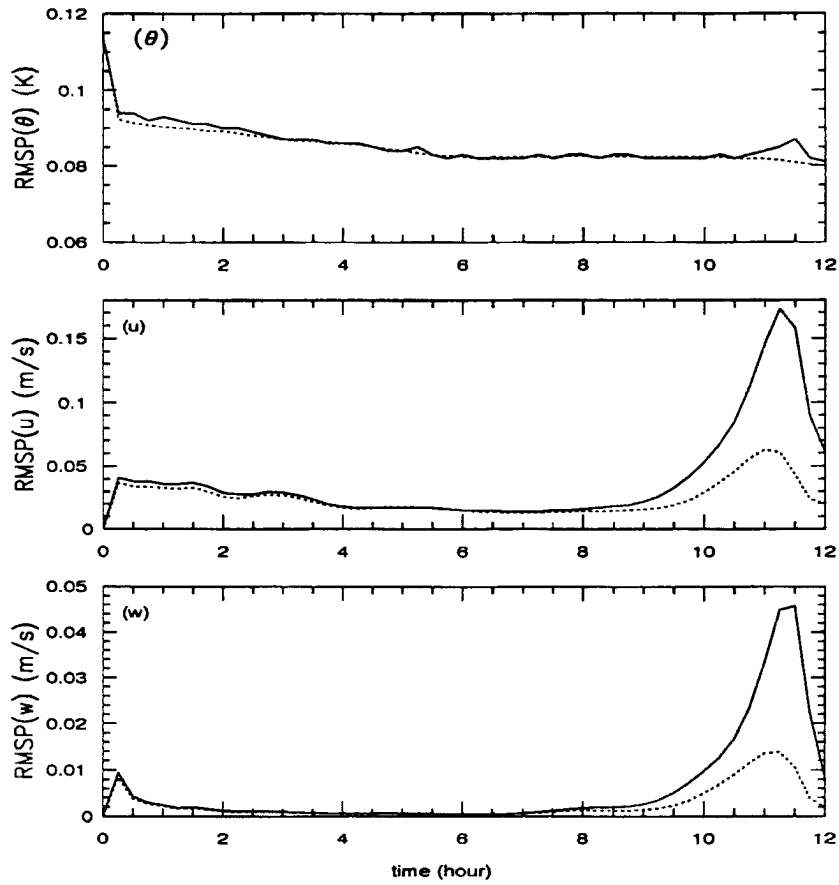


Figure 5.5: RMSP for  $\theta$ ,  $u$ , and  $w$  in the subdomain C with  $K_H$  and FILT4. The case S3 is denoted by the solid line, and S4, scaled by a factor of 10, is denoted by the dotted line.

mesoscale flow and extends the period in which the impact of nonlinear terms and surface forcing on the error growth is balanced by the numerical smoothing.

Theoretically, the influence of numerical diffusion is related to the turbulent Reynolds number which is  $LV/K$ , where  $L$  and  $V$  are representative length and velocity scales, respectively, and  $K$  is the turbulent exchange coefficient. With the increase of  $K_H$  by means of adding  $K_{H0}$ , the Reynolds number is decreased. For the first few hours of integration, the velocity and length scales are small; the increase of  $K_H$  may lead to a very weak turbulent flow or even laminar flow.

Another way to understand the influence of numerical diffusion is by considering the model equation in the schematic form

$$\frac{\partial a_k}{\partial t} = N_k + F_k - \nu_k a_k \quad , \quad (5.6)$$

where  $a_k$  is the amplitude of a spectral component  $k$  in the control run,  $F$  is the surface forcing,  $N$  is the nonlinear advection terms, and  $\nu$  is an effective diffusion coefficient.  $N$  is determined by  $F$ .  $F$  may be slightly affected by  $\nu$ , since  $\nu$  can affect  $a_k$ . The difference between the control and perturbed experiments, denoted by  $\delta$ , can be obtained from Eq. (5.6):

$$\frac{\partial \delta a_k}{\partial t} = \delta N_k + \delta F_k - a_k \delta \nu_k - \nu_k \delta a_k \quad . \quad (5.7)$$

It is expected that  $\delta F$  is smaller than  $\delta N$  in magnitude, since  $F$  is less affected by perturbations. It is also expected that  $a_k$  is more strongly affected by initial perturbations than  $\nu_k$  so that the ratio of  $\delta a_k/a_k$  is larger in magnitude than that of  $\delta \nu_k/\nu_k$ , or, equivalently, the term  $\nu_k \delta a_k$  is larger than the term  $a_k \delta \nu_k$  in magnitude. This is true especially when  $\nu_k$  contains both the constant and deformation parts. When the surface forcing is weak,  $\delta N$  may be smaller than the last term in Eq. (5.7) if the damping is strong. In this case, as shown by the dotted-dashed line in Fig. 5.4 for the first 10 hours or so, the difference fields decrease with time. When the surface forcing is strong, however,  $\delta N$  is larger than the last term in Eq. (5.7), and the difference fields increase with time.

### 5.3.3 Effect of boundary layer structure and surface heating

In order to understand the effect of overlying boundary layer structure and surface forcing, both RMSC and RMSP are computed. But, first, the dependence of the predictability of mesoscale flows on the variable is discussed.

Fig. 5.6 shows the signal and noise for the standard run ST. It is seen that, during the day, RMSC is qualitatively similar in shape for  $\theta$ ,  $u$ , and  $w$ , but the error growth is different for these variables. Especially, the signal/noise ratio is substantially different for these variables: it is much larger than unity for  $\theta$ , is larger than unity for  $u$ , and is close but less than unity most of the daytime for the  $w$  field. In other words,  $\theta$  is strongly predictable,  $u$  is predictable, and  $w$  is least predictable; a result which was also reported in Pielke *et al.* (1989).

The dependence of the predictability on the variable is well known from large-scale predictability studies, where the 500 mb geopotential height is often used. In our case, this phenomenon can be explained in different ways. In the mixing layer, the potential temperature is very well mixed, and the mixing depends on the surface heating. When  $\theta$  is perturbed, the mixing is hardly affected, since the surface heating is only slightly affected by these perturbations. Therefore,  $\text{RMSP}(\theta)$  is very small compared with  $\text{RMSC}(\theta)$  and changes little with time. The variable  $u$  is less well mixed than  $\theta$ , and the variation of  $\text{RMSP}(u)$  relative to  $\text{RMSC}(u)$  is larger than for  $\theta$ . For the variable  $w$ , both  $\text{RMSC}(w)$  and  $\text{RMSP}(w)$  are small, and slight differences of locations of upward and downward motions can substantially change  $\text{RMSP}(w)$ . Therefore the signal/noise ratio is low for  $w$ . Another way to explain these features is that the velocity field is related to the pressure gradient and the pressure is related to the temperature field through the hydrostatic equation. Therefore, slight variations of  $\theta$  can induce large variations of  $u$ , and the predictability of  $\theta$  is better than that of  $u$ . Similarly, the variable  $w$  is related to the gradient of  $u$  through the continuity equation, and its predictability is less than that of  $u$ .

When we change the date from July 1 to April 1; i.e., when we decrease the surface forcing, RMSC and RMSP are smaller than but similar to those in Fig. 5.6. When the latitude is changed from 40°N to 60°, 20°, or 0°N (so that the surface heating and the

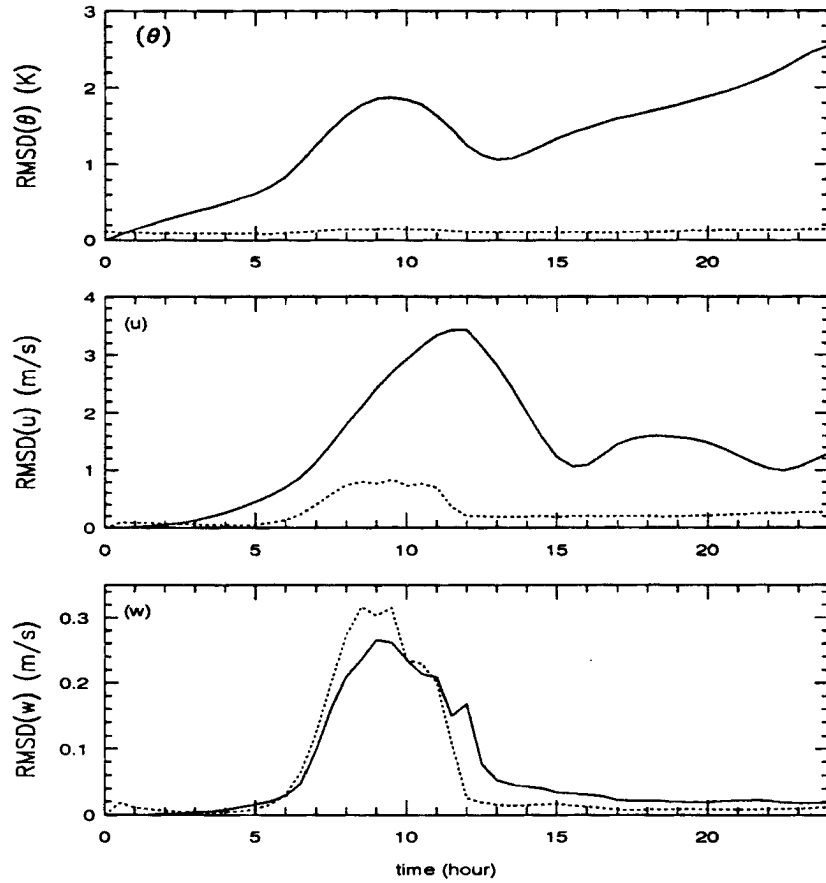


Figure 5.6: The signal (RMSC) and noise (RMSP) of  $\theta$ ,  $u$ , and  $w$  in the subdomain C for the standard run ST. The solid and dotted lines denote RMSC and RMSP, respectively.

Coriolis force are changed), qualitatively similar curves of RMSC and RMSP are obtained. When the initial stratification is changed from 4 K/km to 8 K/km, the stratification is more stable so that RMSC and RMSP are smaller than those in Fig. 5.6. Also, the signal/noise ratio for  $w$  is slightly higher than that in Fig. 5.6. Therefore, a more stable stratification improves the predictability slightly. When the initial stratification is changed from 4 K/km to 2 K/km, RMSC and RMSP are larger than those in Fig. 5.6, and the flow is slightly less predictable than in Fig. 5.6. Overall, the effects of these changes are noticeable for RMSC and RMSP, but are small in terms of the predictability; i.e., for the ratio of RMSC/RMSP.

It has been shown in Pielke (1984) that surface thermally-induced circulations are strongly affected by synoptic wind. In a more general sense, mesoscale flow is affected by large-scale forcing and surface forcing, and the latter itself is also affected by the former. Theoretically, the impact of the synoptic wind is two-fold: it increases the Richardson number and makes the flow less unstable during the day, and it suppresses the surface thermally-induced circulations. Based on simulations with synoptic winds of  $U = 3, 6,$  and  $9$  m/s, it is found that their influence on  $\text{RMSC}(\theta)$  and  $\text{RMSP}(\theta)$  is small. The synoptic wind decreases  $\text{RMSC}(u)$ , but does not change the signal/noise ratio significantly. However, the influence of synoptic wind on the  $w$  field is strong. Fig. 5.7 shows  $\text{RMSC}(w)$  and  $\text{RMSP}(w)$  for different synoptic winds. It is seen that, compared with the lower panel in Fig. 5.6 with calm synoptic wind, both the signal and noise decrease, and the signal/noise ratio is greater than unity with  $U = 3, 6,$  or  $9$  m/s. This means that, when the synoptic wind is changed from zero to  $3, 6,$  or  $9$  m/s,  $w$  is changed from unpredictable to predictable. Whether this is generally true for thermally-induced mesoscale flows needs further work. Further studies are also needed to explain the signal/noise ratio (which is smaller than unity) between  $t = 9$  and  $13$  hours with  $U = 6$  m/s.

#### 5.3.4 Sensitivity to boundary conditions and model parameters

In order to understand the sensitivity of the flow structure to different specifications in the model, we compute RMSD between the standard run ST and a simulation with different specifications. Note that RMSD is different from RMSP in that RMSP is the RMS

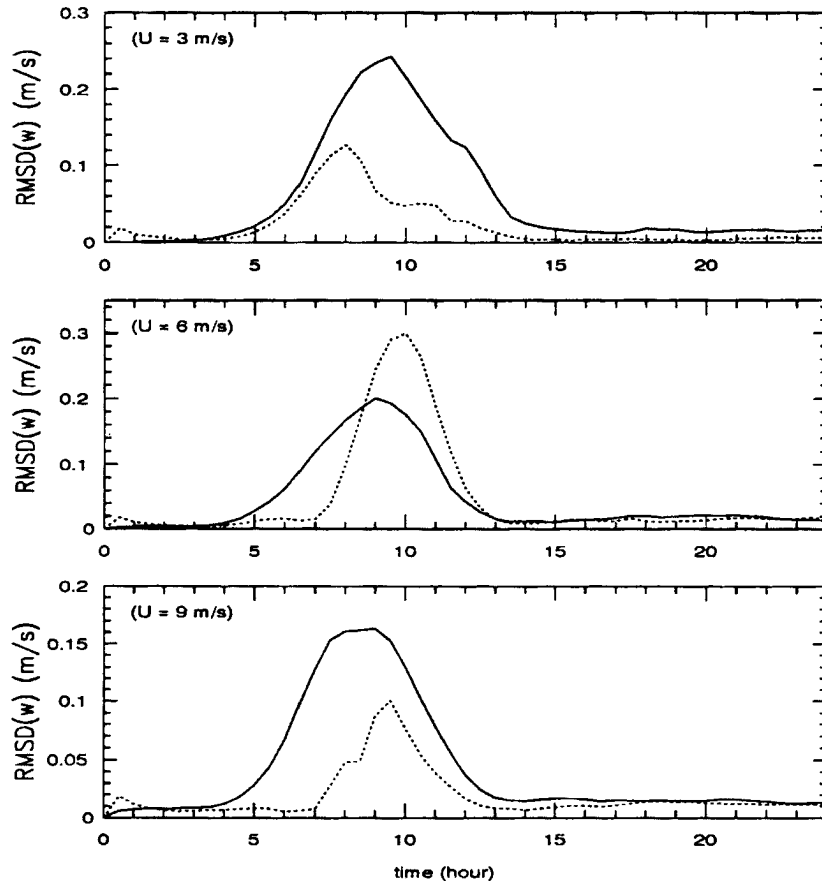


Figure 5.7: The signal (RMSC) and noise (RMSP) of  $w$  in the subdomain C for the same case as ST except with the synoptic wind  $U = 3, 6, \text{ or } 9 \text{ m/s}$ . The solid and dotted lines denote RMSC and RMSP, respectively.

difference between two runs with and without initial perturbations and is related to error growth, but RMSD is related to the influence of the specifications on the flow structure and is the traditional sensitivity analysis. Only systematic perturbations of boundary conditions or model parameters are used. The random perturbations of parameters at model grid points and the random subgrid variability will be studied in the future.

Our computations show that the surface thermally-induced mesoscale circulations are almost unchanged when the height of the model top is changed, or when the number of the levels or the relaxation time scale is changed in the Rayleigh absorbing layer. It is also found that, when different lateral boundary conditions (such as the zero gradient boundary conditions, the radiative boundary conditions, and enhanced diffusion near the boundaries) are used, the flow structures are very close to those using periodic boundary conditions under a calm synoptic wind. No simulations are carried out to study the sensitivity to the boundary conditions at the bottom of the soil, but insensitivity is expected. The sensitivity to the internal boundary conditions at the air/soil interface is not studied, but the sensitivity to parameters relating to the parameterization of the air/soil interface is discussed below. Therefore, surface thermally-induced mesoscale circulations are insensitive to top and lateral boundary conditions under a calm synoptic wind.

Our results show that, when the initial time is shifted from 600 LST by an hour, results are only slightly changed. When the surface roughness length is changed from 0.2 m to 0.05 m,  $\max[\text{RMSD}(\theta)] = 0.21 \text{ K}$  is small compared with  $\text{RMSC}(\theta)$  given in Fig. 5.6,  $\max[\text{RMSD}(u)] = 0.83 \text{ m/s}$  is not large compared with  $\text{RMSC}(u)$  given in Fig. 5.6, but  $\max[\text{RMSD}(w)] = 0.28 \text{ m/s}$  is large and comparable to  $\text{RMSC}(w)$  given in Fig. 5.6. The last point is consistent with that of Garratt *et al.* (1990) in that the main influence of roughness length change is on the vertical velocity. When the ratio of the diffusion coefficient for heat to that for momentum is changed from 3 to 1 in Eq. (5.3) and before  $R_i$  in Eq. (5.1), the influence is larger than that of changing the roughness length from 0.2 m to 0.05 m:  $\max[\text{RMSD}(\theta)] = 0.27 \text{ K}$ ,  $\max[\text{RMSD}(u)] = 1.0 \text{ m/s}$ , and  $\max[\text{RMSD}(w)] = 0.36 \text{ m/s}$ . As in the case of changing the roughness length, the major influence is on the vertical velocity. In a study on the influence of changing surface-layer parameterization constants, similar conclusions were reported in Garratt and Pielke (1989).

Soil water content should be between  $\theta_{wilt}$  and  $\theta_{fc}$ , which are the permanent wilting point associated with a soil water potential of  $-15$  bar, and the field capacity associated with a hydraulic conductivity of  $0.1$  mm/day, respectively (Lee and Pielke, 1992). For the soil type of clay loam used in our study,  $\theta_{wilt}$  and  $\theta_{fc}$  are  $0.53$  and  $0.68$  of  $\theta_{sat}$  which is the saturated soil water content. Several studies (e.g., McCumber and Pielke, 1981) reveal that, among many factors, the soil water content is one of the most important for the soil, although the soil water content and other factors such as soil type, vegetation, and albedo, are not independent. In ST, the initial soil moisture content is  $SLM \times \theta_{sat}$  where  $SLM = 0.6$ . Because of the small range of SLM (from  $0.53$  to  $0.68$ ) between very dry and very moist conditions, it is expected that a small change of SLM will strongly affect the surface energy budget in a complicated way (e.g., by changing the Bowen ratio, the albedo, and the soil thermal conductivity). Fig. 5.8 shows RMSD between the standard run ST (with  $SLM = 0.6$ ) and the runs with  $SLM = 0.54, 0.57, 0.63,$  and  $0.66$ . It is seen that, among the four different values of SLM used in Fig. 5.8,  $RMSD(\theta)$  is largest at  $SLM = 0.54$  for  $t < 8$  hours and at  $SLM = 0.66$  for  $t > 8$  hours,  $RMSD(u)$  is largest at  $SLM = 0.54$  for  $t < 11$  hours and at  $SLM = 0.66$  for  $t > 11$  hours, and  $RMSD(w)$  is largest at  $SLM = 0.54$ . Overall, RMSD caused by the change of SLM in these four cases is as large as the signal RMSC in the standard run ST. Therefore, the effect of soil water content is strong on the flow structure, which was also found in McCumber and Pielke (1981) and Schadler (1990). The strong influence of soil parameters on synoptically-induced mesoscale systems was also reported in Tremback (1991). Changes of soil moisture (which also determines the surface albedo in RAMS) over time can also cause substantial climatic changes (e.g., Charney, 1975; Idso, 1981).

One question that we do not address in this study is the influence of changing the grid spacing with a corresponding change of constants in the turbulence closure scheme. Our experience has shown that with the decrease of grid spacing, the constants such as  $0.16$  in Eq. (5.1),  $0.25$  and  $AKMIN$  in Eq. (5.2) need to be increased to suppress the numerical noise. The selection of these constants is usually arbitrary. A better way may be to use the higher-order closure scheme, e.g., the Mellor-Yamada level-2.5 scheme (Mellor and Yamada, 1974). We plan to study this question in the near future.

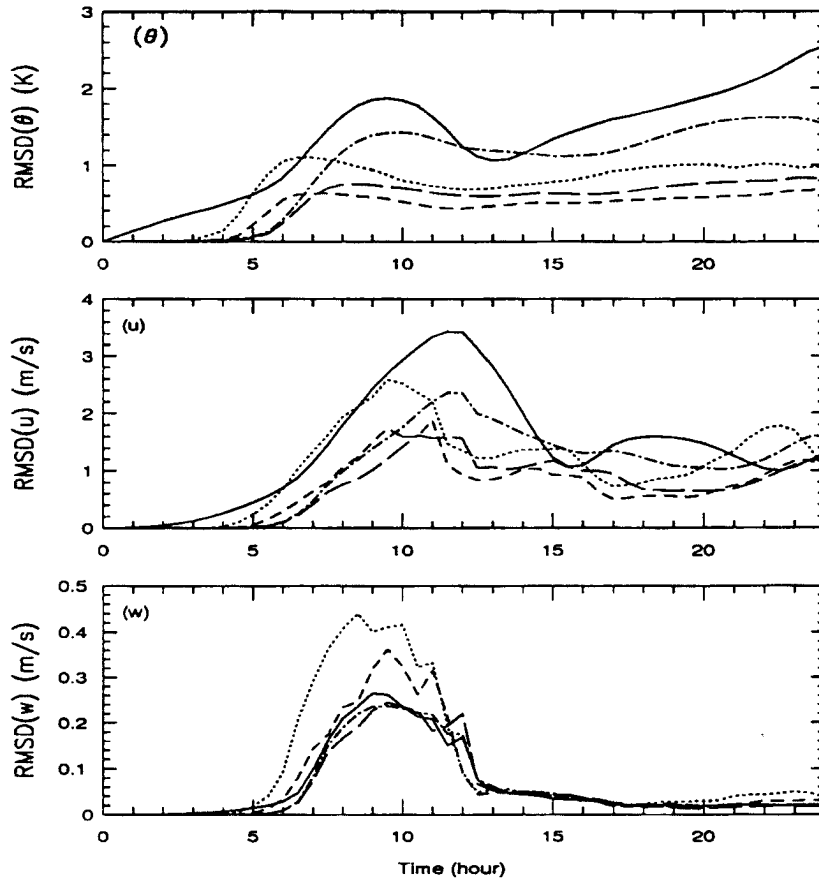


Figure 5.8: The RMSD of  $\theta$ ,  $u$  and  $w$  in the subdomain C between the standard run ST (with  $SLM = 0.6$ ) and the simulations of  $SLM = 0.54, 0.57, 0.63$ , or  $0.66$ . The RMSC for ST (same as the solid line in Fig. 5.6), denoted by the solid line, is drawn for comparison. The dotted, short dashed, long dashed, and dotted-dashed lines denote the cases of  $SLM = 0.54, 0.57, 0.63$ , and  $0.66$ , respectively.

#### 5.4 Predictability as a Function of the Size of Surface Heat Patches

In this section, the surface consists of alternating water and land strips with the size of each strip denoted by  $L$ . For the cases  $L = 0$  (i.e., homogeneous land), 1, 2.5, and 5 km, a 2-D fine-resolution ( $\Delta x = 100$  m) model is used. In these cases, the horizontal domain size is 10 km, and RMSC and RMSP are computed in the subdomain below 1.5 km. The perturbations are added at  $t = 2$  hours rather than at  $t = 0$ . For the cases  $L = 10$  to 150 km, a 2-D mesoscale model with  $\Delta x = 2$  km is used, and the horizontal domain size is between 280 and 360 km. In these cases, RMSC and RMSP are computed in the subdomain which is below 2 km and consists of an equal number of water and land strips. The synoptic wind is zero. Qualitatively similar results are obtained when other subdomains are used.

The influence of the width of land masses on the development of sea-breeze type circulations has been studied for the past twenty years or so. Neumann and Mahrer (1974, 1975) studied the thermally-induced circulations due to circular islands or lakes of different radii. Abe and Yoshida (1982) demonstrated the influence of the width of a peninsula on the development of a sea breeze. Mahrer and Segal (1985) studied the impact of both the geometry and size of the landmass on the sea-breeze circulations. More recently, Xian and Pielke (1991) studied similar problems, using a 2-D hydrostatic version of RAMS. Usually, the vertical velocity variation is emphasized in these studies. The influence of horizontally varying soil water content on the triggering of atmospheric convection was studied by Schadler (1990). Pielke *et al.* (1992a) demonstrated that the influence on the atmosphere of mesoscale landscape spatial variability must be parameterized (or explicitly modeled) in large-scale atmospheric model simulations including general circulation models, based on computations of the subgrid turbulent heat fluxes and the resolvable heat fluxes induced by surface inhomogeneities. The enhanced potential buoyant energy due to surface inhomogeneities (wet soil/dry soil) is suggested as a mechanism for potentially enhanced thunderstorm severity over and near irrigated locations in Pielke and Zeng (1989). In addition to the above numerical and experimental studies, Dalu and Pielke (1992) made an analytical study of the vertical heat fluxes generated by mesoscale atmospheric flow

induced by thermal inhomogeneities. Dalu *et al.* (1992) also evaluated the linear impact of thermal inhomogeneities on mesoscale flow with a calm mean wind. However, none of these studies focused at the predictability of the surface thermally-induced circulations.

Figures 5.9 and 5.10 show  $\text{RMSC}(w)$  and  $\text{RMSP}(w)$  with different sizes of heat patches under calm synoptic wind. It is seen that, when  $L = 0$  to 5 km where a fine-mesh model is used, the vertical velocity  $w$  is unpredictable. When  $L = 10$  to 40 km,  $w$  is predictable in mesoscale simulations since the signal/noise ratio is greater than unity. When  $L = 50$  to 70 km,  $w$  is marginally predictable. When  $L$  is increased beyond 70 km,  $w$  becomes unpredictable.

Figures 5.11 and 5.12 show the results for  $u$ . When  $L = 0$  to 2.5 km, the horizontal velocity field  $u$  is unpredictable. When  $L = 5$  km,  $u$  is predictable in the fine-resolution simulations. When  $L$  is greater than 5 km, the contribution of the coherent circulations should be larger than when  $L = 5$  km, so that it is expected that the  $u$  field should also be predictable in fine-resolution simulations. However, this requires further study. When  $L$  is greater than or equal to 10 km, it is also seen from Figs. 5.11 and 5.12 that the  $u$  field is highly predictable in mesoscale simulations.

Figures 5.13 and 5.14 show the results for  $\theta$ . For all cases including the case of homogeneous soil ( $L = 0$  km), the  $\theta$  field is highly predictable in both high-resolution and mesoscale simulations. The signal  $\text{RMSC}(\theta)$  consists of two parts: one is the RMS difference between the horizontally-averaged potential temperature  $\langle \theta \rangle$  and the initial  $\theta$ , denoted as  $\text{RMSC}(\langle \theta \rangle)$ ; the other is the RMS difference between  $\theta$  and  $\langle \theta \rangle$ , denoted as  $\text{RMSC}(\theta')$ . Note that  $[\text{RMSC}(\theta)]^2 = [\text{RMSC}(\langle \theta \rangle)]^2 + [\text{RMSC}(\theta')]^2$ . Our computations show that  $\text{RMSC}(\theta')$  is close to  $\text{RMSC}(\theta)$  when the turbulence is fully developed (e.g.,  $t = 5$  to 11 hours).

For a convective boundary layer with inhomogeneous surface forcing, the dependence of the predictability on the surface forcing is two fold: the strong heating leads to fully-developed turbulence, and the strong horizontal differential heating results in thermally-induced circulations at the same time. The former is noncoherent, turbulent, and basically unpredictable. However, the latter is coherent and predictable. By analyzing the autocorrelation and power spectrum, which will be discussed in Section 5.6, it is found that the

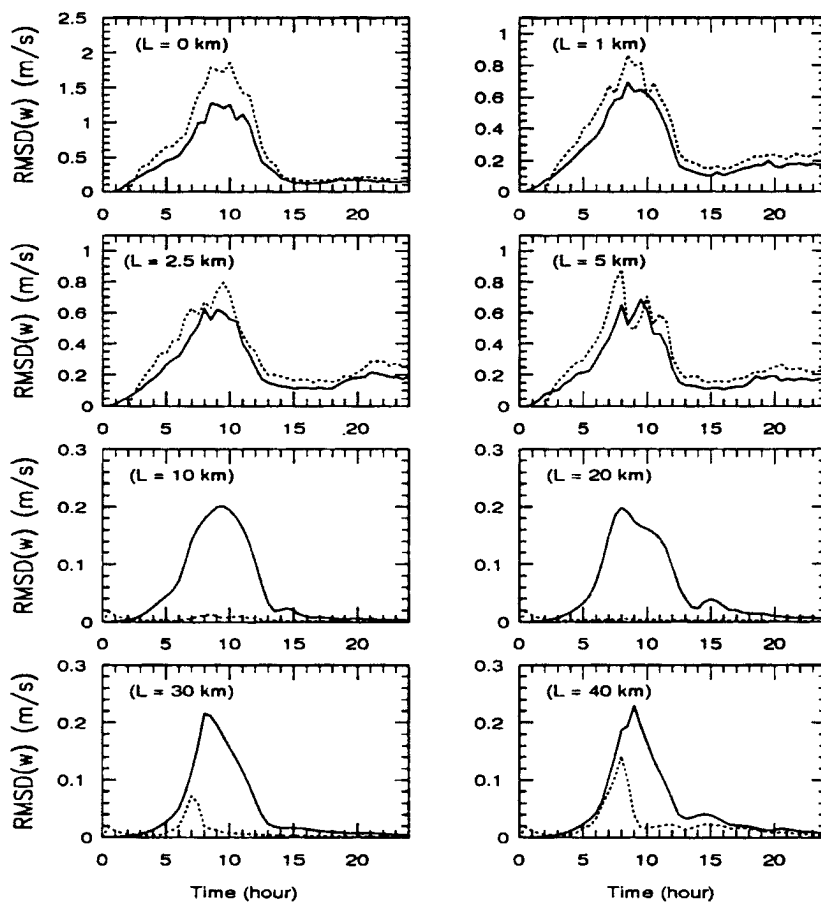


Figure 5.9: RMSD( $w$ ), denoted by the solid line, and RMSP( $w$ ), denoted by the dotted line, for  $L = 0$  to 40 km. Results for  $L = 0$  to 5 km are based on fine mesh model integrations with  $\Delta x = 100$  m, and results for  $L = 10$  to 40 km are based on  $\Delta x = 2$  km.

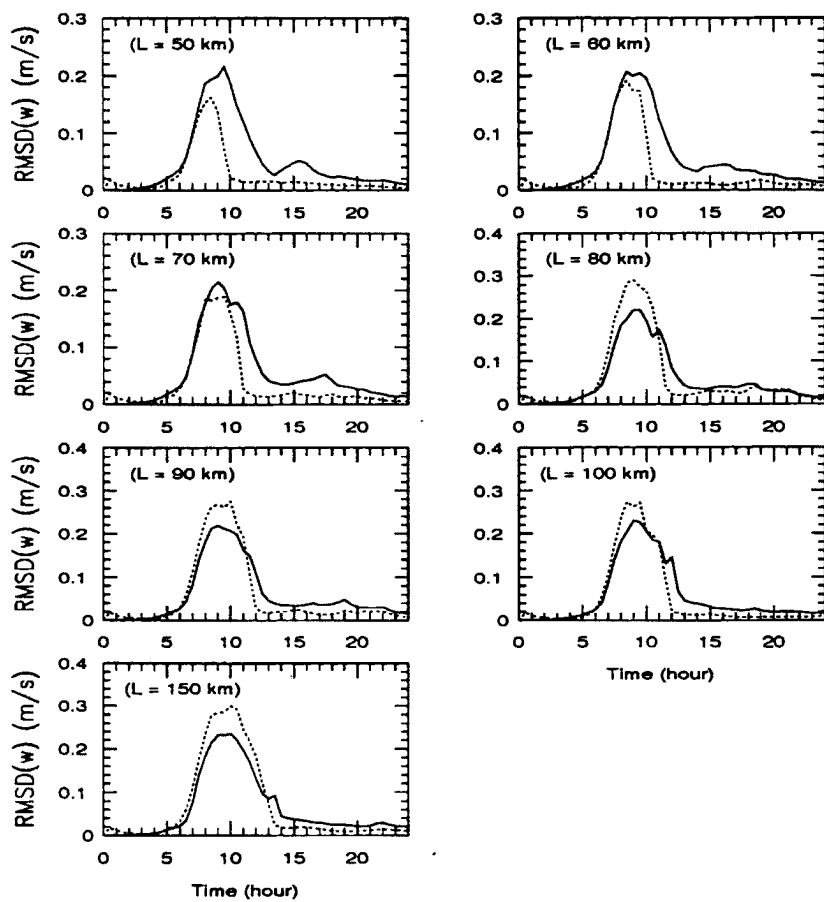


Figure 5.10:  $\text{RMSC}(w)$ , denoted by the solid line, and  $\text{RMSP}(w)$ , denoted by the dotted line, for  $L = 50$  to  $150$  km, based on  $\Delta x = 2$  km.

$w$ ,  $u$ , and  $\theta$  fields contain components of both coherent circulations and random motions. The relative importance of these two components depends on the size  $L$ . In addition, under the same conditions, the relative contribution of the coherent circulation component is larger for the  $u$  and  $\theta$  fields than for the  $w$  field. These are consistent with the conclusion in Krettenauer and Schumann (1991), and Walko *et al.* (1992) that long-time and phase averages in a realization are needed to exhibit the coherent circulations, especially for the  $w$  field. Since  $\theta$  is well mixed in a convective boundary layer with or without horizontal differential heating, the  $\theta$  field is highly predictable in all cases in Figs. 5.13 and 5.14. When  $L = 5$  km, the coherent circulations are strong for the  $u$  field so that  $u$  becomes predictable in high-resolution simulations. When  $L$  is greater than 5 km, the circulations are even stronger and  $u$  is very predictable in mesoscale simulations (and is expected to be correspondingly predictable in fine-resolution simulations).

When  $L$  is smaller than or equal to 5 km, the coherent circulations for the  $w$  field are not strong, as reflected in its power spectrum and autocorrelation which will be discussed in Section 5.6. Besides, the error field  $w'$ , i.e., the difference between the control and perturbed runs, shows large variations at both small and large wavelengths. In other words, because the coherent circulations are weak, even the component of the coherent circulations for the instantaneous  $w$  field is somewhat sensitive to initial perturbations. This is consistent with the conclusion in Walko *et al.* (1992) that, even when the time and space averages are used in a realization, the mean probability of occurrence of positive vertical velocity shows a very strong horizontal variation. Therefore,  $w$  is unpredictable in fine-resolution simulations for  $L = 0$  to 5 km. As  $L$  is increased, the coherent circulations become stronger, and  $w$  becomes predictable in mesoscale simulations with  $\Delta x = 2$  km for  $L = 10$  to 40 km. However, since the strength of the circulation depends on the grid increments, further work is needed in order to determine the range of  $L$  for which  $w$  is predictable in fine-resolution simulations with  $\Delta x = 100$  m.

When  $L$  is greater than 70 km, except near the coastlines, the flow is dominated by boundary layer turbulence, just like the homogeneous case, and  $w$  becomes unpredictable in mesoscale simulations. On the other hand, when  $L$  is greater than 70 km, the horizontal differential heating is very strong. Since AKMIN is zero in mesoscale simulations,

and since the turbulent flux terms in 2-D simulations actually contain both the subgrid contributions and the resolvable-scale fluxes which cannot be properly handled without including the third direction (Pielke, 1974b), strong upward motion can induce numerical noise. Therefore, whether or not  $w$  is unpredictable for  $L$  greater than 70 km requires further study.

When  $\Delta x = 2$  km is used for  $L \geq 10$  km, the boundary layer turbulence is parameterized, which, unavoidably, contains some arbitrarily-selected constants. Since  $\Delta x = 2$  km is close to the turbulence scale in the convective boundary layer, some sensitivity to the constants in the parameterization is expected (as has been demonstrated in the previous section). The problem of changing the grid increments with a corresponding change of parameterization constants will be studied in the future.

Note that the above results represent the predictability of a single realization of grid-volume-averaged variables. The predictability of a generalized ensemble average, i.e., an ensemble average of grid-volume-averaged variables (Cotton and Anthes, 1989), may be different. Since the control and perturbed runs can be taken as two individual realizations of an ensemble average, whether an ensemble average and a realization yield close results regarding the predictability is dependent upon the predictability of the single realization. When a variable is highly predictable in a realization, an ensemble average and a realization have the same predictability. In contrast, when a variable, such as  $w$ , is unpredictable in a realization due to a large chaotic motion component, an ensemble average may still be predictable if the chaotic motion component appears to be nearly random and can be removed significantly by averaging. Therefore, Figures 5.13 and 5.14 show that an ensemble average and a realization yield the same results regarding the predictability of  $\theta$  for fine-resolution and mesoscale simulations. Since  $\text{RMSP}(u)$  is comparable to  $\text{RMSC}(u)$  for  $L = 0$  to 5 km in the fine-resolution simulations with  $\Delta x = 100$  m; i.e., the variation of the  $u$  field is large from one realization to another, the predictability of an ensemble average is different from that of a single realization in Figs. 5.11 and 5.12. As  $L$  is increased, coherent circulations become stronger so that the difference between two individual realization, i.e.,  $\text{RMSP}(u)$ , becomes smaller compared with  $\text{RMSC}(u)$ . Therefore, an ensemble

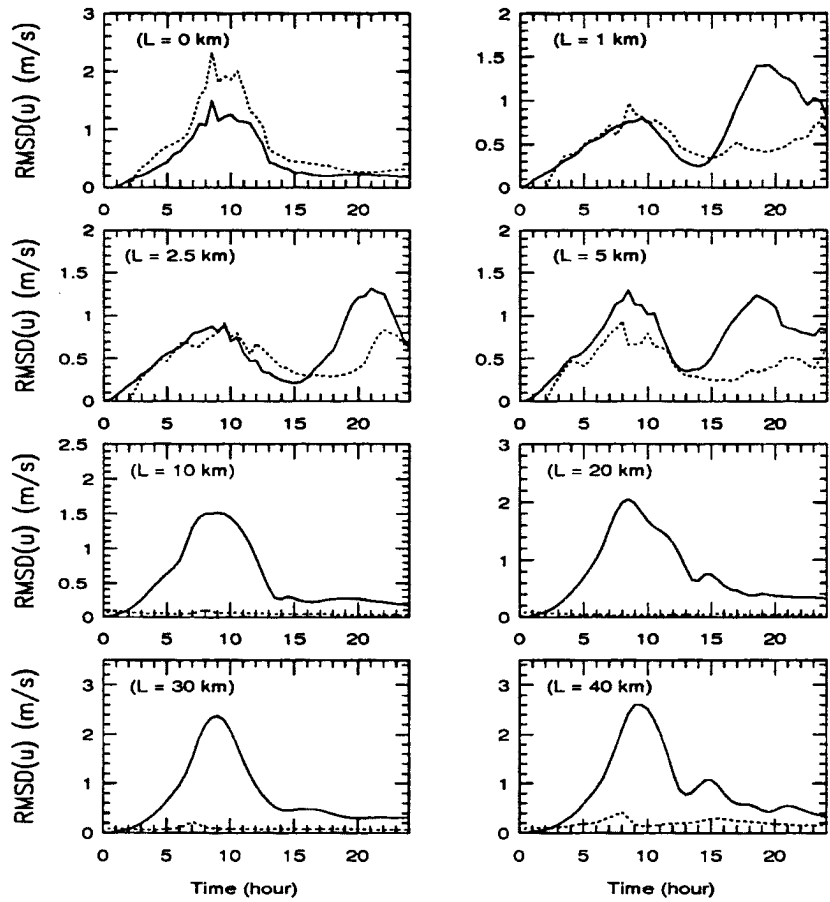


Figure 5.11: Same as Fig. 5.9 but for  $u$ .

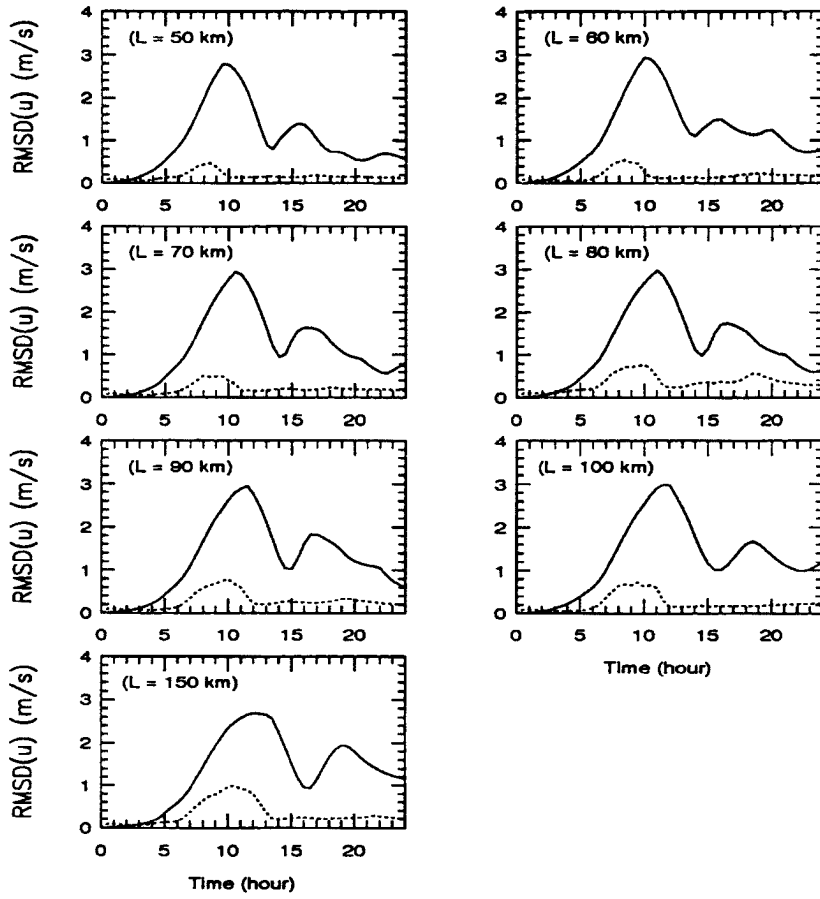


Figure 5.12: Same as Fig. 5.10 but for  $u$ .

average and a realization yield close results for  $L$  equal to or greater than 10 km in the mesoscale simulations with  $\Delta x = 2$  km. Further work is needed to determine the critical value of  $L$  (greater than 10 km) at which an ensemble average and a realization yield close results for fine-resolution simulations. For the  $w$  field, an ensemble average and a realization yield close results for  $L = 10$  to 30 km in mesoscale simulations. For all other cases, the predictability of an ensemble average is different from that of a realization, and further work is needed.

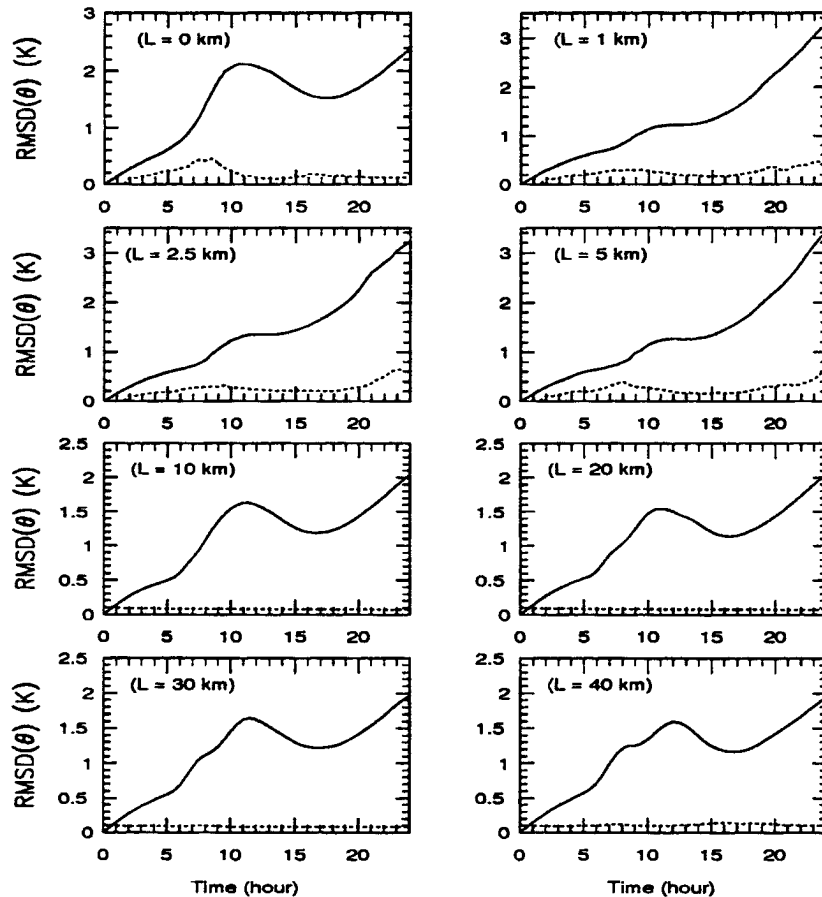


Figure 5.13: Same as Fig. 5.9 but for  $\theta$ .

The transition from organized flow to the situation in which fluxes are dominated by non-coherent turbulent eddies is an important theoretical problem in turbulence study. In practice, the understanding of such a transition will help the parameterization of subgrid processes in large-scale numerical models. As far as we know, our study is the first

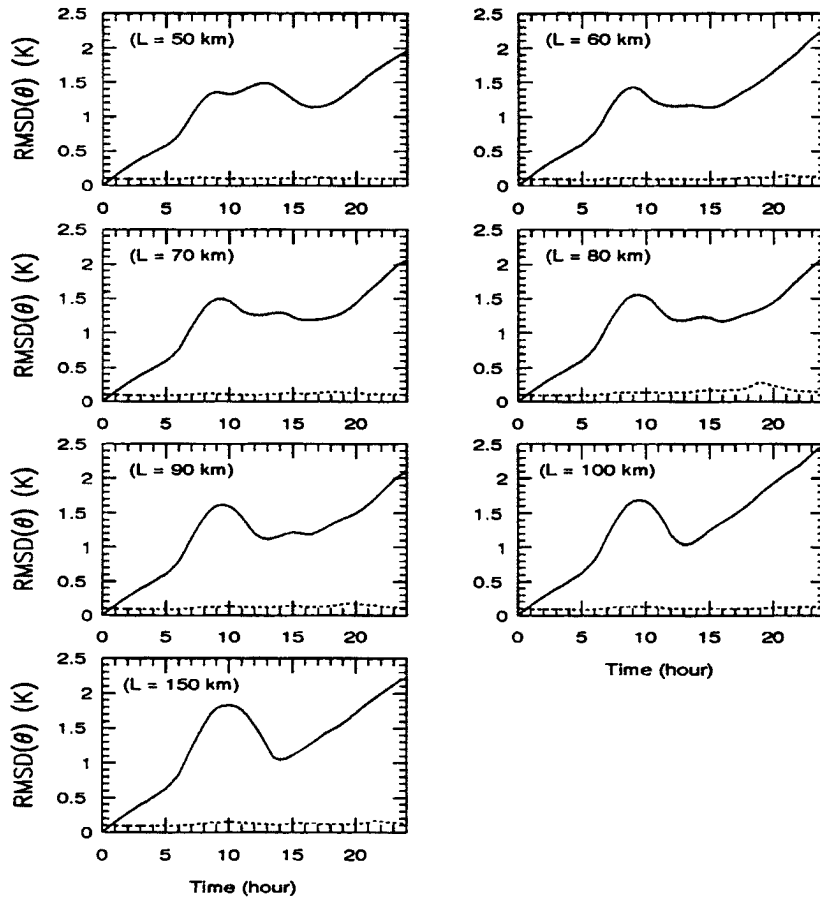


Figure 5.14: Same as Fig. 5.10 but for  $\theta$ .

quantitative evaluation of the transition from predictable flow to unpredictable flow due to the development of coherent circulations.

### 5.5 Three-Dimensional Experiment

The results in the previous two sections are based on 2-D numerical simulations. The difference between 2-D and 3-D simulations has been discussed for different situations in the past (a discussion related to the sea breeze is given in Pielke, 1974b). Extensive 3-D simulations are beyond the scope of this study. Instead, we ran only a pair of 3-D mesoscale simulations (i.e., a control run and a perturbed run) for  $\Delta x = \Delta y = 2$  km and a pair of fine-resolution simulations (i.e., a control run and a perturbed run) for  $\Delta x = \Delta y = 100$  m. The domain is  $50$  (x)  $\times$   $40$  (y)  $\times$   $28$  (z) in the mesoscale run, and is  $60$  (x)  $\times$   $40$  (y)  $\times$   $40$  (z) in the fine-resolution run. For the mesoscale run, the surface is homogeneous in the y-direction, and consists of a strip of water and a strip of land with  $L = 50$  km in the x-direction. Homogeneous land (i.e.,  $L = 0$  km) is used in the fine-resolution run. In order to initiate asymmetry in the y-direction, very small initial perturbations of  $\theta$  are added in the control run. Everything else is the same as for the corresponding 2-D runs as shown in Figs. 5.9 to 5.14.

Natural phenomena are three dimensional. When 2-D simulations are used, the variation in the y-direction is removed, the vorticity tilting and stretching in the y-direction is omitted, and the energy and enstrophy cascade processes are changed. For 2-D turbulence, energy and enstrophy are both conserved; energy cascades toward the low wavenumbers, and enstrophy cascades toward the high wavenumbers. However, for 3-D turbulence, enstrophy is not conserved, and energy cascades toward the high wavenumbers. It is also found in Pielke (1974b) that, even with strong 2-D forcing as in our studies, the circulations are so inherently three-dimensional that the Reynolds stress terms must represent the resolvable as well as the subgrid-scale fluxes. Due to these limitations, even the features in the x-z directions can be distorted in the 2-D simulations compared with 3-D simulations; for instance, the eddies appear to be larger in 2-D simulations with fine resolutions.

Figure 5.15 shows RMSC and RMSP in the 3-D mesoscale simulation for  $\theta$ ,  $u$ , and  $w$  in subdomain A (the whole model domain), subdomain B (below 4 km) and subdomain

C (below 2 km) which is the same as used in Figs. 5.10, 5.12, and 5.14. It is seen that, as in the case of the 2-D runs (which are not shown), RMSC and RMSP are similar in the different subdomains. Comparing Fig. 5.15 with the panels for  $L = 50$  km in Figs. 5.10, 5.12, and 5.14, it is seen that  $\text{RMSC}(\theta)$ ,  $\text{RMSC}(u)$ ,  $\text{RMSC}(w)$ , and  $\text{RMSP}(\theta)$  are qualitatively and quantitatively close between the 2-D and 3-D simulations, and that  $\text{RMSP}(u)$  and  $\text{RMSP}(w)$  in the 3-D simulation are smaller than in the 2-D simulation. Regarding the predictability, very close results are obtained for  $\theta$  and  $u$ , and similar results are obtained for  $w$  between the 3-D and 2-D simulations. It is also shown in Pielke (1974b) that, with 2-D forcing, the 2-D and 3-D models produce identical results when the explicit horizontal diffusion in the 2-D model is increased.

The 3-D fine-resolution simulation with  $\Delta x = \Delta y = 100$  m can be called a large-eddy simulation (LES), since most of the energy-containing eddies are explicitly resolved in the model. However, the 2-D simulation is not called 2-D LES, since the criterion for LES is not satisfied. Instead, we only refer to such 2-D simulations as fine-resolution simulations. Figure 5.16 shows RMSC and RMSP in the 3-D LES for  $\theta$ ,  $u$ , and  $w$  in subdomain A (the whole model domain), subdomain B (below 2 km), which is the same as used in Figs. 5.9, 5.11, and 5.13, and subdomain C (below 1 km). Note that the subdomains are different from those in the 3-D mesoscale simulation. It is seen from Fig. 5.16 that, as in the case of the 2-D runs (which are not shown), the ratios of RMSC/RMSP are similar in different subdomains. Comparing Fig. 5.16 with the panels for  $L = 0$  km in Figs. 5.9, 5.11, and 5.13, it is seen that  $\text{RMSC}(\theta)$  and  $\text{RMSP}(\theta)$  are qualitatively and quantitatively close between 2-D and 3-D simulations. It is also found that RMSC and RMSP for  $u$  and  $w$  in the 3-D simulation are smaller than in the 2-D simulation. This means that eddy activities are stronger in the 2-D simulation. Similar results were also reported in Cotton *et al.* (1990). Regarding the predictability, very close results are obtained for  $\theta$ , and similar results are obtained for  $u$  and  $w$  between the 3-D and 2-D simulations. Although important features (such as rolls, e.g., Krettenauer and Schumann, 1991) may occur in the  $y$ -direction in the 3-D LES, and the 2-D simulations are not accurate quantitative representations of the 3-D structure in the boundary layer, it will be shown in the next

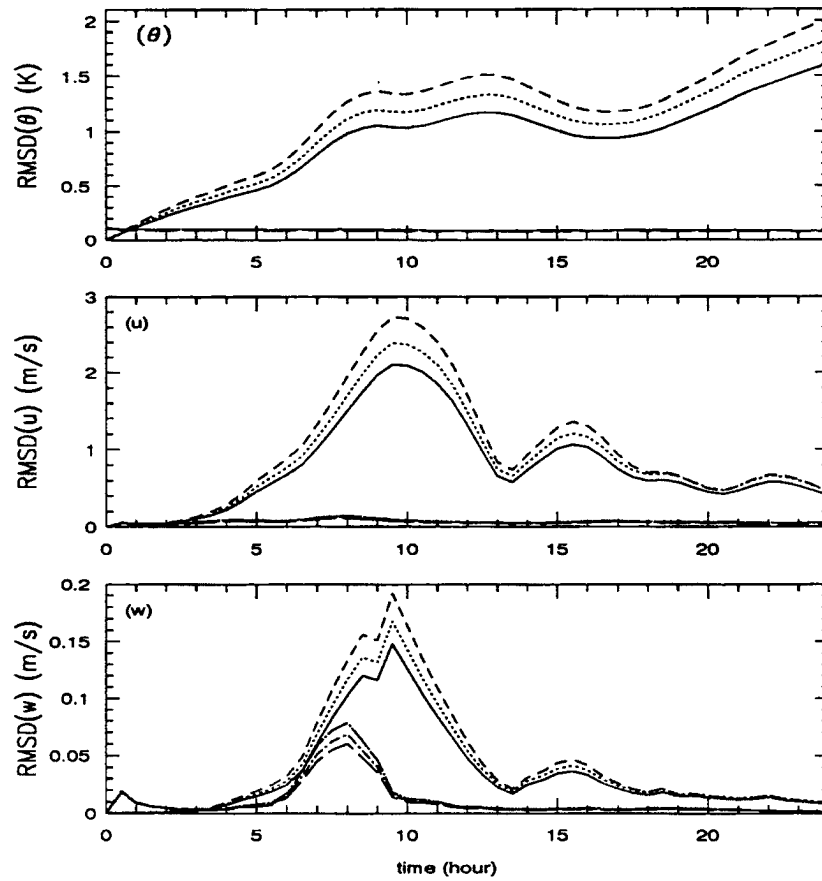


Figure 5.15: RMSC and RMSP of  $\theta$ ,  $u$  and  $w$  in the 3-D mesoscale simulations with  $L = 50$  km. The solid, dotted, and short dashed lines denote RMSC in the subdomains A, B, and C, respectively. The long dashed, short dashed-dotted, and long dashed-dotted lines denote RMSP in the subdomains A, B, and C, respectively.

section that the domain-averaged properties are not substantially changed between the 2-D and 3-D fine-resolution simulations.

Based on the above comparisons, it is reasonable to expect that our results in the previous two sections are also correct for 3-D simulations. Because the 2-D simulations are much cheaper than 3-D simulations, our comparison of 2-D and 3-D runs suggests that 2-D simulations can be widely used in predictability studies when the surface forcing is homogeneous in the y-direction. When surface characteristics are variable in the y-direction, however, only 3-D simulations can be used.

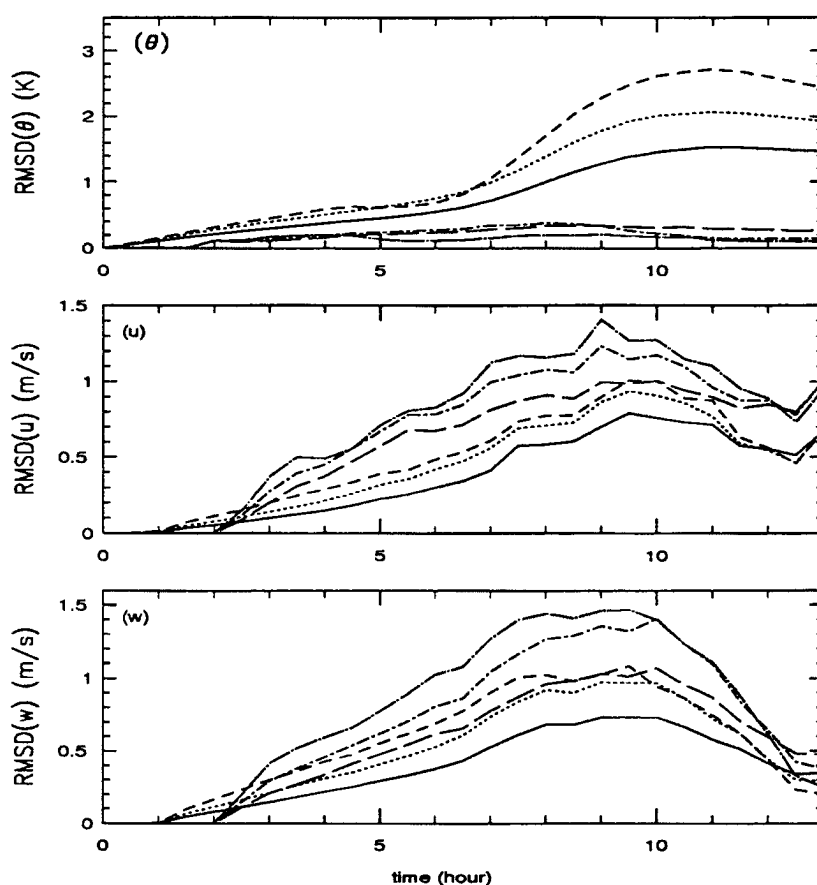


Figure 5.16: Same as Fig. 5.15 but for the 3-dimensional large-eddy simulation with  $L = 0$  km.

## 5.6 Further Analysis of Model Output

### 5.6.1 Analysis tools

In the previous sections, RMSC and RMSP are computed based on quantities at grid points. A related problem is to study the influence of initial perturbations on the domain-averaged quantities. This method is applied to output from fine-resolution simulations ( $L = 0$  to 5 km). Such a method is also used in Pielke *et al.* (1992a) to evaluate the nonlinear influence of mesoscale landuse on weather and climate, based on the variation of subgrid and mesoscale heat fluxes as a function of  $L$ .

Another quantity to be computed is the spatial and temporal autocorrelation coefficients. The autocorrelation measures the persistence of a wave within the entire duration of a temporal or spatial series. This quantity, denoted as  $R$ , is computed for cases of  $L = 0$  to 150 km.

Another quantity related to the autocorrelation is the power spectrum, denoted as  $E$ .  $E(f)$  represents the portion of variance explained by waves of frequency  $f$  for time series or of wavenumber  $f$  for spatial series.  $E(f)$  is normalized by the variance so that the sum of  $E(f)$  for  $f = 1/N$  to  $1/2$  is unity where  $N$  represents the total number of data. This quantity is computed for the cases of  $L = 0$  to 150 km. Note that power spectrum analysis does not include any phase information. A new technique that deals with both frequency and phase information is the wavelet representation which has been developed recently, and has been used in different fields (e.g., Strang, 1989 and references therein; Meneveau, 1991 and references therein). We plan to use this technique in the near future.

The fractal dimension and Lyapunov exponents are important quantities in chaos theory developed in the past thirty years (e.g., Zeng *et al.*, 1992a,b; also see Chap. 2). The fractal dimensions are evaluated in this study, and the Lyapunov exponents will be discussed very briefly. (For the convenience of publication of this chapter, the rest of this subsection is a repetition of the material in Chap. 2.)

The significance of the fractal dimension in chaos is discussed in Zeng *et al.* (1992a) in detail. Related to the predictability problems, the estimation of the fractal dimension from the whole model output provides some information about the statistics of atmospheric variability. Besides, if a low-dimensional attractor can be obtained under certain

conditions, a relatively simple model may be constructed for prediction problems. This is a very active area in chaos research (e.g., Abarbanel *et al.*, 1990).

The computation of the fractal dimensions is carried out in a phase space. For a system with known ordinary differential equations (ODEs) or difference equations, all dependent variables constitute a phase space, i.e., an Euclidean space whose coordinates are these variables. Each point in phase space represents a possible instantaneous state of the system. A state, which is governed by the governing equations, is represented by a particle traveling along a trajectory in phase space. For a system with known partial differential equations (PDEs), the system can usually be studied by discretizing the PDEs, and all of the dependent variables at all grid points constitute a phase space, which is an approximation to the original infinite-dimensional phase space. For such a system (e.g., the atmosphere), an additional difficulty is that the initial values of the system may be unknown or lacking. However, a time series of one or more of the variables of a complex system may be available, and the attractor of the system needs to be reconstructed in a phase space. Different reconstruction techniques have been discussed in detail in Zeng *et al.* (1992b). In this chapter, the phase space will be constructed by using dependent variables at grid points, and by the time-delay method (Zeng *et al.*, 1992b).

In a  $k$ -dimensional phase space reconstructed from model output, the correlation dimension, which is different from (but usually close to) other definitions of the fractal dimension, is given by (Grassberger and Procaccia, 1983a)

$$C(r) = \lim_{N \rightarrow \infty} \frac{1}{N^2} \sum_{i,j=1}^N H(r - \|\vec{x}_i - \vec{x}_j\|) , \quad (5.8)$$

where the vector  $\vec{x}_i$  is a trajectory point,  $N$  is the total number of trajectory points,  $H$  is the Heaviside function defined by  $H(y) = 1$  for positive  $y$ , and  $H(y) = 0$  otherwise, and the usual Euclidean norm is used. In other words,  $C(r)$  is the cumulative histogram for the number of pairs of trajectory points whose distance is less than  $r$  in  $k$ -dimensional phase space.

The relationship between  $C(r)$  and  $r$  varies with  $r$ . When  $r$  is very small, there are insufficient statistics, and the influence of noise inherent in the system or contributed

by measurements is important; whereas, for  $r$  too large, the information is affected by nonlinearity, and the slope of the curve of  $\ln C(r)$  versus  $\ln r$  is smaller than that for intermediate  $r$ . However, there exists an intermediate range of  $r$  in which this slope is almost constant; i.e.,  $C(r)$  depends upon  $r$  as

$$C(r) \sim r^\nu . \quad (5.9)$$

For each embedding dimension  $k$ , this exponent  $\nu$  can be obtained from the slope of the linear part of a plot of  $\ln C(r)$  versus  $\ln r$ . If  $\nu$  approaches a value independent of  $k$  as  $k \rightarrow \infty$  (usually  $k > 2\nu$  is sufficient), this value is defined as the correlation dimension  $\nu_s$ . When a high-dimensional phase space is used, which is constructed by variables at different grid points,  $\nu_s$  can be obtained without increasing the embedding dimension further. In this study, the correlation dimension is computed from the entire model output and from the output at several grid points for cases of  $L = 0$  to 150 km.

### 5.6.2 Results of further analysis

The horizontally averaged statistical quantities from our 3-D fine-resolution simulations are compared first with those from other 3-D LESs. Figure 5.17 shows the horizontally averaged quantities as a function of time in the 3-D fine-resolution simulation for the homogeneous case (i.e.,  $L = 0$ ). It is seen that, at the stage of the fully-developed turbulence (e.g.,  $t = 9$  hours), the horizontally averaged quantities are characteristic of those from laboratory and other LES studies (Deardorff and Willis, 1985; Mason, 1989; Moeng and Wyngaard, 1988; Hadfield *et al.*, 1991,1992; Krettenauer and Schumann, 1991; Walko *et al.*, 1992). The negative skewness near the surface is also present in Fig. 5.17f, as in other LES studies. Some possible reasons are discussed in Mason (1989) and Nieuwstadt *et al.* (1991). However, most of the previous LES studies concentrated on the steady-state behavior rather than the predictability of the boundary layer flow.

Figure 5.18 shows the horizontally averaged quantities as a function of time in the 2-D fine-resolution simulation for the homogeneous case (i.e.,  $L = 0$ ). It is seen that the horizontally averaged potential temperature is close to that in the 3-D LES (Fig. 5.17).

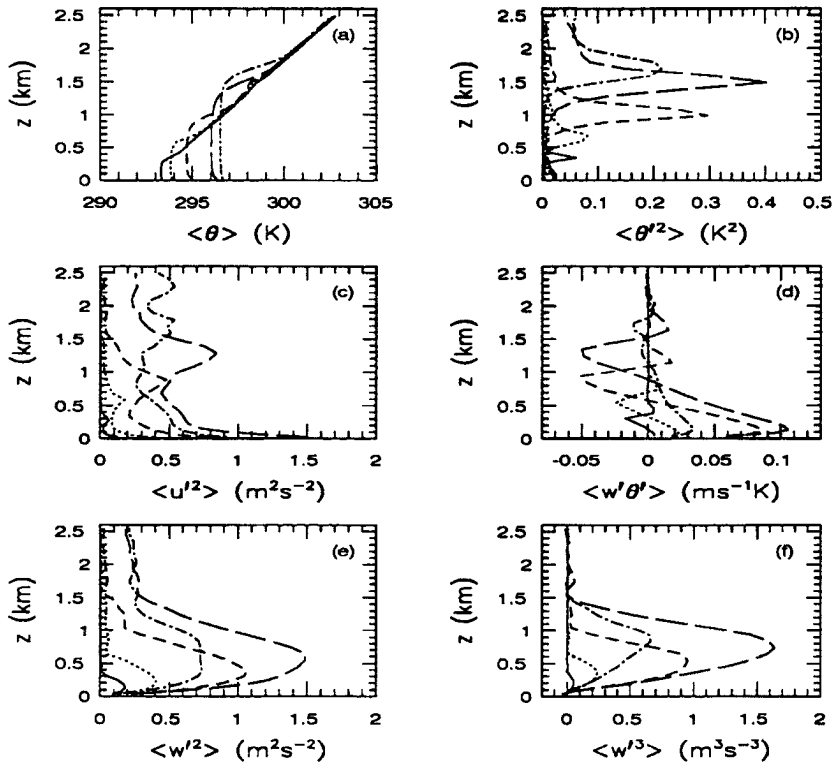


Figure 5.17: The horizontally averaged quantities for the horizontally homogeneous case ( $L = 0$  km) from 3-D large-eddy simulation. The subgrid contributions are excluded. The solid, dotted, short dashed, long dashed, and dotted-dashed lines denote the time  $t = 3, 5, 7, 9,$  and  $11$  hours, respectively.

Other quantities in Fig. 5.18 are similar to those in Fig. 5.17 qualitatively, and are larger than those in Fig. 5.17 quantitatively. This is another indication that eddy activities are stronger in the 2-D simulation. Note that normalization is not used in Figs. 5.17 and 5.18. The negative skewness near the surface is also present in Fig. 5.18f, as in LES studies.

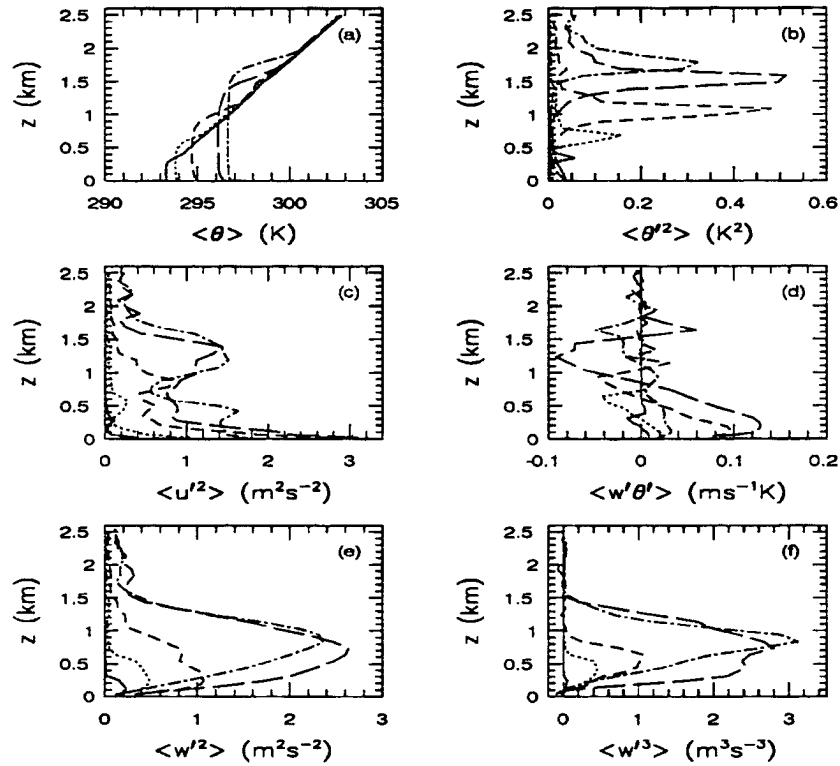


Figure 5.18: Same as Fig. 5.17 except from 2-D fine-resolution simulation.

Figures 5.19 and 5.20 show the influence of surface inhomogeneities on the prediction of the horizontally averaged quantities at time  $t = 9$  hours for the cases of  $L = 1$  and  $5$  km. It is seen from both Figures that the horizontally averaged potential temperature, i.e.,  $\langle \theta \rangle$ , is very close between the control and perturbed runs, while other horizontally averaged quantities are somewhat different. The profiles of  $\langle \theta \rangle$  are expected, since potential temperature is well mixed. It is also found that the horizontally averaged quantities, except  $\langle \theta \rangle$ , are also somewhat different between the control and perturbed 3-D

LESs. This is consistent with the conclusion in previous LES studies (e.g., Walko *et al.*, 1992) that long-time averages are needed to obtain stationary statistics. When temporal and horizontal averages are used, quantities are insensitive to the initial perturbations. However, since no steady state is expected with the surface forcing, which varies with time, long-time averages may not be appropriate in our cases. Therefore, the small discrepancies between the control and perturbed runs simply reflect the temporal fluctuation of a spatially-averaged variable in a spatial and temporal average. By comparing Figs. 5.19 and 5.20 with the corresponding Figure for the homogeneous case (i.e.,  $L = 0$  km) which is not shown, it is found that the discrepancies between the control and perturbed simulations in Figs. 5.19 and 5.20 are smaller than for the homogeneous case. This may imply that a smaller number of realizations are needed for an ensemble average when surface forcing is present. This is consistent with the discussion about the ensemble average and individual realizations in Section 5.4. Obviously, further studies are needed to clarify this important issue.

The domain for the case of  $L = 1$  or  $5$  km is covered half by water and half by soil. If we regard the model domain as a grid box of large-scale models, the difference of the corresponding variables between Fig. 5.19 and 5.20 indicates the errors due to subgrid variability. This is related to the subgrid parameterizations in large-scale models. It is seen that the major errors caused by subgrid variability are the variances of  $\theta'$  and  $u'$  near the surface, and the peak of the skewness. It is also interesting to note that the skewness in Fig. 5.20 (i.e.,  $L = 5$  km) is very nearly zero, rather than negative as in the cases of  $L = 0$  km (Fig. 5.18) and  $1$  km (Fig. 5.19). The reason is unclear at present.

At time  $t = 3, 5, 7, 9,$  and  $11$  hours and at different vertical levels, the autocorrelations for  $\theta$ ,  $u$ , and  $w$  are computed for the cases  $L = 0$  to  $5$  km. It is found from these computations that the autocorrelation for  $w$  [i.e.,  $R_w(r)$ ] drops to zero rapidly and then oscillates around zero in all cases with the increase of the lag  $r$ . In contrast,  $R_u$  and  $R_\theta$  decrease more slowly with the lag  $r$ . It is also found that, with the increase of  $L$  (i.e., the increase of the spatial scale of the surface forcing),  $R_u$  and  $R_\theta$  decrease more slowly with the lag  $r$ . This simply reflects the increase of the strength of coherent circulations with the increase of  $L$ .

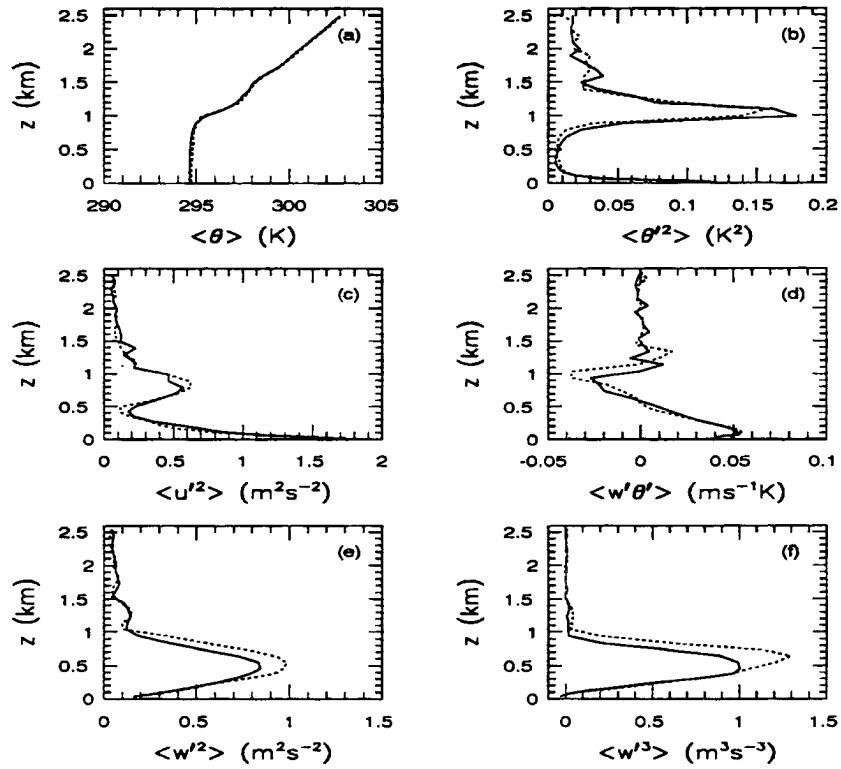


Figure 5.19: The horizontally averaged quantities at time  $t = 9$  hours for the case of  $L = 1$  km. The subgrid contributions are excluded. The solid and dotted lines denote the control and perturbed runs, respectively.

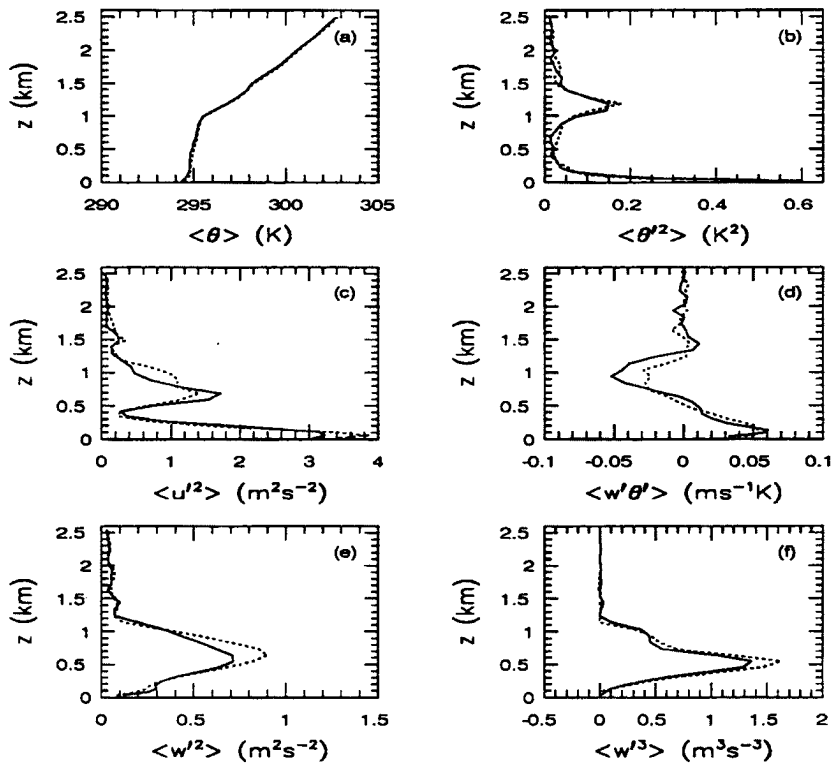


Figure 5.20: The same as Fig. 5.19, except for the case of  $L = 5$  km.

We also compute the autocorrelation coefficients at different times and different vertical levels for the cases of  $L = 10$  to  $150$  km. Some of the results are presented in Fig. 5.21. For the surface of alternating water and soil with the width of each strip (of water or soil) being  $L$ , the wavelength of the thermally-induced circulations is  $2L$  or  $L\Delta x$  (since  $\Delta x = 2$  km). The peak of each curves in Fig. 5.21 reflects this wavelength; for instance, for the case of  $L = 10$  km (denoted by the solid line), the peaks are at lag = 10, 20, ...,  $70\Delta x$ . This means that the boundary layer flow is strongly modulated by the surface inhomogeneities.

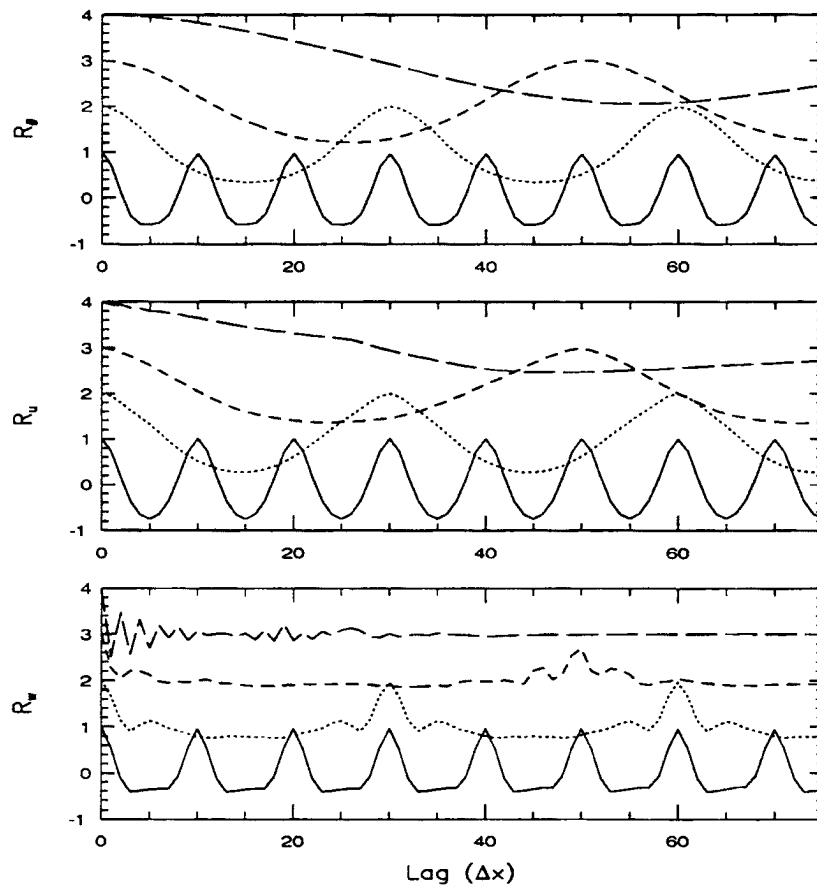


Figure 5.21: The autocorrelation coefficients of  $\theta$ ,  $u$ , and  $w$  at time  $t = 9$  hours and at the fourth vertical level ( $z = 112$  m for  $\theta$  and  $u$ , and  $z = 139$  m for  $w$ ). The solid, dotted, short dashed, and long dashed lines denote the cases of  $L = 10, 30, 50,$  and  $100$  km, respectively. The curves from bottom to top in each panel are separated by increments of 1.0.

The horizontally averaged autocorrelation coefficients of  $\theta$ ,  $u$ , and  $w$  at different vertical levels are also computed as a function of time. It is found from these computations that the autocorrelation for  $\theta$ ,  $u$ , and  $w$  decreases slowly for the cases of  $L = 10$  to  $150$  km. In the cases of  $L = 0$  to  $5$  km, the autocorrelation for  $\theta$ , i.e.,  $R_\theta(t)$ , also decreases very slowly. For instance, for the time lag of 2 hours,  $R_\theta$  is still greater than 0.5 for the case of  $L = 5$  km. This long persistence illustrates the longer predictability of  $\theta$  field, as found in Section 5.4 by computing the signal/noise ratios. In contrast,  $R_w(t)$  drops to zero rapidly for the cases of  $L = 0$  to  $5$  km, which means that the component of small-scale non-coherent motions is more important, as mentioned in Section 5.4. It is also found that  $R_u(t)$  decreases more slowly in the case of  $L = 5$  km than in the homogeneous case. This is consistent with the fact that the  $u$  field is more predictable for  $L = 5$  km than for  $L = 0$  km, as shown in Fig. 5.11.

Figure 5.22 show the autocorrelations of the error fields, i.e., the differences of  $\theta$ ,  $u$ , and  $w$  between the control and perturbed runs. It is seen that the error fields do not show the surface modulation, and are influenced mainly by perturbations of short wavelengths.

The power spectra are computed at different time and different vertical levels for the cases of  $L = 0$  to  $5$  km. Some of the results are shown in Fig. 5.23. It is seen that, for the homogeneous case, i.e., the panels of (a), (c), and (e) in Fig. 5.23, there are a few important wavenumbers at  $t = 3$  hours. With the evolution of the boundary layer structures and eddies with time, only one or two wavenumbers dominates the spectra. Furthermore, as the integration time increases from  $t = 3$  hours to 11 hours, the dominant wavenumber for the  $u$  field decreases, and when  $t = 11$  hours, the dominant wavenumber is 2; in other words, the dominant wavelength of the eddies for the  $u$  field is 5 km. Note that the eddy activities have been found to be stronger in the 2-D fine-resolution simulation in Section 5.5. The phenomena, that eddies are larger in size and eddy activities are stronger in the 2-D fine-resolution simulation, are also observed in Cotton *et al.* (1990). The reason is that the energy and enstrophy cascade processes are changed and the vorticity cannot stretch in the  $y$ -direction, as mentioned in Section 5.5. In contrast to the homogeneous case, the surface inhomogeneities and forcing will modulate the eddies in the boundary layer. It is

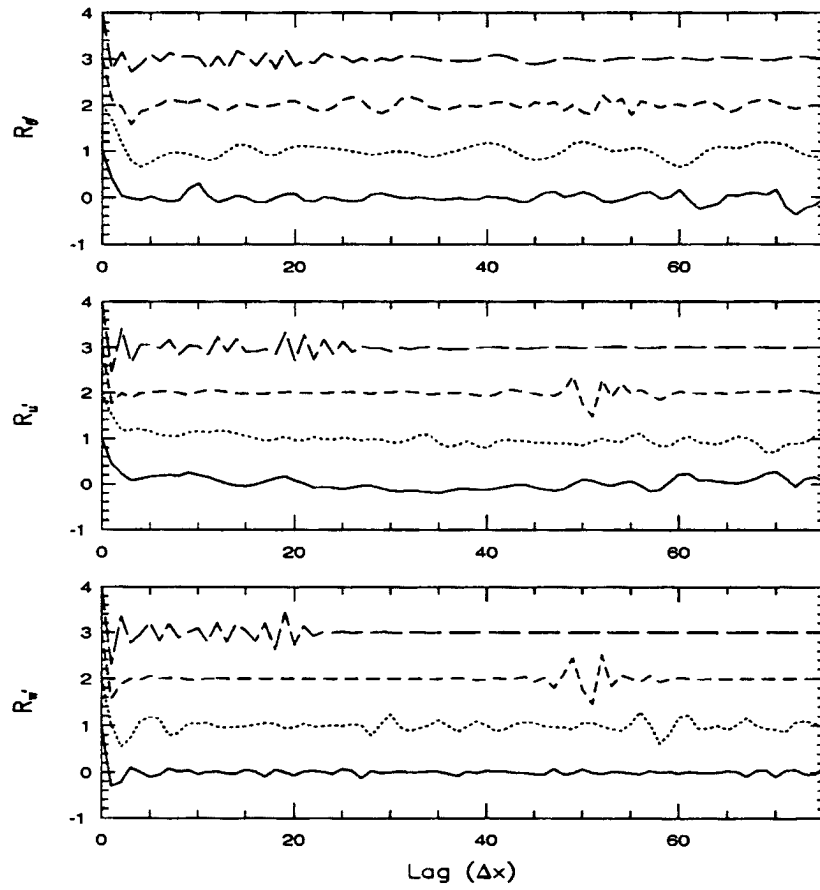


Figure 5.22: Same as Fig. 5.21 except for the error fields between the control and perturbed simulations.

seen from the panels of (b), (d), and (f) in Fig. 5.23 that the dominant wavelength is 2 km at any time due to the width of strip of land ( $L$ ) of 1 km. For the cases of  $L = 2.5$  and 5 km, the dominant wavelengths are 5 and 10 km, respectively. Therefore, although the 2-D fine-resolution model produces larger eddies than in LES for the homogeneous case, the 2-D model does not have this problem in the presence of significant surface inhomogeneities (e.g.,  $L = 1$  km). For the cases of  $L = 10$  to 150 km, the dominant wavelength is also found to be  $2L$ .

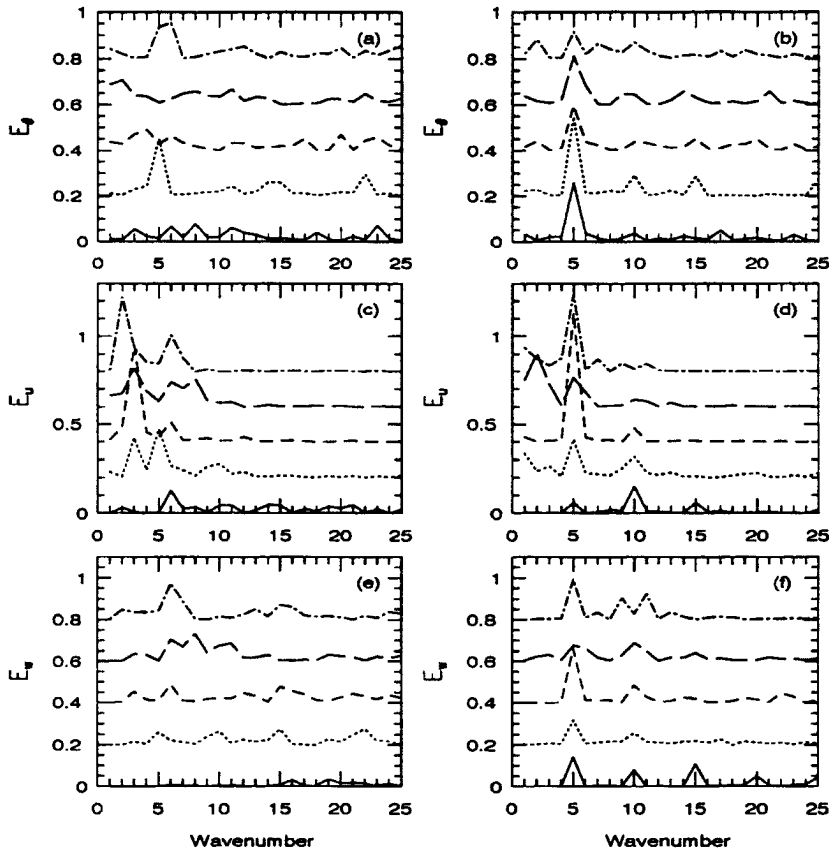


Figure 5.23: The power spectra of  $\theta$  and  $u$  at the height  $z = 108$  m, and  $w$  at the height  $z = 132$  m for the cases of  $L = 0$  and 1 km. The corresponding wavelength with the wavenumber  $n$  is  $10/n$  (km). The panels of (a), (c), and (e) represent the homogeneous case; the panels of (b), (d), and (f) represent the case of  $L = 1$  km. The solid, dotted, short dashed, long dashed, and dotted-dashed lines from bottom to top in each panel denote the time  $t = 3, 5, 7, 9,$  and  $11$  hours, respectively, and are separated by increments of 0.2 for clarity.

The power spectra of  $\theta$ ,  $u$ , and  $w$  are also computed as a function of frequency for the first 12 hours at different vertical levels for the different cases. It is found that the spectra for  $w$  is flat between low and high frequencies. This means that  $w$  is controlled by components of both coherent circulations and chaotic motions, as mentioned before. However, the spectra for  $\theta$  have peaks at low frequency, and decrease with an increase of the frequency. This means that the chaotic components are small for  $\theta$  field. The spectra for  $u$  also have peaks at low frequency, but decrease more slowly with the increase of the frequency than the spectra for  $\theta$ . These results mean that  $\theta$  is more predictable than  $u$ , and  $u$  is more predictable than  $w$ , which are consistent with our results in Sections 5.3 and 5.4.

In order to further understand the results for the  $u$  field in Section 5.4, the power spectra for the  $u$  field in the control run and the error field of  $u$  between the control and perturbed simulations are shown in Fig. 5.24. It is found that both the  $u$  field and the error field of  $u$  are influenced mainly by the low wavenumber components for the homogeneous case. In other words, the coherent circulations are not strong, and the error field of  $u$  is mainly caused by the change of locations of coherent circulations. Therefore, the signal/noise ratio of  $u$  is smaller than unity in the homogeneous case. When  $L = 5$  km or 30 km, the  $u$  field shows strong coherent circulations, and the error field of  $u$  is influenced by components of both high and low wavenumbers (i.e., by components of both coherent circulations and chaotic motions). Therefore, the  $u$  field is predictable when  $L$  is equal to or greater than 5 km.

Figure 5.25 shows the power spectra for the  $w$  field in the control run and the error field of  $w$ . It is found that, like the error field of  $u$ , the error field of  $w$  is influenced mainly by the change of locations of coherent circulations for the homogeneous case. Therefore, the signal/noise ratio of  $w$  is smaller than unity in the homogeneous case. For  $L = 30$  km, the  $w$  field shows strong circulations, and the error field of  $w$  is influenced mainly by the component of chaotic motions so that the  $w$  field is predictable. For  $L = 100$  km, because the region of substantial horizontal differential heating covers only a small portion of the total domain, as discussed in Section 5.4, both the  $w$  field and the error field of  $w$  are

determined mainly by components of short wavelengths. Therefore, the  $w$  field becomes unpredictable in our simulations. Again, further study is needed to clarify this result.

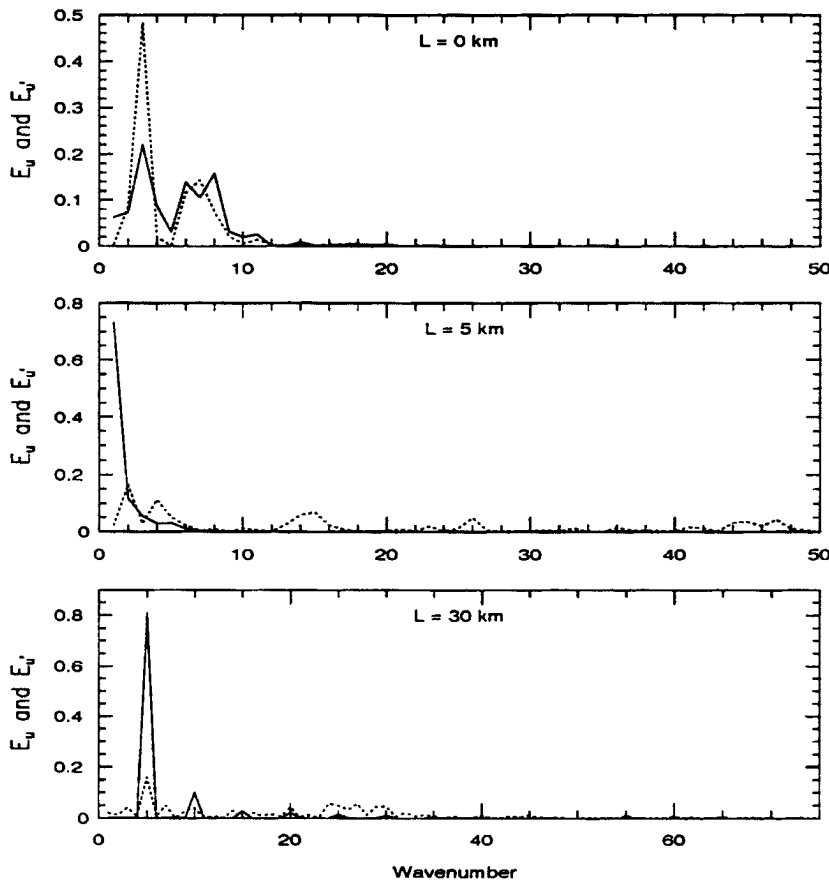


Figure 5.24: The power spectra of  $u$ , denoted by the solid line, and of the error field of  $u$ , denoted by the dotted line, at the height  $z = 108$  m for the cases of  $L = 0$  and 5 km, and at  $z = 112$  m for  $L = 30$  km at time  $t = 9$  hours. The corresponding wavelength with the wavenumber  $n$  is  $10/n$  (km) for  $L = 0$  and 5 km, and is  $300/n$  (km) for  $L = 30$  km.

Figure 5.26 compares the spectra in the 3-D LES and those in the 2-D high-resolution simulation for the homogeneous case. For the 3-D LES, the spectra are computed in the  $x$ -direction and are then averaged along the  $y$ -direction. It is seen that the spectra are different between the 2-D and 3-D simulations, as mentioned in Section 5.5. For the 3-D LES, the  $-5/3$  range in wavelength is 300 to 1500 m for  $\theta$ , 1500 to 3000 m for  $u$ , and 240 to 1500 m for  $w$ . When the wavelength is smaller than 1500 m, the spectrum for  $u$  decreases faster with wavenumber than for the  $-5/3$  power law. The sharp drop in the spectra at

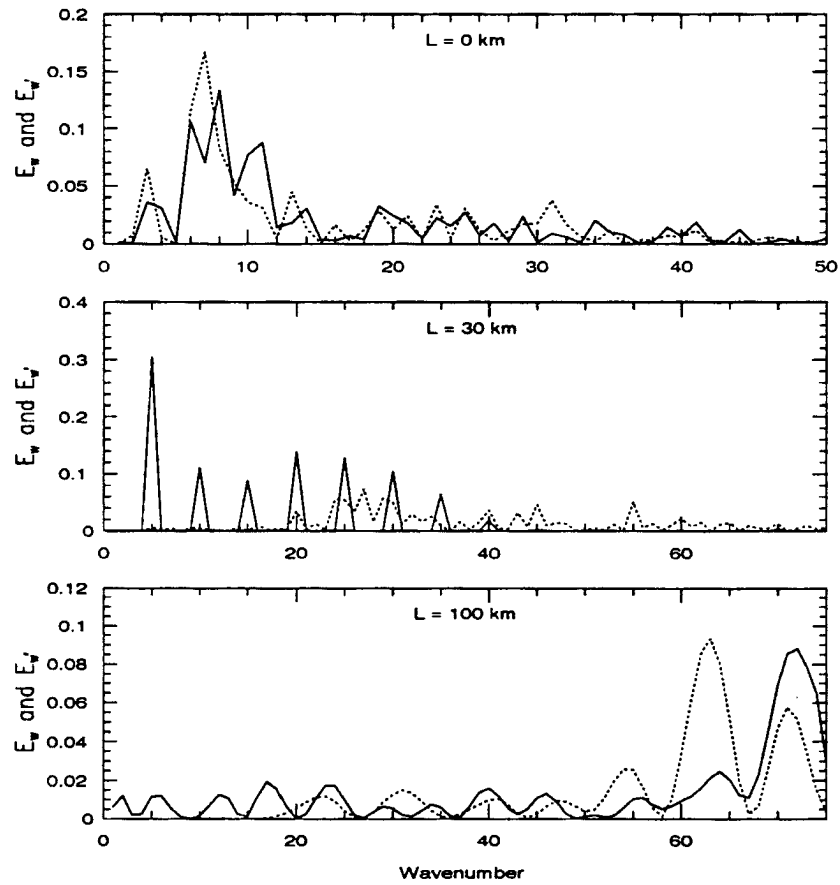


Figure 5.25: The power spectra of  $w$ , denoted by the solid line, and of the error field of  $w$ , denoted by the dotted line, at the height  $z = 132$  m for the cases of  $L = 0$  km, and at  $z = 139$  m for  $L = 30$  and  $100$  km at time  $t = 9$  hours. The corresponding wavelength with the wavenumber  $n$  is  $10/n$  (km) for  $L = 0$  km, and is  $300/n$  (km) for  $L = 30$  and  $100$  km.

high wavenumbers can be explained by the fact that averaging or filtering is used in LES, as discussed in Moeng and Wyngaard (1988). For the 2-D simulation, the spectrum of  $\theta$  is close to the -3 power law at high wavenumbers; the spectrum of  $u$  is close to the -3 power law when the wavelength is less than 3.3 km; and the spectrum of  $w$  decreases more slowly with wavenumber than for the -3 range.

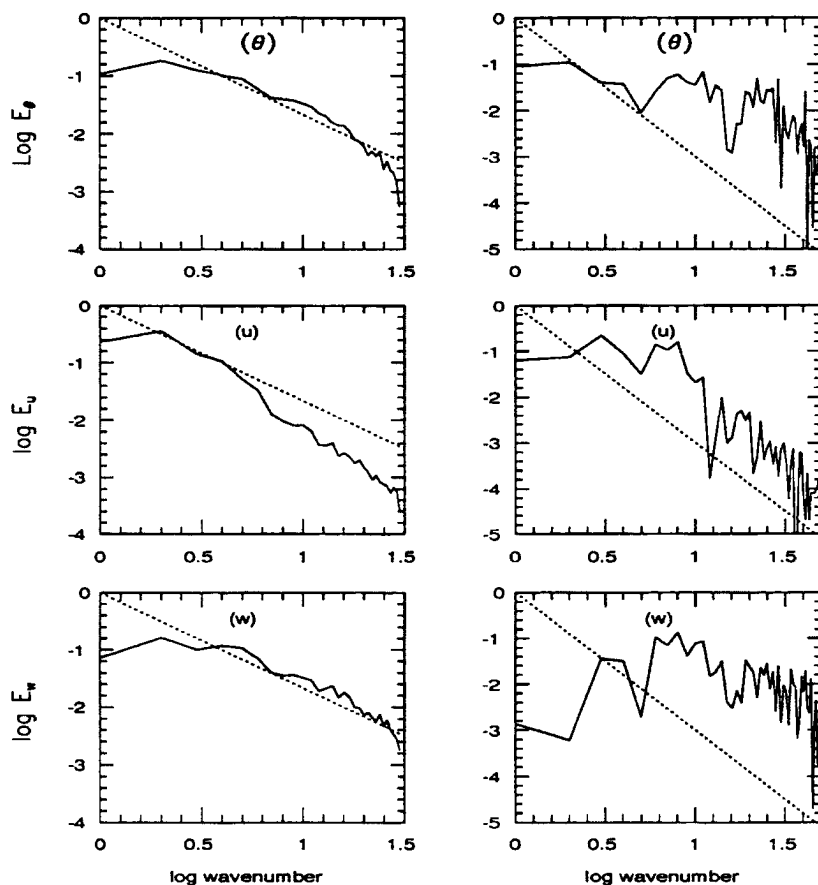


Figure 5.26: The power spectra (denoted by the solid lines) of  $\theta$  and  $u$  at the height  $z = 108$  m, and  $w$  at the height  $z = 132$  m for the homogeneous case (i.e.,  $L = 0$  km) at time  $t = 9$  hours. The left panels represent the spectra for the 3-D LES, in which the dotted line denotes the -5/3 power law and the corresponding wavelength with the wavenumber  $n$  is  $6/n$  (km). The right panels represent the spectra for the 2-D high-resolution simulation, in which the dotted line denotes the -3 power law and the corresponding wavelength with the wavenumber  $n$  is  $10/n$  (km).

We next take all grid points to construct a 4000-dimensional phase space for the cases of  $L = 0$  to 5 km. Results for  $\theta$ ,  $u$ , and  $w$  are stored every half an hour. Therefore, for

each variable, there are 48 trajectory points in this phase space for 24 hours of integration. Note that the phase space is only a projection of the true phase space which consists of all prognostic variables ( $\theta$ ,  $u$ ,  $w$ , and the turbulent kinetic energy) at all grid points. Although the dimension of the phase space is fixed for these cases, saturated correlation  $\nu_s$  can be obtained without further increasing the embedding dimension, since this phase space is large enough. Figure 5.27 shows the cumulative histograms for the cases of  $L = 0$  to 5 km. It is seen that the correlation dimension  $\nu_s$  is similar for  $\theta$  for different cases. For  $(\ln r)$  from 2 to 2.5 (or the potential temperature difference defined by the Euclidean norm from 7.4 to 12.2 K), the correlation dimension is about 3.5. For  $(\ln r)$  greater than 3,  $\nu_s$  is about 1.4. For the  $u$ -component,  $\nu_s$  is similar for the cases of  $L = 1, 2.5,$  and 5 km, but different between these cases and the homogeneous case.  $\nu_s$  is about 3.2 for the intermediate range for  $L = 1, 2.5,$  and 5 km, but difficult to estimate for the homogeneous case. For the  $w$ -component,  $\nu_s$  is about 4.7 in the intermediate range for the cases of  $L = 1, 2.5,$  and 5 km, but difficult to estimate for the homogeneous case in the intermediate range. For  $(\ln r)$  greater than 2.5 (or the  $w$  difference defined by the Euclidean norm greater than 12.2 m/s),  $\nu_s$  is less than unity for all cases.

By comparing  $\nu_s$  for different variables, it is seen that  $\nu_s$  is smallest for  $\theta$ , and largest for  $w$  in the intermediate range. This is consistent with the predictability of these variables:  $\theta$  is most predictable and  $w$  is least predictable. However, this consistency need not be true in general. The fractal dimensions are different for different variables, because different variables are governed by different detailed dynamics. Low-dimensional attractors are found in the intermediate range for  $\theta$  in all cases, and for  $u$  and  $w$  in all cases except the homogeneous case. (The high correlation dimensions of  $u$  and  $w$  in the intermediate range for the homogeneous case, which are difficult to estimate, imply that the turbulent structures in the boundary layer are of a larger degree of freedoms and hence are difficult to predict.) The low fractal dimensions between 3 and 5 imply that the motion in a very high dimensional space (which approximately represents the original infinite-dimensional space of the physical system) is confined to the vicinity of a low-dimensional manifold. However, the correlation-dimension analysis gives us no way of constructing this manifold.

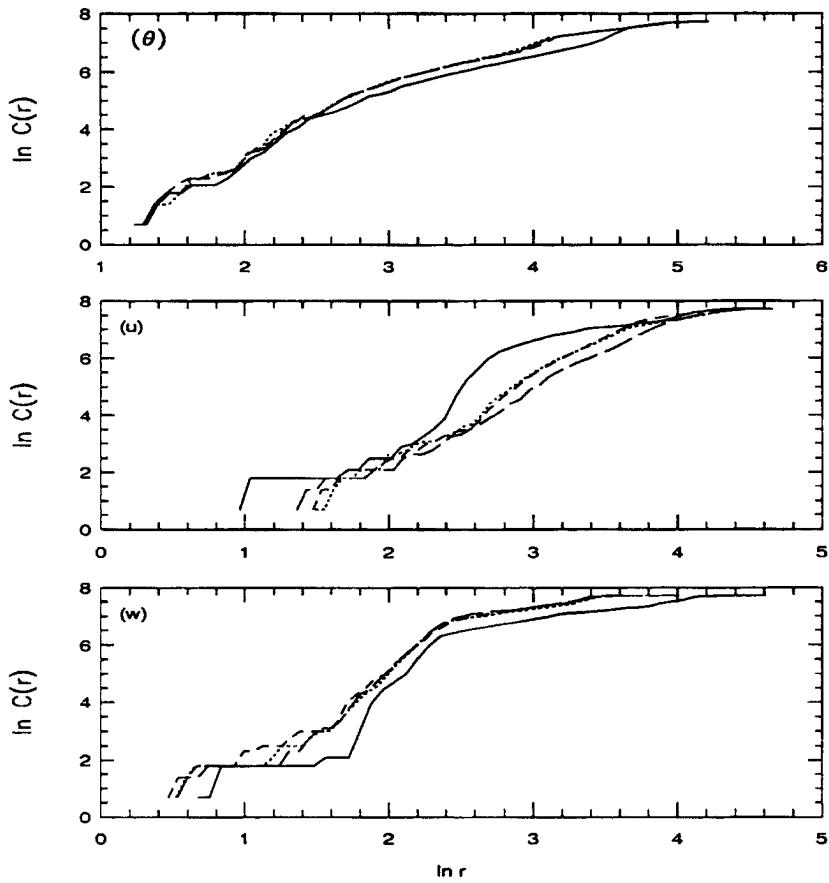


Figure 5.27: Correlation dimension plot for  $\theta$ ,  $u$ , and  $w$ , using the data at all grid points. The solid, dotted, short dashed, and long dashed lines denote the cases of  $L = 0, 1, 2.5,$  and  $5$  km, respectively. Note that the term  $1/N^2$  in Eq. (5.8) is not multiplied.

This is a well-known frustration of the correlation dimension analysis. For our cases, we speculate that the three dimensions of the low-dimensional attractors are associated with the magnitude of the surface heating, the surface modulations due to surface inhomogeneities, and the thermal stratification in the boundary layer. Another dimension may be associated with the Coriolis force or the horizontal diffusion. The selection of these four features is based on the fact that, from linear theory (Rotunno, 1983; Dalu and Pielke, 1989) and from our own experiences, that these parameters basically determine the surface thermally-induced circulations under the condition of calm wind. We also speculate that the diurnal cycle is responsible for the correlation dimension being less than unity for the vertical velocity at large  $\ln r$ .

Low dimensional attractors are also obtained for the cases using  $\Delta x = 2$  km. Some of the results are given in Fig. 5.28. Discussions similar to those in the previous paragraph can be given. We also use data stored every 30 seconds at 66 grid points (11 points at each of six selected levels in the boundary layer) to compute the correlation dimension. Only the data in the first 12 hours are used, so that there are 1440 trajectory points in the 66-dimensional phase space. The results for  $L = 10, 30, 50,$  and  $100$  km are given in Fig. 5.29. As in Fig. 5.28, the correlation dimensions are also low (less than 4). Results similar to those in Fig. 5.29 are also obtained for the cases of  $L = 0$  to  $5$  km. Furthermore, we compute the correlation dimensions at different vertical levels in a 11-dimensional phase space for all cases. Low-dimensional attractors are obtained for all cases based on the intermediate range of the curves.

In addition to the above computations, we also compute the correlation dimensions in 3 to 11 dimensional phase space by two methods. The same two methods were used in Essex *et al.* (1987) and were shown to produce similar results. The first method, as used in the above, entails the use of the data from each of 11 grid points at the same vertical level and separated by 500 m in fine-resolution simulations as a separate coordinate. The embedding is done by introducing the data from progressively more grid points as additional coordinates. In this way, the number of trajectory points in the phase space is 1080 for the first 12 hours, since data are stored every 40 seconds for the cases

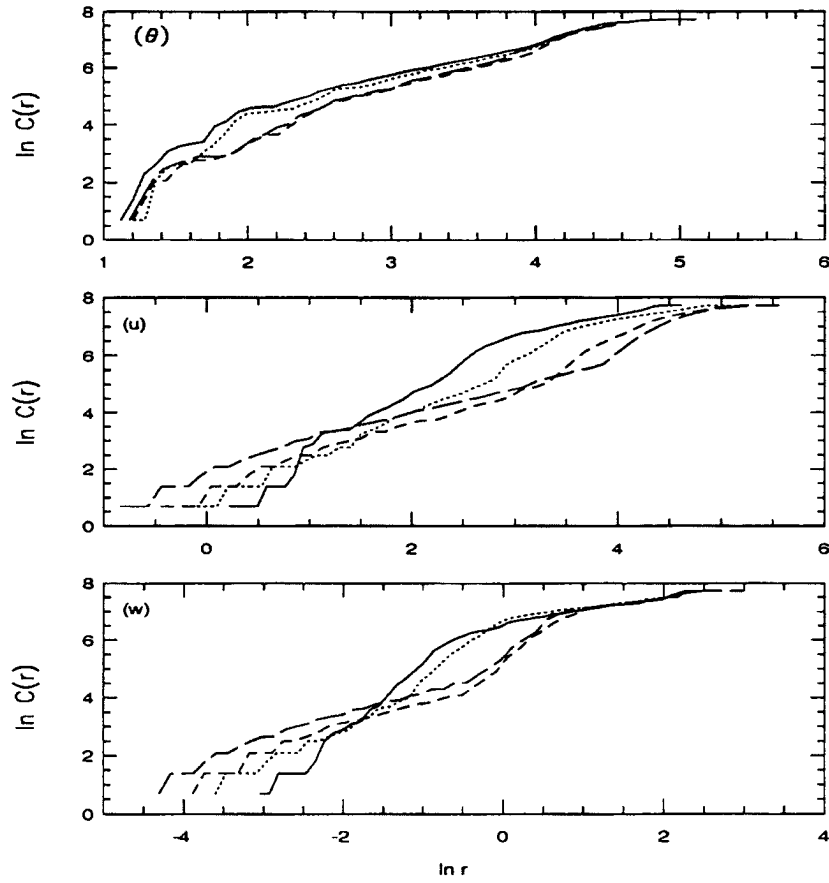


Figure 5.28: The same as in Figure 5.27 except for the cases of  $L = 10, 30, 50,$  and  $100$  km, denoted by the solid, dotted, short dashed, and long dashed lines, respectively.

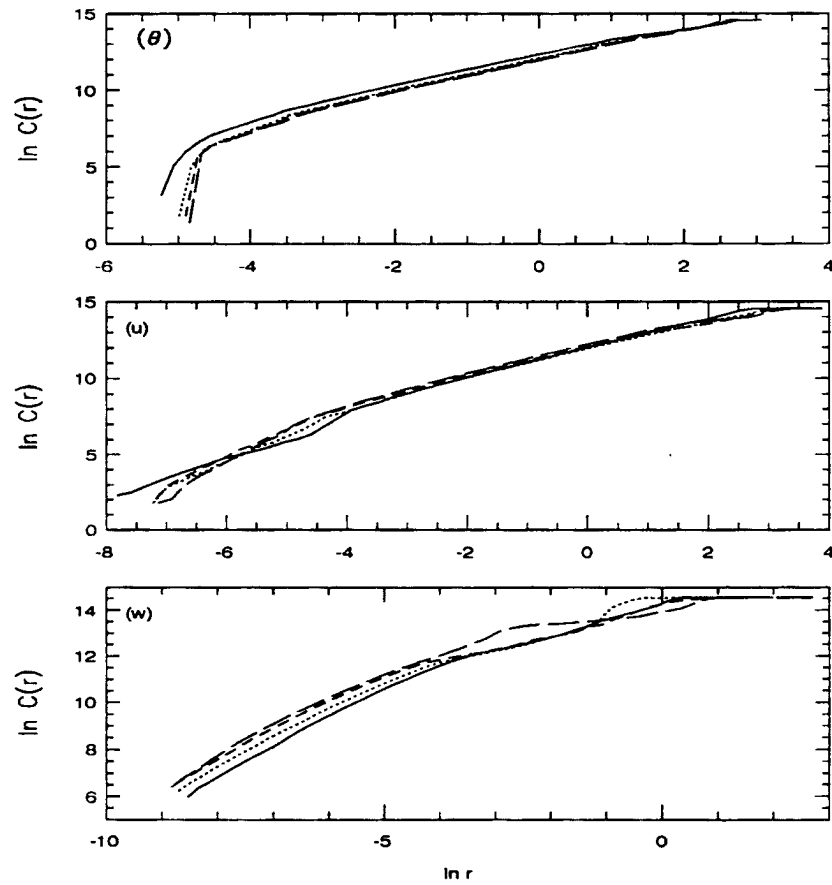


Figure 5.29: Correlation dimension plot for  $\theta$ ,  $u$ , and  $w$ , using the data at 66 grid points (11 points at each of six selected levels in the boundary layer). The solid, dotted, short dashed, and long dashed lines denote the cases of  $L = 10, 30, 50,$  and  $100$  km, respectively. Note that the term  $1/N^2$  in Eq. (5.8) is not included.

of  $L = 0$  to 5 km. An example for the case of  $L = 5$  km is given in Fig. 5.30. It is seen that, as in the above, the correlation dimensions are low. It is also seen that the  $w$  field is characterized by two distinct correlation dimensions:  $\nu$ , is higher in the lower range than in the intermediate range.

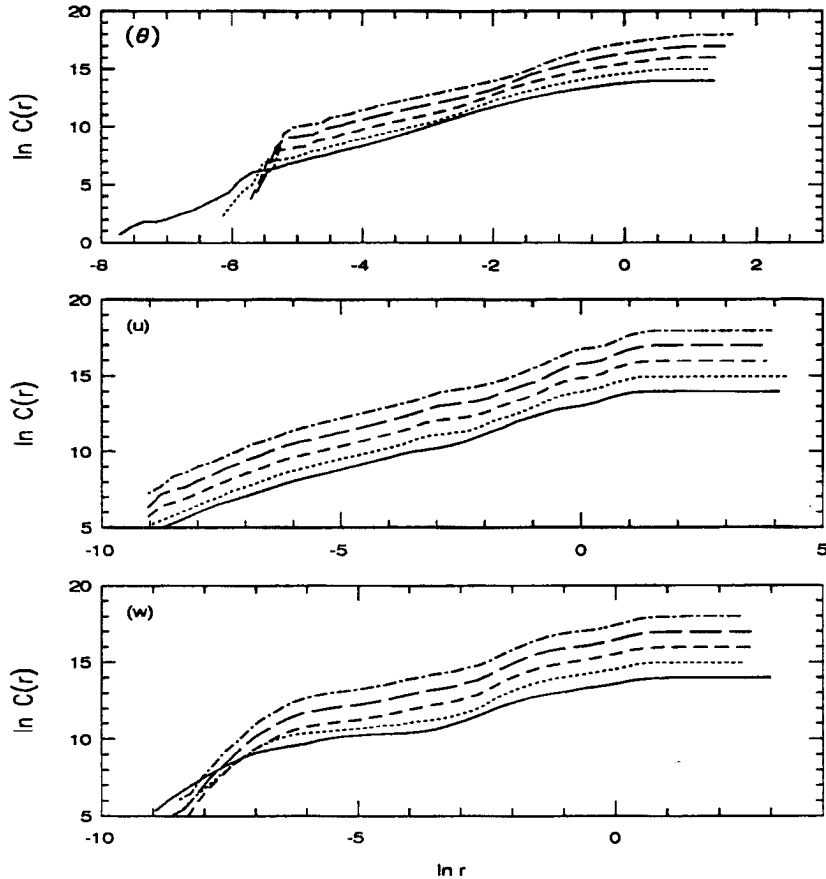


Figure 5.30: Correlation dimension plot for the case of  $L = 5$  km, using the data of  $\theta$  and  $u$  at  $z = 589$  m and of  $w$  at  $z = 637$  m. The solid, dotted, short dashed, long dashed, and dotted-dashed lines denote the phase space reconstructed by using 3, 5, 7, 9, and 11 grid points, respectively, and are separated by increments of 1 for clarity. Note that the term  $1/N^2$  in Eq. (5.8) is not included.

The other method treats the data at 11 grid points together as independent measures from a single site by concatenating the different time series from each grid point to create a single large time series of 11880 data. An example is given in Fig. 5.31 where 20 ( $\times$  40 seconds) is used as the time delay in the reconstruction of phase space. The data are

the same as those used to generate the lower panel in Fig. 5.30. As in the lower panel of Fig. 5.30, the correlation dimension is low, and there are two regimes in Fig. 5.31 with the correlation dimension higher in the lower range. Because of the low value of the correlation dimensions, the qualitative and quantitative requirements discussed in Zeng *et al.* (1992a) (and in Chap. 3) are satisfied. Therefore, we have shown by different methods that low-dimensional attractors (less than 5) exist for surface thermally-induced circulations. These low dimensions are probably associated with the magnitude of the surface heating, the horizontal differential heating due to the surface inhomogeneities, the thermal stratification, (the synoptic wind when present), and the latitude or the horizontal diffusion.

We have also made some preliminary tests of applying our algorithm (Zeng *et al.*, 1991) to estimate the Lyapunov exponents from model output. However, since the time delay, which is the e-folding time of the autocorrelation with time, is large, there are not enough independent data to compute the Lyapunov exponents. If the delay time is taken to be small, the matrix  $T_i$  (see Zeng *et al.*, 1991) is singular, and the Lyapunov exponents cannot be estimated. Although the Lyapunov-exponent spectrum cannot be obtained at this time, the largest Lyapunov exponent ( $\lambda_1$ ) can be obtained from the error growth curves at times  $t_1$  and  $t_2$ :  $\lambda_1 \approx \ln[\text{RMSP}(t_2)/\text{RMSP}(t_1)]/(t_2 - t_1)$ . Therefore, it is seen from Figs. 5.3 to 5.15 that the Lyapunov exponents are different for different variables, and different at different periods for the same variable:  $\lambda_1$  is near zero for the first few hours, is positive and approximately constant when the surface forcing is strong, and is negative again after sunset.

## 5.7 Conclusions

The predictability studies of small to large scale atmospheric flows are overviewed. The definition of predictability and the difference in the predictabilities between the large scale and mesoscale (and small scale) atmospheric flows are discussed. Using 2-D RAMS in its nonhydrostatic and compressible configuration, the predictability of the surface thermally-induced circulations is studied, including not only the sensitivity to initial conditions (i.e., the traditional predictability studies), but also the sensitive dependence on

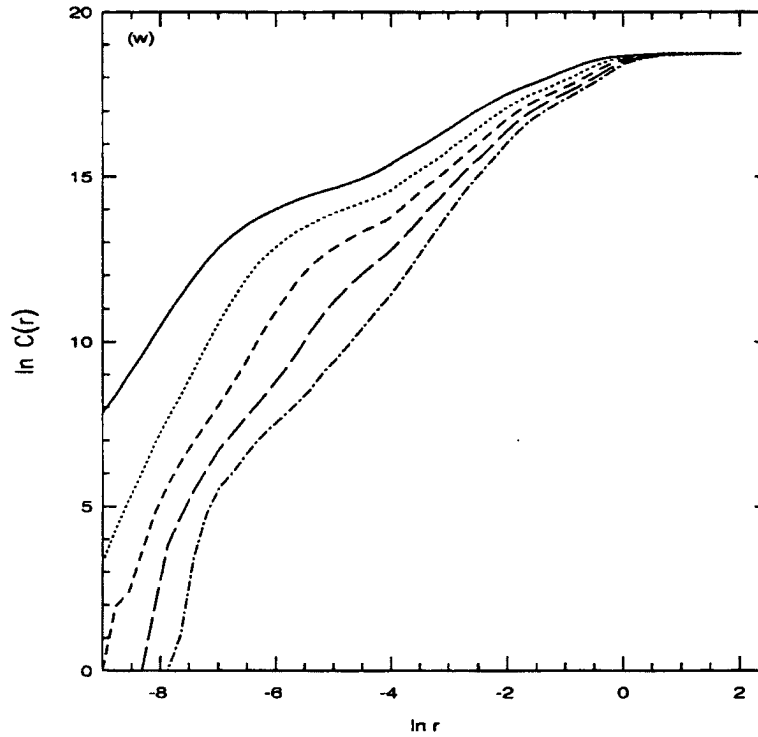


Figure 5.31: Correlation dimension plot of  $w$  for the case of  $L = 5$  km, using the data of  $\theta$  and  $u$  at  $z = 589$  m and of  $w$  at  $z = 637$  m. The solid, dotted, short dashed, long dashed, and dotted-dashed lines denote the embedding dimensions of 3, 5, 7, 9, and 11, respectively. The phase space is reconstructed from the large time series created by concatenating the different time series from 11 grids. Note that the term  $1/N^2$  in Eq. (5.8) is not included.

the boundary conditions and model parameters. It is found that the error growth (at least at the stage when the surface forcing is strong) is not sensitive to the characteristics of the initial perturbations (such as the magnitude and the horizontal scales). The reason is that the initial geostrophic adjustment process, which is the balance between the horizontal pressure gradient force and the nonlinear advection terms, is very fast (about half an hour). The adjustment processes due to the Coriolis force and sound waves, and the implicit numerical smoothing are unimportant for the initial adjustment process. However, the explicit numerical smoothing by means of the horizontal diffusion terms or filters has an important impact on the initial adjustment process. The numerical smoothing also has a strong impact on the error growth dynamics. Specifically, the strong numerical smoothing can even change the error growth property from increasing with time to decreasing with time.

It is found that the predictability is different for different variables, because different variables are governed by different detailed dynamics. Another reason may be that the coupling of different variables to rest of the variables is different, which is used in Lorenz (1991) to explain the different fractal dimensions of different variables in a system. The potential temperature is most predictable, the vertical velocity is least predictable, and the horizontal velocity is in between. It is also found that the effects of the change of the stratification in the boundary layer, the change of the latitude, the change of the simulation date (which changes the strength of surface forcing) are small on the predictability; i.e., the signal/noise ratio, although these effects are large for the signal and the noise individually. Although the ambient wind does not change the signal/noise ratios of  $\theta$  and  $u$  significantly, the increase of the ambient wind can change the  $w$  field from unpredictable to predictable in our cases. The surface thermally-induced flows are shown to be insensitive to boundary conditions. Based on sensitivity studies on selected model parameters, it is found that the change of surface roughness length and the constants in turbulence parameterizations mainly affect the  $w$  field. Especially, the flow structure is strongly affected by the specification of the initial soil water content. Because the soil parameters cannot be accurately determined in practice, it is expected that this will cause serious uncertainties in the numerical simulation of surface thermally-induced circulations.

The influence of the size of surface heat patches on the atmospheric predictability of a single realization was studied. The transition from organized flow to the situation in which fluxes are dominated by non-coherent turbulent eddies is quantitatively evaluated. The predictability of atmospheric flow is controlled by two different processes: one is the non-coherent and unpredictable turbulent eddies; the other is the coherent and predictable thermally-induced circulations. It is found that this transition is different for different variables. The potential temperature is predictable for all cases, because  $\theta$  is always well mixed in the convective boundary layer. When the size of the soil strip is greater than or equal to 5 km or so, the strong coherent circulations induced by surface forcing are dominant, and the horizontal velocity field becomes predictable. The vertical velocity field is least predictable because it is related to the derivatives of  $u$ , and small change of  $u$  can alter  $w$  significantly. Another reason is that the instantaneous state of a single realization is used in the fine-resolution simulations, which affect  $w$  field most strongly. As far as we know, our study is the first quantitative evaluation of this transition process, which is of theoretical significance in turbulence studies and of practical importance in the parameterization of the subgrid processes in large scale numerical models.

The relationship between the predictability of a realization and of an ensemble average is discussed. When a variable is highly predictable in a single realization, an ensemble average and a realization yield the same predictability. When a variable is unpredictable in a realization, it may still be predictable in an ensemble average. Therefore, an ensemble average and a realization yield the same predictability for  $\theta$  when  $L = 0$  to 150 km, for  $u$  when  $L \geq 5$  km, and for  $w$  when  $L = 10$  to 30 km.

A pair of three-dimensional mesoscale simulations were carried out with alternating water and soil strips in the  $x$ -direction and an otherwise homogeneous surface in the  $y$ -direction. It is found that results regarding the predictability are close for  $\theta$  and  $u$ , and similar for  $w$  between 2-D and 3-D simulations. A pair of 3-D LESs were also performed for the homogeneous case. It is found that results regarding the predictability are close for  $\theta$ , and similar for  $u$  and  $w$  between 2-D and 3-D fine-resolution simulations. Furthermore, domain-averaged quantities are found to be similar between 2-D and 3-D fine-resolution

simulations. Therefore, although 2-D models cannot simulate the detailed 3-D structures correctly (e.g., the eddies are larger and eddy activities are stronger in the 2-D simulations) due to its inability to resolve the variation in the y-direction and to stretch the vorticity, and due to the change of energy and enstrophy cascade processes, 2-D simulations are still useful for predictability studies. The 2-D simulations also provide guidance in the design of the computationally more costly simulations.

Further analyses of model output show that the horizontally averaged quantities are similar between the control and perturbed runs. The small discrepancies may reflect the temporal fluctuation of a spatially averaged variable in a spatial and temporal average. It is also found that the differences between the control and perturbed simulations are smaller in the presence of surface inhomogeneities than in the homogeneous case. This may imply that a smaller number of realizations are needed for an ensemble average when surface inhomogeneities are present. Obviously, further studies are needed to clarify these issues.

Computations of the autocorrelation with a space lag show the coherent circulations clearly. It is also found that the autocorrelation coefficient decreases more slowly with time for  $\theta$  and  $u$  than for  $w$ , which is consistent with the fact that  $\theta$  and  $u$  are more predictable than  $w$ . With the increase of the spatial size of the surface forcing, the autocorrelation decreases more slowly. The large peaks in the power spectra also show the surface modulation clearly. In particular, although the 2-D fine-resolution model produces larger eddies than those obtained in LES for the homogeneous case, it does not have this problem in the presence of surface inhomogeneities. Power spectra also show that the peaks are located at low frequencies for  $\theta$ , located at low and intermediate frequencies for  $u$ , and located at low and high frequencies for  $w$ . This means that the  $\theta$  field has the longest persistence, and  $w$  has the shortest persistence. The power spectra of variables in the control run and the error fields between the control and perturbed runs help explain the results of the predictability as a function of the size of heat patches.

The correlation dimensions are computed in a phase space constructed by different methods. It is found by all these methods that low (less than 5) -dimensional attractors

are present for the surface thermally-induced circulations. In the absence of ambient wind, four dimensions may be associated with the surface heating due to solar radiation, horizontal differential heating due to surface inhomogeneities, thermal stratification, and the latitude or the horizontal diffusion. The existence of low-dimensional attractors in these systems are not surprising, since, based on linear theory, these four parameters determine the gross features of the circulations. For some cases (especially of  $w$ ), there are two distinct regimes with higher correlation dimensions in the lower range of the distance  $r$  in phase space. This means that the large variations of  $w$  are controlled by a smaller number of degrees of freedom than the small variations. Finally, a preliminary analysis of the Lyapunov exponents shows that the Lyapunov exponents are different for different variables, and different during different periods for the same variable.



## Chapter 6

### CONCLUSIONS AND SUGGESTIONS FOR FUTURE WORK

#### 6.1 Conclusions

In this study, chaos theory is overviewed, and a practical method is developed to compute the Lyapunov-exponent spectrum from short time series of low precision. The application of chaos is divided into three categories, and each of these categories is studied by an example: the daisyworld model, the observational data analysis, and atmospheric predictability. These three examples are important questions themselves in the atmospheric sciences. They are unrelated themselves, but are unified under chaos. In this section, only the major points from this study are summarized. More detailed conclusions have been given in each of the previous chapters.

- (i) Chaos theory is overviewed, which includes the bifurcation and routes to turbulence, and the characterization of chaos such as dimensions, Lyapunov exponents, and Kolmogorov-Sinai entropy. We divide the application of chaos into three categories: new ideas inspired by chaos, observational data analysis, and numerical model output analysis. This overview and classification also demonstrate that current emphasis on the computation of fractal dimensions from observational data and the debate regarding the existence of low-dimensional attractors in the atmosphere are just small parts of chaos theory and its application in the atmosphere.
- (ii) The computation of the Lyapunov-exponent spectrum is simple in principle, but very subtle in practice. Different techniques from different sources are compiled to give a comprehensive overview of different aspects of this computation for the first time in the literature. Based on theoretical reasoning and our experiences, we select suitable

options from different techniques to develop our own method. All parameters are tuned so that our scheme contains no free adjustable parameters, and hence can be easily used by other researchers with or without experience. Using various known model systems, both finite- and infinite-dimensional, it is found that our method can give reasonable results from short time series of low precision.

- (iii) Using observational daily data of surface temperature and pressure in the United States and over the North Atlantic Ocean, the fractal dimensions and the Lyapunov exponents are estimated. Although our time series are longer than those used in the previous studies, it is found that no saturated value of the correlation dimension can be obtained. Based on the qualitative and quantitative requirements of the data for the computation of the correlation dimensions, it is found that most, if not all, of the previous estimates of low dimensional attractors are spurious. Therefore, we claim that there probably exist no low-dimensional attractors from observational data in the atmosphere. Different from the previous studies on the computation of the Lyapunov exponents from observational data, we relate our computations to the climate signal/noise ratio analysis. It is found that the error-doubling time is 2 to 8 days at different locations. The predictability time is longer in an area of higher climate signal/noise ratio. The predictability time for daily data for the entire year is shorter than that for summer and/or winter data. The relationship between our estimates and those based on general circulation models is also discussed.
- (iv) When the differential model is used for daisyworld as in Watson and Lovelock (1983), it is found that a steady state is always maintained, not only for one or two species (as in Watson and Lovelock), but also for more than two species. However, we argue that, physically, a more appropriate model for daisyworld should be the discrete model, rather than the differential model. When the discrete model is used, it is known that chaos is possible without the feedback between the biota and the environment. When the feedback is included, we find that periodic, and even chaotic, behavior still exists in daisyworld with one or two species, with the controlling parameter being the strength of the coupling between the daisies and the environmental

temperature. Computations of the power spectra, fractal dimensions, and Lyapunov exponents verify the existence of chaos in daisyworld. Therefore, our results show that the presence of daisies in daisyworld does not always stabilize the climate conditions of the environment, and the feedback from the environment does not always lead to steady-state behaviors. These results raise questions regarding the validity and the interpretation of the Gaia hypothesis.

- (v) The atmospheric predictability of microscale to planetary-scale motions are overviewed, which is, as far as we know, the most comprehensive updated review of the atmospheric predictability studies. Using the 2-D RAMS in its nonhydrostatic and compressible configuration, it is found that the error growth (at least at the stage when the surface forcing is strong) is not very sensitive to the characteristics of the initial perturbations, due to the very fast geostrophic adjustment process (of about half an hour), which is the balance between the horizontal pressure gradient term and the nonlinear advection terms. The explicit horizontal diffusion terms and filters can strongly affect not only the initial adjustment process but also the error growth dynamics. Especially, the strong numerical smoothing can even change the error growth property from increasing with time to decreasing with time.
- (vi) It is found that the predictability is variable-dependent: the potential temperature is most predictable, the vertical velocity is least predictable, and the horizontal velocity is in between. The mesoscale flow is shown to be insensitive to boundary conditions. Among the conclusions regarding the influence of the boundary layer structures and model parameters on the predictability and on the flow structures, it is found that an increase of the ambient wind can change the vertical wind field from unpredictable to predictable in our cases. The flow structure is strongly affected by the specification of the initial soil water content.
- (vii) The transition from organized flow to the situation in which fluxes are dominated by non-coherent turbulent eddies is quantitatively evaluated. This transition is determined by two different processes: one is the non-coherent and unpredictable turbulent eddies; the other is the coherent and predictable thermally-induced circulations.

This transition is different for different variables: the potential temperature from an ensemble average or from a realization is predictable and gives the same predictability, which is independent of the size of the surface inhomogeneities; the horizontal velocity from an ensemble average or from a realization is predictable and gives the same predictability when the size of heat patches is equal to or greater than about 5 km; the vertical velocity from an ensemble average or from a realization is predictable and gives similar predictability when the size of heat patches is between about 10 to 30 km. The reasons are also discussed. The predictability and the coherent circulations modulated by the surface inhomogeneities are also studied by computing the autocorrelations and the power spectra of variables in the control run and the error fields between the control and perturbed runs. The relationship between the predictability of an ensemble average and of a realization is also discussed.

- (viii) The eddies are larger and the eddy activities are stronger in the 2-D fine-resolution simulations than in 3-D LES. However, the 2-D mesoscale (or fine-resolution) simulation yields close or similar results regarding the predictability as those from 3-D mesoscale (or fine-resolution) simulations. The horizontally averaged quantities based on 2-D fine-resolution simulations are characteristic of those based on 3-D LES.
- (ix) The fractal dimension is computed in phase space constructed by different methods. It is found that low (less than 5) -dimensional attractors are present for the surface thermally-forced circulations. Four dimensions may be associated with the surface heating due to solar radiation, the horizontal differential heating due to surface inhomogeneities, the thermal stratification, and the latitude or the horizontal diffusion in the absence of ambient wind. Finally, a preliminary analysis shows that the Lyapunov exponents are different for different variables, and different during different periods for the same variable.

## 6.2 Suggestions for Future Work

Because this work involves my research on a few different subjects, many suggestions for future research became apparent during the course of this work. Some of these suggestions are due to the inspiration of chaos—one of the application of chaos theory.

- (i) Only the mono-fractal dimension is computed in our study. A more appropriate tool to characterize the nonlinear dynamical processes is the multifractal spectrum of dimensions. Although the qualitative and quantitative data requirements have been established for the computation of the mono-fractal dimensions, the corresponding requirements have not yet been studied.
- (ii) Although it is not directly related to chaos, a new technique called wavelet transformation, of which I became aware during this work, contains not only the frequency information (as the Fourier transformation) but also the phase information. Therefore, this tool is very helpful to study the spatial intermittency and the spatial-temporal nonlinear variations.
- (iii) I hypothesize that the predictability should be universal for certain types of dynamical systems. One way to test this hypothesis is to follow the milestone work of Feigenbaum (1978, 1979a) which lead to the well-known Feigenbaum constants. The advanced mathematical theory on the renormalization group is needed for this research.
- (iv) Noise reduction is a very active research area in nonlinear science. This can be related to the 4DDA, especially by the adjoint method. For example, observational data can be processed by noise reduction techniques before 4DDA. Some methods in noise reduction may also be used to improve the 4DDA by the adjoint method.
- (v) Lyapunov exponents are the time averages of the local (temporal) rates of divergence. Higher moments of these local rates are also helpful to understand the fine structure of the attractors.

- (vi) For high-dimensional complex systems (such as the atmosphere), the embedding dimension may be smaller than the fractal dimension. This may be related to the slight sensitivity to the selection of the time delay  $\tau$  in the computation of the Lyapunov exponents from observational data, as reported in Chapter 3. It is assumed in Chapter 3 that at least the first few positive exponents can be reasonably estimated. Considering the practical significance of this assumption, further work is needed.
- (vii) Figure 4.1 shows an example regarding biodiversity. Since biodiversity loss is a very important environmental problem, further work on this topic is needed.
- (viii) Between the differential model of Watson and Lovelock (1983) and our discrete model of daisyworld, there exists another model—the time delay differential model. Some work based on this model has been done in De Gregorio *et al.* (1992) and Flynn and Eykholt (1992). The biodiversity problem may be studied by these models.
- (ix) Our 2-D simulations have led to many conclusions. We have shown that the major results on the error growth dynamics and the predictability as a function of the size of surface inhomogeneities are consistent with those based on 3-D mesoscale simulations using 2-D forcing. Using 3-D simulations with 3-D forcing, further work is needed to extend these conclusions to more realistic situations.
- (x) Our conclusions regarding the predictability as a function of the size of the surface inhomogeneities are based on the condition of calm mean wind. Further work is needed to evaluate the influence of mean wind on this transition process.
- (xi) The moisture is taken as a tracer in our study. An important question is whether our conclusions will be changed by moist processes. Further work is needed on this topic.
- (xii) When 3-D LES is used, it would be interesting to compare the predictability of the individual realizations with that of the ensemble average. In addition, it is concluded in Chapter 5 that surface inhomogeneities decrease the required number of individual realizations for an ensemble average. Considering its importance, further study is needed.

- (xiii) Because of the rapid increase of computer power, small grid increments (such as a few hundred meters or a few kilometers) have begun to be used in mesoscale simulations. One problem is the adjustment of the constants in the turbulence parameterization when the grid increments are changed. A related question is how to compare results based on different resolutions.
- (xiv) The computation of the Lyapunov exponents provides a new tool for model output analysis. Further work is needed to apply this method to different model output.
- (xv) The predictability in the Eulerian frame is usually emphasized. The predictability study in the Lagrangian frame should also be very helpful. In addition, the computation of the fractal dimensions and Lyapunov exponents can be carried out easily in the Lagrangian frame.
- (xvi) The adjoint technique has been applied to a diverse set of problems (e.g., Errico and Vukicevic, 1991) which are all related to the predictability problem. Further work is needed to improve our understanding of the usefulness of the adjoint method in the predictability problems and of the usefulness of the results from predictability studies in the application of the adjoint method.

The above suggestions are still a partial list of my ideas gained in my research on chaos theory and its application in the atmosphere in the past few years. Those unlisted ideas are related to the extended-range forecasting, pollutant dispersion, numerical schemes, model grids, synoptically-induced mesoscale dynamics, and climate dynamics. The diversity of these ideas is again an indication of the power of chaos. Indeed, it is expected that more and more researchers will be inspired by chaos in their scientific work.



## Chapter 7

### REFERENCES

- Abarbanel, H.D.A., R. Brown, and J.B. Kadtko, 1990: Prediction in nonlinear chaotic systems: Methods for time series with broadband Fourier spectra. *Phys. Rev.*, **A41**, 1782-1807.
- Abe, S. and T. Yoshida, 1982: The effects of the widths of a peninsula to the sea breeze. *J. Meteor. Soc. Japan*, **60**, 1074-1084.
- Aleksic, Z., 1991: Estimating the embedding dimension. *Physica*, **D52**, 362-368.
- Anthes, R.A., 1984a: Predictability of mesoscale meteorological phenomena. *Predictability of fluid motions*. Holloway, G. and B.J. West, Ed., AIP Conference Proceedings No. 106. 247-270.
- Anthes, R.A., 1984b: The general question of predictability. *Preprint NCAR Ms. 0901-84-04*.
- Anthes, R.A., Y.H. Kuo, D.P. Baumhefner, R.M. Errico, and T.W. Bettge, 1985: Predictability of mesoscale motions. *Advances in Geophysics*. **28**, *Issues in Atmospheric and Oceanic Modeling Part B: Weather Dynamics*, Academic Press, 159-202.
- Anthes, R.A., Y.H. Kuo, E.Y. Hsie, S. Low-Nan, and T.W. Bettge, 1989: Estimation of skill and uncertainty in regional numerical models. *Q. J. R. Meteorol. Soc.*, **115**, 763-806.
- Arakawa, A. and V.R. Lamb, 1981: A potential enstrophy and energy conserving scheme for the shallow water equations. *Mon. Wea. Rev.*, **109**, 18-36.

- Atmanspacher, H., H. Scheingraber, and W. Voges, 1988: Global scaling properties of a chaotic attractor reconstructed from experimental data. *Phys. Rev.*, **37A**, 1314-1322.
- Badii, R. , G. Broggi, B. Derighetti, M. Ravani, S. Ciliberto, A. Politi, and M.A. Rubio, 1988: Dimension increase in filtered chaotic signals. *Phys. Rev. Lett.*, **60**, 979-982.
- Badii, R. and A. Politi, 1985: Statistical description of chaotic attractors: The dimension function. *J. Stat. Phys.*, **40**, 725-750.
- Baumhelfner, D.P., 1984: The relationship between present large-scale forecast skill and new estimates of predictability error growth. *Predictability of Fluid Motions*. Holloway, G. and B.J. West, Ed., IAP Conference Proceedings No. 106, 169-180.
- Bennetin, G., L. Galgani and J.M. Strelcyn, 1976: *Phys. Rev.*, **A 14**, 2338-2345.
- Bentley, J.L. and J.H. Friedman, 1979: *ACM Comput. Surv.*, **11**, 397.
- Benzi, R. and G.F. Carnevale, 1989: A possible measure of local predictability. *J. Atmos. Sci.*, **46**, 3595-3598.
- Bergé, P., Y. Pomeau, and C. Vidal, 1984: *Order within chaos*. John Wiley and Sons, Inc., New York, 329pp.
- Berri, G.J. and J. Paegle, 1990: Sensitivity of local predictability to initial conditions. *J. Appl. Meteor.*, **29**, 256-267.
- Breeden, J.L. and A. Hübler, 1990: Reconstructing equations of motion from experimental data with unobserved variables. *Phys. Rev.*, **A42**, 5817-5826.
- Briggs, K., 1990: An improved method for estimating Lyapunov exponents of chaotic time series. *Phys. Lett.*, **A151**, 27-32.

- Brown, R., P. Bryant, and H.D.I. Abarbanel, 1991: Computing the Lyapunov spectrum of a dynamical system from an observed time series. *Phys. Rev.*, **A43**, 2787-2806.
- Bryant, P., R. Brown, and H.D.I. Abarbanel, 1990: Lyapunov exponents from observed time series. *Phys. Rev. Lett.*, **65**, 1523-1526.
- Bretherton, C.S., 1990: A multifractal model of entrainment into a stratocumulus cloud top. *preprints of AMS Cloud Physics Conference*, San Francisco, 1990, paper 1B.2.
- Broomhead, D.S. and G.P. King, 1986: Extracting qualitative dynamics from experimental data. *Physica*, **20D**, 217-236.
- Campbell, D.K., 1990: *Chaos/XAOC: Soviet-American perspectives on nonlinear science*. The American Institute of Physics, 500pp.
- Caputo, J.G., B. Malmaison, and P. Atten, 1986: Determination of attractor dimension and entropy for various flows: an experimentalist's viewpoint. *Dimensions and Entropies in Chaotic Systems*. G. Mayer-Kress, Ed., Springer-Verlag, 180-190.
- Carter, R.N. and S.D. Prince, 1981: Epidemic models used to explain biogeographical distribution limits. *Nature*, **213**, 644-645.
- Casdagli, M., S. Eubank, J.D. Farmer, and J. Gibson, 1991: State space reconstruction in the presence of noise. *Physica*, **D51**, 52-98.
- Charney, J.G., 1975: Dynamics of deserts and drought in the Sahel. *Q. J. R.oy. Meteorol. Soc.*, **101**, 193-202.
- Charney, J.G., R.G. Fleagle, H. Riehl, V.E. Lally, and D.Q. Wark, 1966: The feasibility of a global observation and analysis experiment. *Bull Amer. Meteor. Soc.*, **47**, 200-220.
- Chen, W.Y., 1989: Estimate of dynamical predictability from NMC DERF experiments. *Mon. Wea. Rev.*, **117**, 1227-1236.

- Chen, C. and W.R. Cotton, 1983a: A one-dimensional simulation of the stratocumulus-capped mixed layer. *Bound.-Layer Meteor.*, **25**, 289-321.
- Chen, C. and W.R. Cotton, 1983b: Numerical experiments with a one-dimensional higher-order turbulence model: Simulation of the Wangara 33 case. *Bound.-Layer Meteor.*, **25**, 375-404.
- Clarke, R.H., 1970: Recommended methods for the treatment of the boundary layer in numerical models. *Aust. Meteorol. Mag.*, **18**, 51-73.
- Cotton, W.R. and R.A. Anthes, 1989: *Storm and Cloud Dynamics*. Academic Press, 883pp.
- Cotton, W.R., C.J. Tremback, and R.L. Walko, 1988: CSU RAMS: A cloud model goes regional. *Proc. NCAR Workshop on limited-area modeling intercomparison*, Nov. 15-18, NCAR, Colorado, 202-211.
- Cotton, W.R., R.L. Walko, K.R. Costigan, P.J. Flatau, and R.A. Pielke, 1990: Using RAMS in LES mode—From inhomogeneous surfaces to cirrus clouds. Presented at *Large Eddy Simulation Workshop*, 19-21 December 1990, St. Petersburg, Fl. To be published by Cambridge Press.
- Cram, J.M., 1990: Numerical simulation and analysis of the propagation of a prefrontal squall line. Ph.D. dissertation. Dept. of Atmos. Sci. Colorado State University, 332pp.
- Dalcher, A. and E. Kalnay, 1987: Error growth and predictability in operational ECMWF forecasts. *Tellus*, **39A**, 474-491.
- Dalu, G.A. and R.A. Pielke, 1989: An analytical study of the sea breeze. *J. Atmos. Sci.*, **46**, 1815-1825.

- Dalu, G.A. and R.A. Pielke, 1992: Vertical heat fluxes generated by mesoscale atmospheric flow induced by thermal inhomogeneities in the PBL. *J. Atmos. Sci.* submitted.
- Dalu, G.A., R.A. Pielke, R. Avissar, G. Kallos, M. Baldi, and A. Guerrini, 1992: Linear impact of thermal inhomogeneities on mesoscale atmospheric flow with zero synoptic wind. *Ann. Geophys.*, **9**, 641-647.
- Deardorff, J.W., 1980: Stratocunulus-capped mixed layers derived from a three dimensional model. *Bound.-Layer Meteor.*, **18**, 495-527.
- Deardorff, J.W. and G.E. Willis, 1985: Further results from a laboratory model of the convective planetary boundary layer. *Bound.-Layer Meteor.*, **32**, 205-236.
- De Gregorio, S., R.A. Pielke, and G.A. Dalu, 1992: A delayed biophysical system for the Earth climate. *J. Nonlinear Sci.*, accepted.
- Déqué. M., 1988: 10-day predictability of the northern hemisphere winter 500-mb height by the ECMWF operational model. *Tellus*, **40A**, 26-36.
- Drogemeier, K.K., 1985: The numerical simulation of thunderstorm outflow dynamics. Ph.D. dissertation, Dept. of Atmos. Sci., University of Illinois, 695pp.
- Eckmann, J.-P., 1981: Roads to turbulence in dissipative dynamical systems. *Rev. Mod. Phys.*, **53**, 643-654.
- Eckmann, J.-P. and D. Ruelle, 1985: Ergodic theory of chaos and strange attractors. *Rev. Mod. Phys.*, **57**, 617-656.
- Eckmann, J.-P., S. Ollifson Kamphorst, D. Ruelle, and S. Ciliberto, 1986: Lyapunov exponents from time series. *Phys. Rev.*, **34A**, 4971-4979.
- ECMWF, 1988: Predictability in the medium and extended range. Workshop proceedings held at ECMWF, Shinfield Park, Reading RG2 9AX, UK.

- Errico, R.M. and D.P. Baumhefner, 1987: Predictability experiments using a high-resolution limited-area model. *Mon. Wea. Rev.*, **115**, 488-504.
- Errico, R.M. and T. Vukicevic, 1991: Sensitivity analysis using an adjoint of the PSU/NCAR mesoscale model. *preprints* NCAR 0501/91-3.
- Essex, C., T. Lookman, and M.A.H. Nerenberg, 1987: The climate attractor over short time scales. *Nature*, **326**, 64-66.
- Eykholt, R. and D.K. Umberger, 1988: Relating the various scaling exponents used to characterize fat fractals in nonlinear dynamical systems. *Physica*, **30D**, 43-60.
- Farmer, J.D., 1982: Information dimension and the probabilistic structure of chaos. *Z. Naturforsch*, **37A**, 1304-1325.
- Farrell, B.F., 1990: Small error dynamics and predictability of atmospheric flows. *J. Atmos. Sci.*, **47**, 2409-2416.
- Feigenbaum, M.J., 1978: Quantitative universality for a class of nonlinear transformations. *J. Stat. Phys.*, **19**, 25-52.
- Feigenbaum, M.J., 1979a: The universal metric properties of nonlinear transformations. *J. Stat. Phys.*, **21**, 669-706.
- Feigenbaum, M.J., 1979b: The onset spectrum of turbulence. *Phys. Lett.* **74A**, 375-378.
- Flynn, C.M. and R. Eykholt, 1992. Chaos in Daisyworld with time-delay differential equations. Submitted to *Tellus B*.
- Fraedrich, K., 1986: Estimating the dimensions of weather and climate attractors. *J. Atmos. Sci.*, **43**, 419-432.
- Fraedrich, K., 1987: Estimating weather and climate predictability on attractors. *J. Atmos. Sci.*, **44**, 722-728.

- Fraedrich, K and L.M. Leslie, 1989: Estimates of cyclone track predictability. I: Tropical cyclones in the Australian region. *Quart. J. Roy. Meteor. Soc.*, **115**, 79-92.
- Fraedrich, K., R. Grotjahn, and L.M. Leslie, 1990: Estimates of cyclone track predictability. II: Fractal analysis of midlatitude cyclones. *Quart. J. Roy. Meteor. Soc.*, **116**, 317-335.
- Frank, G.W., T. Lookman, and A.H. Nerenberg, 1990: Recovering the attractor: A review of chaotic time-series analysis. *Can. J. Phys.*, **68**, 711-718.
- Fraser, A.M. and H.L. Swinney, 1986: Independent coordinates for strange attractors from mutual information. *Phys. Rev.*, **33A**, 1134-1140.
- Fraser, A.M., 1989: Reconstructing attractors from scalar time series: A comparison of singular system and redundancy criteria. *Physica*, **D34**, 391-404.
- Fredrickson, P., J.L. Kaplan, E.D. Yorke, and J.A. Yorke, 1983: The Lyapunov dimension of strange attractors. *J. Diff. Eq.*, **49**, 185-207.
- Garratt, J.R. and R.A. Pielke, 1989: On the sensitivity of mesoscale models to surface-layer parameterization constants. *Bound.-Layer Meteor.*, **48**, 377-387.
- Garratt, J.R., R.A. Pielke, W.F. Miller, and T.J. Lee, 1990: Mesoscale model response to random, surface-based perturbations - A sea-breeze experiment. *Bound.-Layer Meteor.* **52**, 313-334.
- Geist, K., U. Parlitz, and W. Lauterborn, 1990: Comparison of different methods for computing Lyapunov exponents. *Prog. Theor. Phys.*, **83**, 875-882.
- Gifford, F.A., 1991: The structure of atmospheric diffusion at regional scales. Final technical report for U.S. Army Research Office, 19pp.

- Goswami, B.N. and J. Shukla, 1991: Predictability of a coupled ocean-atmosphere model. *J. Climate*, **4**, 3-22.
- Grassberger, P. and I. Procaccia, 1983a: Characterization of strange attractors. *Phys. Rev. Lett.*, **50**, 346-349.
- Grassberger, P. and I. Procaccia, 1983b: Estimating the Kolmogorov entropy from a chaotic signal. *Phys. Rev.*, **28A**, 2591-2593.
- Grassberger, P. and I. Procaccia, 1983c: Measuring the strangeness of strange attractors. *Physica*, **9D**, 189-208.
- Grassberger, P. and I. Procaccia, 1984: Dimensions and entropies of strange attractors from a fluctuating dynamics approach. *Physica*, **13D**, 34-54.
- Grebogi, C., E. Ott, and J.A., Yorke, 1982: Chaotic attractors in crisis. *Phys. Rev. Lett.*, **48**, 1507-1510.
- Guckenheimer, J. and P. Holmes, 1983: *Nonlinear Oscillations, Dynamical Systems and Bifurcations of Vector Fields*. Springer-Verlag, 453pp.
- Hadamard, J., 1898: Les surfaces à courbures opposées et leurs lignes géodésiques. *J. Math. Pures Appl.*, **4**, 27-73.
- Hadfield, M.G., W.R. Cotton, and R.A. Pielke, 1991: Large-eddy simulations of the thermally forced circulations in the convective boundary layer. Part I: A small scale circulation with zero wind. *Bound.-Layer Meteor.*, **57**, 79-114.
- Hadfield, M.G., W.R. Cotton, and R.A. Pielke, 1992: Large-eddy simulations of the thermally forced circulations in the convective boundary layer. Part II: The effect of changes in wavelength and wind speed. *Bound.-Layer Meteor.*, **58**, 307-328.

- Haidvogel, D.B. and G. Holloway, 1984: Predictability: Lagrangian and Eulerian views. *Predictability of Fluid Motions* Holloway, G. and B.J. West, Ed., IAP Conference Proceedings No. 106, 67-77.
- Halsey, T.C., M.H. Jensen, L.P. Kadanoff, I. Procaccia, and B. Shraiman, 1986: Fractal measures and their singularities: The characterization of strange sets. *Phys. Rev.*, **33A**, 1141-1151.
- Hao, B.-L., 1984: *Chaos*. World Scientific, Singapore, 576pp.
- Hense, A., 1987: On the possible existence of a strange attractor for the southern oscillation. *Beitr. Phys. Atmos.*, **60**, 34-47.
- Hentschel, H.G.E. and I. Procaccia, 1983: The infinite number of generalized dimensions of fractals and strange attractors. *Physica*, **8D**, 435-444.
- Hill, G.E., 1974: Factors controlling the size and spacing of cumulus clouds as revealed by numerical experiments. *J. Atmos. Sci.*, **31**, 646-673.
- Holzfuß, J. and G. Mayer-Kress, 1986: An approach to error-estimation in the application of dimension algorithms. *Dimensions and Entropies in Dynamical Systems*, G. Mayer-Kress, Ed., Springer-Verlag, 114-122.
- Hopf, E., 1948: A mathematical example displaying features of turbulence. *Commun. Pure Appl. Math.*, **1**, 303-322.
- Hurewicz, W. and H. Wallman, 1948: *Dimension theory*. Princeton.
- Idso, S.B., 1981: Surface energy balance and the genesis of deserts. *Arch. Meteorol. Geophys. Bioclimatol. Ser.*, **A 30**, 253-260.
- Keppenne, C.L. and C. Nicolis, 1989: Global properties and local structure of the weather attractor over western Europe. *J. Atmos. Sci.*, **46**, 2356-2370.

- Kolmogorov, A.N., 1958: A new metric invariant of transient dynamical systems and automorphisms in Lebesgue spaces. *Dokl. Akad. Nauk, SSSR*, **119**, 861-864. [*Sov. Phys. Dokl.*, **112**, 426-429].
- Kostelich, E.J. and J.A. Yorke, 1990: Noise reduction: Finding the simplest dynamical system consistent with the data. *Physica*, **D41**, 183-196.
- Krettenauer, K. and U. Schumann, 1991: Numerical simulation of turbulent convection over wavy terrain. *J. Fluid Mech.* To appear.
- Kuo, Y.H. and S. Low-Nan, 1990: Predictability of nine explosive cycles over the western Atlantic Ocean with a regional model. *Mon. Wea. Rev.*, **118**, 3-25.
- Landau, L.D., 1944: On the problem of turbulence. *Dokl. Akad. Nauk. SSSR* **44**, 339-342. Its English translation is in *Collected papers of Landau*, Ed. by ter Harr, Pergamon, 1965.
- Lee, T.J. and R.A. Pielke, 1992: Estimating the soil surface specific Humidity. *J. Appl. Meteorol.*, **31**, 480-484.
- Leith, C.E., 1971: Atmospheric predictability and two-dimensional turbulence. *J. Atmos. Sci.*, **28**, 145-161.
- Leith, C.E. and R.H. Kraichnan, 1972: Predictability of turbulent flows. *J. Atmos. Sci.*, **29**, 1041-1058.
- Li, T.-Y. and J.A. Yorke, 1975: Period three implies chaos. *Am. Math. Mon.*, **82**, 985-992.
- Lilly, D.K., 1962: On the numerical simulation of buoyant convection. *Tellus*, **14**, 148-172.
- Lilly, D.K., 1984: Some facets of the predictability problem for atmospheric mesoscales. *Predictability of Fluid Motions*, Holloway, G. and B.J. West, Ed., IAP Conference Proceedings No. 106, 287-294.

- Lilly, D.K., 1989: Two-dimensional turbulence generated by energy sources at two scales. *J. Atmos. Sci.*, **46**, 2026-2030.
- Lilly, D.K., 1990: Numerical prediction of thunderstorms-has its time come? *Q. J. R. Meteorol. Soc.*, **116**, 779-798.
- Lorenz, E.N., 1963: Deterministic nonperiodic flow. *J. Atmos. Sci.*, **20**, 130-141.
- Lorenz, E.N., 1969a: Three approaches to atmospheric predictability. *Bull. Amer. Meteor. Soc.*, **50**, 345-349.
- Lorenz, E.N., 1969b: Atmospheric predictability as revealed by natural occurring analogues. *J. Atmos. Sci.*, **26**, 636-646.
- Lorenz, E.N., 1969c: The predictability of a flow which possess many scales of motion. *Tellus*, **21**, 289-307.
- Lorenz, E.N., 1982: Atmospheric predictability experiments with a large numerical model. *Tellus*, **34**, 505-513.
- Lorenz, E.N., 1984a: The local structure of a chaotic attractor in four dimensions. *Physica*, **D13**, 90-104.
- Lorenz, E.N., 1984b: Estimates of atmospheric predictability at medium range. *Predictability of Fluid Motions*, Holloway, G. and B.J. West, Ed., IAP Conference Proceedings No. 106, 133-140.
- Lorenz, E.N., 1987: Deterministic and stochastic aspects of atmospheric dynamics. *Irreversible Phenomena and Dynamical Systems Analysis in Deosciences*, Nicolis, C. and G. Nicolis, Ed., D. Reidel Publishing Co. 159-179.
- Lorenz, E.N., 1991a: The general circulation of the atmosphere: an evolving problem. *Tellus*, **43AB**, 8-15.

- Lorenz, E.N., 1991b: Dimension of weather and climate attractors. *Nature*, **353**, 241-244.
- Louis, J.F., 1979: A parametric model of vertical eddy fluxes in the atmosphere. *Bound.-Layer Meteor.*, **17**, 187-202.
- Lovejoy, S. and D. Schertzer, 1990: Multifractals, universality classes and satellite and radar measurements of cloud and fields. *J. Geophys. Res.*, **95 D3**, 2021-2034.
- Lovejoy, S. and D. Schertzer, 1991: Multifractal analysis techniques and the rain and cloud fields from  $10^{-3}$  to  $10^6$  m. in *Scaling, Fractals and Nonlinear Variability in Geophysics*. Schertzer, D. and S. Lovejoy, Ed., Kluwer Academic Publishers, 111-144.
- Lovelock, J.E., 1972: Gaia as seen through the atmosphere. *Atmos. Environ.*, **6**, 579-580.
- Lovelock, J.E., 1982: Gaia as seen through the atmosphere. *Biomineralization and biological metal accumulation* Westbroek, P. and E.W. de Jong, Ed., D. Reidel Publishing Co., Dordrecht, The Netherlands, 15-25.
- Lovelock, J.E., 1986: Geophysiology: A new look at earth science. *Bull. Amer. Met. Soc.*, **67**, 392-397.
- Lovelock, J.E., and L. Margulis, 1974: Atmospheric homeostasis by and for the biosphere: the Gaia hypothesis. *Tellus*, **21**, 1-9.
- Mackey, M.C. and L. Glass, 1977: Oscillation and chaos in physiological control system. *Science*, **197**, 287-289.
- Madden, R.A., 1976: Estimates of the natural variability of time-averaged sea-level pressure. *Mon. Wea. Rev.*, **104**, 942-952.
- Madden, R.A. and D.J. Shea, 1978: Estimates of the natural variability of time-averaged temperatures over the United States. *Mon. Wea. Rev.*, **106**, 1695-1703.

- Mahrer, Y. and M. Segal, 1985: On the effects of islands' geometry and size on inducing sea-breeze circulation. *Mon. Wea. Rev.*, **113**, 170-174.
- Mandelbrot, B, 1983: *The fractal geometry of nature*. Freeman and Co., New York.
- Manneville, P. and Y. Pomeau, 1980: Different ways to turbulence in dissipative dynamical systems. *Physica*, **1D**, 219-226.
- Marek, M. and I. Schreiber, 1991: *Chaotic behavior of deterministic dissipative systems*. Cambridge University Press, New York. 365pp.
- Mason, P.J., 1989: Large-eddy simulation of the convective atmospheric boundary layer. *J. Atmos. Sci.*, **46**, 1492-1516.
- May, R.M., 1974: Biological populations with nonoverlapping generations: Stable points, stable cycles, and chaos. *Science*, **186**, 645-647.
- May, R.M. 1976. Simple mathematical models with very complicated dynamics. *Nature*, **261**, 459-467.
- McCumber, M.C. and R.A. Pielke, 1981: Simulation of the effects of surface fluxes of heat and moisture in a mesoscale numerical model. I: Soil model. *J. Geophys. Res.*, **86**, C10, 9929-9938.
- McNider, R.T. and R.A. Pielke, 1981: Diurnal boundary-layer development over sloping terrain. *J. Atmos. Sci.*, **38**, 2198-2212.
- Mees, A.I., P.E. Rapp, and L.S. Jennings, 1987: Singular-value decomposition and embedding dimension. *Phys. Rev.*, **A38**, 340-346.
- Mellor, G.L. and T. Yamada, 1974: A hierarchy of turbulence closure models for planetary boundary layers. *J. Atmos. Sci.*, **31**, 1791-1806.

- Meneveau, C., 1991: Dual spectra and mixed energy cascade of turbulence in the wavelet representation. *Phys. Rev. Lett.*, **66**, 1450-1453.
- Meneveau, C. and K.R. Sreenivasan, 1987: Simple multifractal cascade model for fully-developed turbulence. *Phys. Rev. Lett.*, **59**, 1424-1427.
- Metais, O., J.P. Chollet, and M. Lesieur, 1984: Predictability of the large scales of freely evolving three and two-dimensional turbulence. *Predictability of Fluid Motions*, Holloway, G. and B.J. West, Ed., AIP Conference Proceedings No. 106, 303-319.
- Metais, O. and M. Lesieur, 1988: Statistical predictability of decaying turbulence. *J. Atmos. Sci.*, **43**, 857-869.
- Moeng, C.-H. and J.C. wyngaard, 1988: Spectral analysis of large-eddy simulation of the convective boundary layer. *J. Atmos. Sci.*, **45**, 3573-3587.
- Murphy, J.M., 1988: The impact of ensemble forecasts on predictability. *Q. J. R. Meteorol. Soc.*, **114**, 463-493.
- Nerenberg, M.A.H. and C. Essex, 1990: Correlation dimension and systematic geometric effects. *Phys. Rev.*, **42A**, 7065-7074.
- Neumann, J. and Y. Mahrer, 1974: A theoretical study of the sea and land breezes of circular island. *J. Atmos. Sci.*, **31**, 2027-2039.
- Neumann, J. and Y. Mahrer, 1975: A theoretical study of the lake and land breezes of circular lakes. *Mon. Wea. Rev.*, **103**, 474-485.
- Neuwstadt, F.T.M., P.J. Mason, C.-H. Moeng, and U. Schumann, 1991: Large-eddy simulation of the convective boundary layer: A comparison of four computer codes. Proc. 8th Turbulent Shear Flow Symp. Munich, 9-11 Sept. 1991. 6pp (in press).

- Newhouse, S., D. Ruelle, and F. Takens, 1978: Occurrence of strange axiom A attractors near quasi-periodic flows on  $T^m$  ( $m = 3$  or more). *Commun. Math. Phys.*, **64**, 35-
- Nicolis, C. and G. Nicolis, 1984: Is there a climatic attractor? *Nature*, **311**, 529-532.
- Nicolis, C. and G. Nicolis, 1991: Dynamics of error growth in unstable systems. *Phys. Rev.*, **A43**, 5720-5723.
- North, G.R., T.L. Bell, R.F. Calahan, and F.J. Moeng, 1982: Sampling errors in the estimation of empirical orthogonal functions. *Mon. Wea. Rev.*, **110**, 699-706.
- Osborne, A.R. and A. Provenzale, 1989: Finite correlation dimensions for stochastic systems with power-law spectra. *Physica*, **35D**, 357-381.
- Osborne, A.R. and R. Caponio, 1990: Fractal trajectories and anomalous diffusion for chaotic particle motions in 2-D turbulence. *Phy. Rev. Lett.*, **64**, 1733-1736.
- Oseledec, V.I., 1968: A multiplicative ergodic theorem: Lyapunov characteristic numbers for dynamical systems. *Trans. Moscow Math. Soc.*, **19**, 197.
- Owen, T., R.D. Cess, and V. Ramanathan, 1979: Enhanced CO<sub>2</sub> greenhouse to compensate for reduced solar luminosity on the early earth. *Nature*, **277**, 640-642.
- Packard, N.H., J.P. Crutchfield, J.D. Farmer, and R.S. Shaw, 1980: Geometry from a time series. *Phys. Rev. Lett.*, **45**, 712-716.
- Paegle, J. and T. Vukicevic, 1987: On the predictability of low-level flow during ALPEX. *Metror. Atmos. Phys.*, **36**, 45-60.
- Paegle, J., R.A. Pielke, G.A. Dalu, W. Miller, J.R. Garratt, T. Vukicevic, G. Berri, and M. Nicolini, 1990: Predictability of flows over complex terrain. *Current Directions in Atmospheric Processes Over Complex Terrain*. AMS Monograph. Blumen, W., Ed., **23**, 285-323.

- Palmer, T.N., 1988: Medium and extended range predictability and stability of the Pacific/North American mode. *Quart. J. Roy. Meteor. Soc.*, **114**, 691-713.
- Pielke, R.A., 1974a: A three-dimensional numerical model of the sea breeze over south Florida. *Mon. Wea. Rev.*, **102**, 115-134.
- Pielke, R.A., 1974b: A comparison of three-dimensional and two-dimensional numerical predictions of sea breeze. *J. Atmos. Sci.*, **31**, 1577-1585.
- Pielke, R.A., 1984: *Mesoscale Meteorological Modeling*. Academic Press, New York, 612pp.
- Pielke, R.A. and X. Zeng, 1989: Influence on severe storm development of irrigated land. *Natl. Wea. Dig.*, **14**, 16-17.
- Pielke, R.A., G. Kallos, and M. Segal, 1989: Horizontal resolution needs for adequate lower tropospheric profiling involved with atmospheric systems forced by horizontal gradients in surface heating. *J. Atmos. Oceanic Tech.*, **6**, 741-758.
- Pielke, R.A., G.A. Dalu, J.S. Snook, T.J. Lee, and T.G.E. Kittel, 1992a: Nonlinear influence of mesoscale landuse on weather and climate. *J. Climate*, **4**, 1053-1069.
- Pielke, R.A., W.R. Cotton, R.L. Walko, C.J. Tremback, W.A. Lyons, L.D. Grasso, M.E. Nicholls, M.D. Moran, D.A. Wesley, T.J. Lee, and J.H. Copeland, 1992b: A comprehensive meteorological modeling system - RAMS. *Meteor. Atmos. Phys.*, accepted.
- Pierrehumbert, R.T., 1990: Dimensions of atmospheric variability. *Beyond Belief: Randomness, Prediction and Explanation in Science*. Casti J.L. and A. Karlqvist, Ed., CRC Press, 110-142.
- Pomeau, Y. and P. Manneville, 1980: Intermittent transition to turbulence in dissipative dynamical systems. *Commun. Math. Phys.*, **74**, 189-197.
- Pool, R., 1989: Is something strange about the weather? *Science*, **243**, 1290-1293.

- Poincaré, H., 1908: *Science et méthode*. Ernest Flammarion, Paris.
- Roads, J.O., 1986: Forecasts of time averages with a numerical weather prediction model. *J. Atmos. Sci.*, **43**, 871-892.
- Rössler, O.E., 1976: An equation for continuous chaos. *Phys. Lett.*, **57A**, 397-398.
- Rotunno, R., 1983: On the linear theory of land and sea breeze. *J. Atmos. Sci.*, **40**, 1999-2009.
- Ruelle, R., 1990: Deterministic chaos: the science and the fiction. *Proc. R. Soc. Lond.*, **427A**, 241-248.
- Ruelle, D. and F. Takens, 1971: On the nature of turbulence. *Commun. Math. Phys.*, **20**, 167-192.
- Sano, M. and Y. Sawada, 1985: Measurement of the Lyapunov spectrum from a chaotic time series. *Phys. Rev. Lett.*, **53**, 1082-1085.
- Schadler, G., 1990: Triggering of atmospheric circulations by moisture inhomogeneities of the Earth's surface. *Bound.-Layer Meteor.*, **51**, 1-32.
- Schertzer, D. and S. Lovejoy, 1990: Nonlinear variability in Geophysics: Multifractal simulations and analysis. *Fractals: Their physical origin and properties*. Pietronero, L., Ed., Plenum Press, New York.
- Schertzer, D. and S. Lovejoy, 1991: *Scaling, Fractals and Nonlinear Variability in Geophysics*. Kluwer Academic Publishers, 318pp.
- Schubert, S.D. and M. Suarez, 1988: Dynamical predictability in a simple general circulation model: Averaged error growth. *J. Atmos. Sci.*, **46**, 353-370.
- Schumann, U., 1991: Subgrid length-scales for large-eddy simulation of stratified turbulence. *Theoret. Comput. Fluid Dynamics*, **2**, 279-290.

- Sharifi, M.B., K.P. Georgakakos, and I. Rodriguez-Iturbe, 1990: Evidence of deterministic chaos in the pulse of storm rainfall. *J. Atmos. Sci.*, **47**, 888-893.
- She, Zhen-Su and S.A. Orszag, 1991: Physical model of intermittency of turbulence: Initial-range non-Gaussian statistics. *Phys. Rev. Lett.*, **66**, 1707-1704.
- Shimada, I. and T. Nagashima, 1979: A numerical approach to ergodic problem of dissipative dynamical systems. *Prog. Theor. Phys.*, **61**, 1605-1615.
- Shukla, J., 1981: Dynamical predictability of monthly means. *J. Atmos. Sci.*, **38**, 2547-2572.
- Sinai, Y.G., 1959: On the concept of entropy of a dynamical system. *Dokl. Akad. Nauk. SSSR*, **124**, 768-771.
- Smagorinsky, J., 1963: General circulation experiments with the primitive equations. I. The basic experiment. *Mon. Wea. Rev.*, **91**, 99-164.
- Smagorinsky, J., 1969: Problems and promises of deterministic extended range forecasting. *Bull. Amer. Meteor. Soc.*, **50**, 286-311.
- Sreenivasan, K.R., 1991: Fractals and multifractals in fluid turbulence. *Annu. Rev. Fluid Mech.* **23**, 539-600.
- Stoop, R., and J. Parisi, 1991: Calculation of Lyapunov exponents avoiding spurious elements. *Physica*, **D50**, 89-94.
- Strange, G., 1989: Wavelets and dilation equations: A brief introduction. *SIAM Review*, **31**, 614-627.
- Takens, F., 1981: Detecting strange attractors in turbulence. *Dynamical Systems and Turbulence*, Springer-Verlag, 366-381.

- Thompson, P.D., 1957: Uncertainty of initial state as a factor in the predictability of large-scale atmospheric flow patterns. *Tellus*, **9**, 275-295.
- Thompson, P.D., 1988: Stochastic-dynamical prediction of three-dimensional quasi geostrophic flow. *J. Atmos. Sci.*, **45**, 2669-2679.
- Toth, Z., 1991a: Estimation of atmospheric predictability by circulation analogues. *Mon. Wea. Rev.*, **119**, 65-72.
- Toth, Z., 1991b: Intercomparison of circulation similarity measures. *Mon. Wea. Rev.*, **119**, 55-64.
- Tremback, C.J., 1991: Numerical Simulation of a mesoscale convective complex: model development and numerical results. Ph.D. dissertation. Department of Atmospheric Science paper No. 465, Colorado State University.
- Tremback, C.J. and R. Kessler, 1985: A surface temperature and moisture parameterization for use in mesoscale numerical models. *Proc. 7th AMS Conf. on Numerical Weather Prediction*, June 17-20, Montreal, Quebec, American Meteorological Society, Boston, 355-358.
- Tremback, C.J., G.J. Tripoli, R. Arritt, W.R. Cotton, and R.A. Pielke, 1986: The regional atmospheric modeling system. *Proc. Intel. Conf. on Development and Application of Computer Techniques to Environmental Studies*. November, 1986, Los Angeles, California, P. Zannetti, Ed., Computational Mechnica Publications, Boston, 601-607.
- Tripoli, G.J. and W.R. Cotton, 1982: The Colorado State University three-dimensional cloud/mesoscale model-1982. Part I: General theoretical framework and sensitivity experiments. *J. Rech. Atmos.*, **16**, 185-220.

- Tripoli, G.J. and W.R. Cotton, 1989a: Numerical study of an observed orogenic mesoscale convective system. Part I: Simulated genesis and comparison with observation. *Mon. Wea. Rev.*, **117**, 273-304.
- Tripoli, G.J. and W.R. Cotton, 1989b: Numerical study of an observed orogenic mesoscale convective system. Part II: Analysis of governing dynamics. *Mon. Wea. Rev.*, **117**, 305-328.
- Tsonis, A.A. and J.B. Elsner, 1988: The weather attractor over very short time scale. *Nature*, **333**, 545-547.
- Tsonis, A.A. and J.B. Elsner, 1990: Comments on "Dimension Analysis of Climatic Data". *J. Climate*, **3**, 1502-1505.
- Tsonis, A.A., J.B. Elsner, and K.P. Georgakakos, 1991: Evidence for low-dimensional attractors in weather and climate: How conclusive are they? *J. Atmos. Sci.*. Submitted.
- Van Tuyl, A.H. and R.M. Errico, 1989: Scale interaction and predictability in a mesoscale model. *Mon. Wea. Rev.*, **117**, 495-517.
- Vukicevic, T. and R.M. Errico, 1990: The influence of artificial and physical factors upon predictability estimates using a complex limited-area model. *Mon. Wea. Rev.*, **118**, 1460-1481.
- Vukicevic, T. and J. Paegle, 1989: The influence of one-way interacting lateral boundary conditions upon predictability of a flow in bounded numerical models. *Mon. Wea. Rev.*, **117**, 340-350.
- Walko, R.L. and C.J. Tremback, 1991: RAMS-The Regional Atmospheric Modeling System Version 2C: User's guide. Published by ASTeR, Inc., P.O.Box 466, Fort Collins Colorado, 86pp.

- Walko, R.L., W.R. Cotton, and R.A. Pielke, 1992: Large-eddy simulations of the effects of hilly terrain on the convective boundary layer. *Bound.-Layer Meteor.*, **58**, 133-150.
- WMO, 1990: Priprints of the *International Symposium on Assimilation of Observations in Meteorology and Oceanography*, Clermont-Ferrand, France, 9-13 July 1990. Sponsored by the World Meteorological Organization. 636pp.
- Warner, T.T., L.E. Key, and A.M. Lario, 1989: Sensitivity of mesoscale-model forecast skill to some initial-data characteristics, data density, data position, analysis procedure and measurement error. *Mon. Wea. Rev.*, **117**, 1281-1310.
- Warner, T.T., D. Keyser, and L.W. Uccellini, 1984: Some practical insights into the relationship between initial uncertainty and mesoscale predictability. *Predictability of Fluid Motions*, Holloway, G. and B.J. West, Ed., IAP Conference Proceedings No. 106, 271-286.
- Watson, A.J. and J.E. Lovelock, 1983: Biological homeostasis of the global environment: the parable of daisyworld. *Tellus*, **35B**, 284-289.
- Wetzel, P.J. and J.T. Chang, 1988: Evapotranspiration from non-uniform surfaces: A first approach for short-term numerical weather prediction. *Mon. Wea. Rev.*, **116**, 600-621.
- Wolf, A., J.B. Swift, H.L. Swinney, and J.A. Vastano, 1985: Determining Lyapunov exponents from a time series. *Physica*, **16D**, 285-317.
- Woodruff, S.D., R.J. Slutz, R.L. Jenne, and P.M. Steurer, 1987: A comprehensive ocean-atmosphere data set. *Bull. Amer. Meteor. Soc.*, **68**, 1239-1250.
- Xian, Z. and R.A. Pielke, 1992: The effects of width of land masses on the development of sea breeze. *J. Appl. Meteorol.*, **30**, 1280-1304.
- Zeng, X., R.A. Pielke, and R. Eykholt, 1990: Chaos in Daisyworld. *Tellus*, **42B**, 309-318.

- Zeng, X., R. Eykholt, and R.A. Pielke, 1991: Estimating the Lyapunov-exponent spectrum from short time series of low precision. *Phys. Rev. Lett.*, **66**, 3229-3232.
- Zeng, X., R.A. Pielke, and R. Eykholt, 1992a: Estimating the fractal dimension and the predictability of the atmosphere. *J. Atmos. Sci.*, **49**, 649-659.
- Zeng, X., R.A. Pielke, and R. Eykholt, 1992b: Extracting Lyapunov exponents from short time series of low precision. *Mod. Phys. Lett.* **6**, 55-75.
- Zeng, X., R.A. Pielke, and R. Eykholt, 1992c: Reply to Jascourt and Raymond. *Tellus E*  
In press.

## Appendix A

### EXPLANATION FOR SOME FEATURES IN FIGURES 4.3-4.4, AND 4.6-4.8

For one species with the parameters given in the paper, Eqs. (4.4) and (4.5) yield

$$(T_e + 273)^4 = \frac{SL}{\sigma} [0.5 + (0.5 - A_i) a_i], \quad (\text{A1})$$

and, since  $5 \leq T_e \leq 40$ , we have

$$(T_e + 273)^4 \cong (273)^4 + 4(273)^3 T_e \quad (\text{A2})$$

For black daisies with  $A_b = 0.25$ , Eq. (A1) becomes

$$(T_e + 273)^4 = \frac{SL}{4\sigma} (2 + a_b) , \quad (\text{A3})$$

so that  $T_e$  and  $a_w$  oscillate in phase (cf Figs. 4.3 and 4.4). On the other hand, for white daisies with  $A_w = 0.75$ , we have

$$(T_e + 273)^4 = \frac{SL}{4\sigma} (2 - a_w) , \quad (\text{A4})$$

and  $T_e$  and  $a_w$  have opposite phase (hence, in Fig. 4.6, the plots of  $T_e$  and  $a_w$  are inverted versions of each other).

For both black and white daisies with  $A_w = 0.75$  and  $A_b = 0.25$ , we can obtain from Eqs. (4.4) and (4.5) that

$$(T_e + 273)^4 = \frac{SL}{4\sigma} (2 + a_b - a_w). \quad (\text{A5})$$

Since the variation of  $a_b$  is larger than that of  $a_w$  in Figs. 4.7 and 4.8,  $T_e$  and  $a_b$  have the same phase, as can be seen from these figures. However, no such phase relationship exists between  $a_w$  and either  $T_e$  or  $a_b$ .